# Photocatalytic Seawater Splitting

**Yi Lu, Yi-Xuan Liu, Shang Cao, and Xiao-Yu Yang**

**Abstract** Low-carbon technologies have attracted wide interest for researchers. Among them, $H_2$ production from seawater splitting via photocatalysis is the most promising approach due to its abundant resources, low cost, and ease of construction on the large scale. However, there are many differences between water and seawater splitting in photocatalytic reactions. The ionic components in seawater and precipitate generation during the photocatalytic reaction have great impacts on seawater splitting. In this chapter, we have thoroughly introduced the principle, performance evaluation parameter, and features of photocatalytic seawater splitting, and we also summarized the recent development of the most fabricated photocatalysts including their structure, defects, and performances. At last, we discussed the economic cost and practical value of photocatalytic hydrogen industrialization, briefly summarized the design of large-scale synthesis and catalytic systems for photocatalysts, and explored their cost competitiveness.

**Keywords** Photocatalytic seawater splitting · Hydrogen production · Large-scale synthesis · System design · Industrial application

---

Y. Lu (✉)
Institut Für Anorganische Chemie Und Strukturchemie, Heinrich-Heine-Universität Düsseldorf, Universitätsstraße 1, 40225 Düsseldorf, Germany
e-mail: yi.lu@uni-duesseldorf.de

Y.-X. Liu · S. Cao
State Key Laboratory of Advanced Technology for Materials Synthesis and Processing, Wuhan University of Technology, Wuhan 430070, China

X.-Y. Yang
State Key Laboratory of Advanced Technology for Materials Synthesis and Processing (Wuhan), Foshan Xianhu Laboratory of the Advanced Energy Science and Technology Guangdong Laboratory (Xianhu Hydrogen Valley, Foshan), Laoshan Laboratory (168 Wenhai Middle Rd, Jimo District, Qingdao), Wuhan University of Technology, Wuhan, Hubei, China

X.-Y. Yang (ed.), *Photo-Driven Seawater Splitting for Hydrogen Production*,
https://doi.org/10.1007/978-981-99-0510-2_2

# 1 Preface

Photocatalytic seawater splitting (PCSS) is an eco-friendly method to produce clean burning and storable $H_2$ from two renewable sources including solar irradiation and seawater. The simplicity and low operational costs give PCSS systems a high potential for producing this gas at industrial levels.

The PCSS reaction taking place in a reactor begins with light absorption by a photocatalyst (such as semiconductor materials), which causes a transition of an electron from the valence band to the conduction band while leaving a hole in the valence band. Semiconductors that have an energy difference between their valence and conduction bands (called the band gap) greater than 1.23 eV are capable of promoting the redox events that lead to water splitting $H_2O$. Many semiconductor materials developed thus far for photocatalytic water splitting (PCWS) such as $TiO_2$, g-$C_3N_4$, CdS, and $WO_3$ have remarkable performances.

Several options exist for using semiconductor technologies in devices that utilize sunlight for water splitting, including the photovoltaic (PV)-assisted electrochemical (PV-E), photoelectrochemical (PEC), and PCSS methods. Compared to the process in PCSS systems, in PV-E as well as PEC cells, hydrogen and oxygen are evolved at macroscopically distant locations. Therefore, the basic design of PCSS systems is not identical to those of the PEC and PV-E counterparts. While it is believed that PCSS systems are less expensive than others, to date, only laboratory-scale devices have been extensively explored. However, the approaches devised thus far are nor amenable to scale up to the kilogram level. Moreover, large numbers and types of dissolved salts are present in seawater, and these salts participate in a variety of photocatalyzed chemical reactions that result in the reduction of the activity and durability of the photocatalyst.

In this chapter, we discuss the basic operational principles of PCSS and review the state-of-the-art materials that have been developed as photocatalysts for these systems. We also analyze past studies that have revealed key principles for the design of photocatalysis and guidelines that can be used to fabricate more efficient materials. In the final section, we review the different types of devices that have been designed thus far for large-scale PCSS.

# 2 Principles

## 2.1 Mechanism for $H_2$ Production in PCSW Systems

The basic process involved in sunlight-promoted photocatalyzed water splitting to generate $H_2$ is depicted in Fig. 1. In the process, the energy of a photon is converted into chemical energy for water splitting that requires a large positive Gibbs free energy change (Fig. 2). The overall process is similar to the one occurring in photosynthesis by green plants and, therefore, PCWS is regarded as artificial photosynthesis. From the viewpoint of the Gibbs free energy change, PCWS is distinguished from photocatalytic degradation reactions such as $TiO_2$ photocatalyzed oxidation of organic compounds using oxygen, which are generally thermodynamically downhill processes.

The stepwise sequence involved in the PCWS reaction begins with the absorption of a photon of light by the photocatalyst, which promotes the transition of an electron in the valence band to the higher energy conduction band. The light promoting this transition must have an energy equal to that of the band gap. This event forms an electron–hole pair in the form of a negative-electron ($e^-$) and positive-hole ($h^+$), which then migrate to the surface of the photocatalyst where they induce water splitting to produce $H_2$ and $O_2$ by serving as respective reducing and oxidizing agents. The mechanism followed in a PCWS reaction is depicted in Fig. 3.

Splitting water to form $H_2$ and $O_2$ (Eq. 1) is an energetically uphill process that has a standard Gibbs free energy change ($\Delta G_0$) of 237 kJ/mol or 1.23 eV. To enable

**Fig. 1** Hydrogen production from water using photocatalyst under solar irradiation

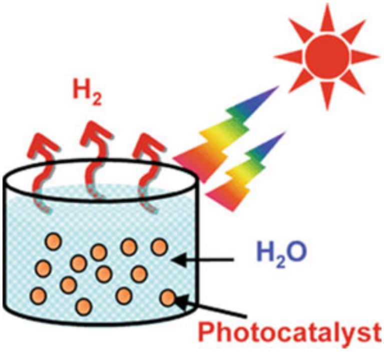

**Fig. 2** Energetic changes in photosynthesis by green plants and PCWS

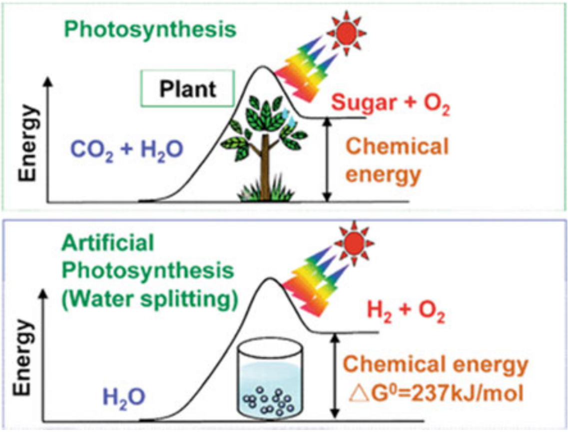

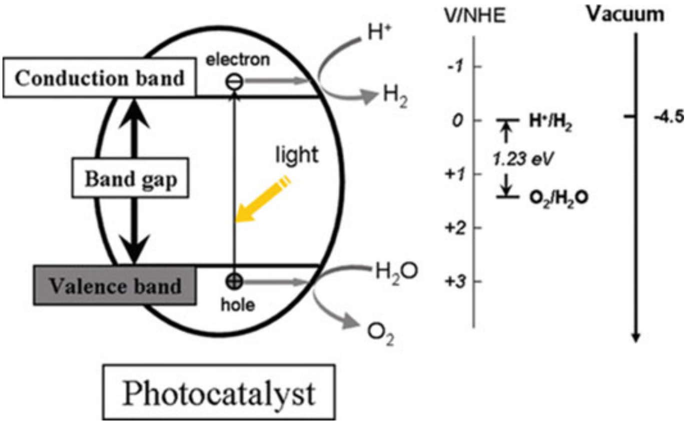

**Fig. 3** Schematic diagram of the mechanism of PCWS for hydrogen and oxygen generation

both reduction and oxidation of $H_2O$ by the photoexcited electron and hole (exciton), the reduction and oxidation potentials of water should lie within the band gap energy of the photocatalyst, with the energy of the conduction band being more negative than the reduction potential of $H+/H_2$ (0 V vs. normal hydrogen electrode (NHE)), and that of the valence band being more positive than the oxidation potential of $O_2/H_2O$ (1.23 V). The electronic structures of semiconductor systems match well with the redox potential associated with transforming water into $H_2$ and $O_2$. Other factors, such as overpotentials, charge separation and mobility, and lifetime of the photogenerated electron and hole, affect the efficiency of photocatalytic generation of hydrogen from water splitting.

$$H_2O \rightarrow \frac{1}{2}O_2 + H_2;\ \Delta G = +237\,\mathrm{KJ/mol} \tag{1}$$

The second step in the mechanism for PCWS is charge separation and migration of the photogenerated electron and hole. Competing with these events is energy wasting charge recombination (both surface and bulk) that leads to deactivation by emitting light or generating phonons [1]. Moreover, the separation of an excited electron and hole sometimes has an energy barrier associated with the binding energies of these oppositely charged species. Efficient charge separation and transport is enhanced by avoiding bulk/surface charge recombination. Examples of the approaches that have been employed to facilitate charge separation and transport include incorporating an internal electric field and using high photoconductive semiconductor materials.

The final step in the PCWS process involves surface chemical reactions that lead to $H_2$ and $O_2$ formation. Importantly, for these reactions to take place efficiently it is necessary to have a large number of active sites on the semiconductor surface carrying the photoexcited electrons and holes. Cocatalysts such as Pt, NiO, and $RuO_2$ are typically utilized to introduce active sites for the reduction of water to evolve $H_2$. Active sites for holes are needed to promote 4-electron oxidation of water for $O_2$

evolution. It is necessary to use cocatalysts and photocatalysts that have unfavorable properties for this process.

## *2.2 Measurement of the Performance of PCWS Systems*

Three metrics have been typically used to quantify the performance of PCWS systems including $H_2$ production rate, internal quantum yield (IQY) or apparent quantum yield (AQY), and solar-to-hydrogen (STH) conversion efficiency, which reflect three different aspects of the process (Scheme 1).

### 2.2.1 $H_2$ Production Rate

The activity of a PCWS system can be represented by the $H_2$ production rate (*r*, the amount of $H_2$ produced vs. reaction time and photocatalyst mass). The time and mass are the two factors determining the $H_2$ production rate, which is expressed by the amount of evolved $H_2$ or $O_2$ per unit irradiation time and the amount of photocatalysts ($\mu$mol $h^{-1}$ $g^{-1}$ or $\mu$mol $h^{-1}$ $mg^{-1}$) [2, 3]. However, many other factors influence the production rate including properties [4]. The use of different sets of parameters in studies in this area has led to confusion in comparing *r* directly, indicating that reporting protocols need to be standardized. Normalizing the *r* by using the mass of the photocatalyst is erroneous because *r* does not linearly increase with m owing to light-shielding effects (see Fig. 4) [5]. The light-shielding effects of photocatalysts occurring with increased photocatalyst mass is illustrated in Fig. 4. When the use of photocatalysts increases from $m_1$ in the graph, the shielding effect becomes more significant, and the gas evolution rate plateaus at high mass. Specifically, when a high mass of photocatalyst is present, numerous particles cannot participate in light absorption due to limited light penetration depth. Therefore, it is recommended that an *r*–*m* curve (Fig. 4) be provided when the efficiency of PCWS systems is given in terms of the $H_2$ evolution rate.

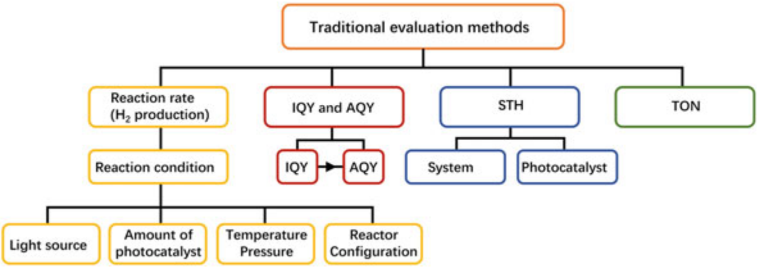

**Scheme 1** Traditional methods to evaluate PCWS performance

**Fig. 4** The relationship between gas production rate and mass of photocatalyst

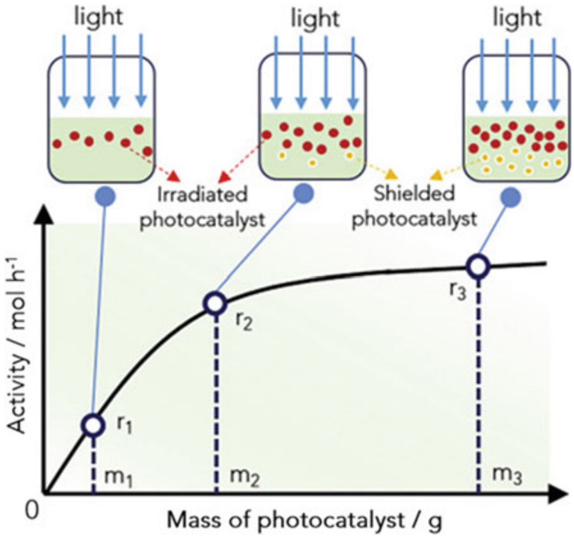

The $H_2$ production rate is governed by many factors, such as the temperature, pressure, and type of reaction system. To establish standard conditions for evaluating lab-based systems, we suggest using a temperature in the range of 10–25 °C that can be easily maintained through the use of a closed-water circulation system. An on-line gas chromatograph is normally used to measure gas evolution. However, the accumulation of $H_2$ and $O_2$ in the system will change the atmosphere and pressure, which leads to changes in gas evolution rates as the reaction progresses except when the rate is low. To minimize potential measurement errors, it is suggested that the system be calibrated under the same condition as those used in the overall water splitting reaction.

Under practical operating conditions, it is difficult to maintain a photocatalytic water splitting reactor at reduced pressures and temperatures. Therefore, determining the STH efficiency under ambient pressure and product gas analysis using a gas chromatograph are more acceptable. Also, it is best to utilize a flow reaction system that enables maintenance of the same atmosphere and pressure throughout the course of the process.

When photocatalysts have sufficiently high overall water splitting efficiencies, it is best to use the upward water displacement to quantify the amount of produced gas because this method does not rely on expensive equipment.

### 2.2.2 Internal Quantum Yield (IQY)

IQY has been defined by IUPAC as the number of electrons utilized for the reaction per number of absorbed photons in a given period time [6]. The electrons utilized for productive reactions are the number of molecules of reactant consumed or product formed. Thus, IQY describes the efficiency of a photocatalyst that transforms light into active charges, which is independent of the photocatalyst's mass. At the early stage, the IQY was not widely used because of the great challenge associated with accurately measuring the absorption of photons [7, 8].

### 2.2.3 Apparent Quantum Yield (AQY)

Due to differences in conditions employed for photocatalytic reactions (especially irradiation conditions), direct comparisons of the activities of catalysts based on the amounts or rates of gases produced are not possible. Thus, at the current time, assessing the photocatalyst performance of PCWS systems requires the determination of both quantum yields and STH energy conversion efficiencies. Owing to light transmission and scattering, determining the actual number of photons absorbed by the photocatalyst is not possible. Hence, apparent quantum yield (AQY), or sometimes called the external quantum efficiency (EQE), calculated using Eq. (2), is used

$$\mathrm{AQY} = \frac{nR}{I} \tag{2}$$

in which $n$, $R$, and $I$ represent the number of electrons or holes consumed, the quantity of gas molecules evolved in a specific time interval, and the number of incident photons reaching the photocatalytic system during the same time interval, respectively. It is important to determine the AQY as a function of irradiation wavelength.

The AQY provides insights into the intrinsic properties of a photocatalyst without knowing the mechanism of the overall water splitting or half-reaction. The AQY of a system can be diminished by energy wasting, such as charge recombination and back reactions, and is reflective of the quality of the semiconductor as well as those of the cocatalyst. Using the photocatalytic $H_2$ production reaction as an example, holes generated simultaneously with photoexcited electrons induce the formation of radicals, which can transfer electrons to the conduction band. In this case, one photon causes the production of two electrons for the HER, which can potentially lead to an AQY for HER over 100%. Therefore, it is important to understand the intrinsic nature of a photocatalyst in terms of light harvesting, separation efficiency, transfer kinetics, and utilization of carriers via surface catalytic reactions.

For the overall water splitting process, within experimental error the AQY calculated based on $H_2$ generation should be the same as that of $O_2$ generation. For photocatalytic half-reaction, AQY is the most significant parameter for evaluating the efficiency of a photocatalyst.

AQY is strongly dependent on the wavelengths of the incident photons due to varied absorption coefficients of a semiconductor at different irradiation wavelengths ($\lambda$) [9]. The setup for AQY measurements is similar to that used for a normal photocatalytic activity determination. Two critical criteria need to be met in making this measurement. First, the AQY is normally evaluated at the maximum photocatalytic rate which is attained by using light corresponding to the absorption wavelength maximum of the photocatalyst. Second, monochromatic light should be employed by using combined band-pass and cut-off filters.

The standard actinometer method for the conversion of ferrioxalate ions into $Fe^{2+}$ ions also provides an optional technology to determine the incident photon flux [10, 11]. Although the actinometer method also has some uncertainties, including the quantum yield of the reaction not actually being 100%, it can be used as a verification for the reliability measurements using photodetectors.

### 2.2.4 Solar-To-Hydrogen (STH) Efficiency

In 1985, Bolton et al. suggested that evaluations of PCWS systems should be based on the solar-to-hydrogen (STH) conversion efficiency. This is the most important parameter used to evaluate the water splitting device exposed to broadband solar Air Mass 1.5 Global (AM1.5 G) illumination under zero bias conditions [10]. During the past decades, this approach has gradually become accepted for evaluating the photocatalytic activity of PCWS [12, 13]. STH refers to the ratio of solar energy stored in formed $H_2$ to the incident solar energy as described in Eq. (3) [14].

$$\mathrm{STH} = \frac{\text{Output energy as } \mathrm{H_2}}{\text{Energy of incident solar light}} = \frac{r_{H_2} \times \Delta G_r}{P_{\mathrm{sun}} \times S} \tag{3}$$

where $P_{\mathrm{sun}}$ is the energy flux of the sunlight, $S$ is the irradiated area, $r_{H_2}$ is the rate of $H_2$ production, and $\Delta G_r$ is the reaction Gibbs energy. Solar irradiation has an energy flux of 100 mW $cm^{-2}$. It should be noted that solar energy and $H_2$ are the only energy inputs and outputs, respectively, and that $H_2$ and $O_2$ evolved in a stoichiometric ratio [15]. Furthermore, it should be adjusted taking into account the experimental conditions when used in the calculation of STH efficiency, such as temperature and pressure.

The STH efficiency is considered to be the standard for the evaluation of photocatalyst performance. The intensity for STH measurement should be set as one sun, which is typically obtained via a solar simulator (AM 1.5G, 100 mW/$cm^2$). Calculating STH energy conversion efficiency using concentrated sunlight is not comparable arising by using a solar simulator because $H_2$ evolution rates on various photocatalysts are not proportional to the incident light intensity.

Due to the fluctuation of sunlight caused by weather and altitude, simulated light sources like a Xenon lamp, high-pressure mercury lamp, and solar simulators are used in laboratory research (Fig. 5A). The power spectra of Xenon and mercury lamps include a strong UV light region. However, mercury lamps emit this light as individual lines rather than a continuum, thus the spectral mismatch with sunlight is large. Therefore, solar simulators which simulate the standard sunlight (AM1.5G) with appropriate spectrum distribution and stable light intensity are highly recommended for the laboratory level comparisons.

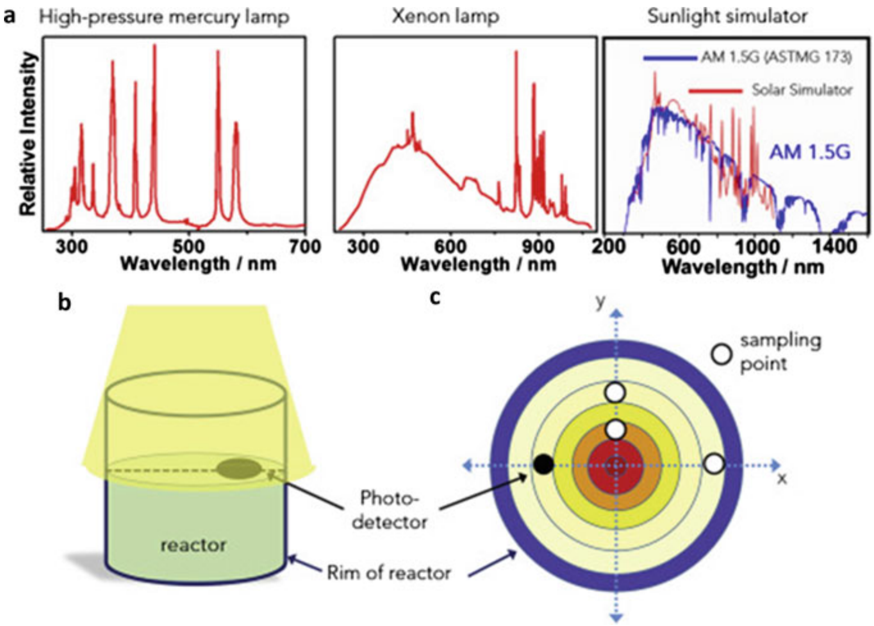

**Fig. 5** **a** Typical power spectra of different light sources, **b** schematic diagram of light spot size and reactor, and **c** the Photon flux is calculated by measuring the light intensity in different areas via a light detector

In the case of uniformly distributed light intensity (Fig. 5B), the incident light intensity is relevant to the irradiation area and the distance of the reaction mixture from the light source. But the light intensity is distributed non-uniform within the irradiation area in practice (Fig. 5C), in which case a numerical integration needs to be performed to estimate the total intensity of input light. In this case, it is assumed that the light intensity is constant at the same distances from the center of the reactor (Fig. 5C) [9]. The first step in determining the STH energy conversion efficiency is the identification of the location of the highest light intensity region within the irradiation area. Starting at the maximum point, the intensity along the radial direction is then measured by changing the location of the photodetector along the *x*- and *y*-axis at the same intervals (Fig. 5C). After measuring the light intensity distribution within the irradiation area, the total incident photons can be measured with reasonable accuracy [4].

What is the difference between AQY and STH? Typically, AQY is measured at a specific wavelength or over a narrow range of wavelengths. Thus, there is no correlation between AQY and STH, because the effect of wavelength-dependent light absorption is fully considered in determining STH but not in AQY. Only in the case when STH is determined using a monochromatic light source can the two indicators be interconverted by using Eq. 4,

$$\mathrm{STH}_\lambda = \mathrm{AQE} \cdot \frac{\lambda \Delta G^0}{hcnN_A} \tag{4}$$

where $\mathrm{STH}_\lambda$ is the STH measured at wavelength $\lambda$, $h$ is Planck's constant, c is the speed of light, and NA is Avogadro's number. Nevertheless, a high AQY at any wavelength is sufficient to indicate that efficient charge carrier separation, transport, and surface reactions have occurred which are also parameters for high STH over the entire solar spectrum. These physical processes are relatively independent of irradiation wavelength and can be described mathematically, which enables STH to be correlated to AQY to some extent. A detailed review on this aspect is found elsewhere [16, 17].

The theoretical limit for the STH efficiency is 31% in overall water splitting [18], which is the percentage of solar energy stored as chemical energy for hydrogen production. Considering inevitable losses, it has a practical limit of 11% [19]. But in practice, the STH efficiency of photocatalytic overall water splitting rarely exceeds 1%. One important reason for this is that only semiconductors that have $E_g$ that is significantly larger than 1.23 eV have overall water splitting activity, such as some well-known examples like $TiO_2$, $SrTiO_3$, $NaTaO_3$, $Ga_{1-x}Zn_xN_{1-x}O_x$, and g-$C_3N_4$ [20–24]. The large $E_g$ of these semiconductors prevents the utilization of most visible and infrared light, which accounts for over 95% of solar light received at sea level. Hence, enhancing the response of photocatalysts to visible light is an important goal for improving STH efficiency.

Another major factor leading to low STH efficiencies is energy (photon) wasting radiative or non-radiative recombination of photogenerated electrons and holes occurring in competition with promoting water splitting. Carrier diffusion length, which is the average distance a charge carrier travels in a semiconductor before recombination takes place, offers a way to intuitively compare the extent of recombination. This length typically ranges from over one millimeter for lightly doped silicon wafers to a few nanometers for the common photocatalyst $TiO_2$ [25, 26]. Short carrier diffusion lengths significantly impact photocatalytic efficiencies, which means that electrons/holes separation that happened deeper inside the bulk photocatalysts does not contribute to promoting surface redox reactions [16].

### 2.2.5 Ton

Turnover number (TON), defined as the number of reacted molecules to those of active sites (Eq. (5)), is usually used to assess the efficiencies of photocatalyst.

$$\mathrm{TON} = \frac{\text{Number of reacted molecules}}{\text{Number of active sites}} \tag{5}$$

In fact, the numbers of active sites present in photocatalysts is difficult to determine. Thus, Eq. (6)) or Eq. (7) is employed in determining TON.

$$\text{TON} = \frac{\text{Number of reacted electrons}}{\text{Number of atoms in a photocatalyst}} \tag{6}$$

$$\text{TON} = \frac{\text{Number of reacted electrons}}{\text{Number of atoms at the surface of a photocatalyst}} \tag{7}$$

However, these values cannot be applied to particulate photocatalysis systems due to the great challenge of identifying the number of active sites. However, most of the reported studies do not provide sufficient and exact experimental details, which leads to great difficulties in accurately evaluating and comparing photocatalytic performances. In addition, each of these evaluation parameters has its own insufficiencies or need for use of specific conditions. Only through a comprehensive and rational evaluation can the photocatalytic performance of a system be reasonably assessed and compared.

## *2.3 Features and Effects on the Performance*

### 2.3.1 Salt Components

A large content of various salts is a characteristic feature of seawater. The main ionic components of >90% of these salts are $Na^+$, $Mg^{2+}$, $Ca^{2+}$, $K^+$, $Cl^-$, and $SO_4^{2-}$ [27]. Unfortunately, these salts have a great impact on PCSS, because the efficiencies of most photocatalysts are lower in natural or simulated seawater than in pure water [28–31], while only a few show the opposite behavior [32]. The mechanism by which ions in seawater control the water splitting process is still at an exploratory stage and, to date, no universal effects seem to apply to different systems. The main component of seawater is NaCl and most reports on splitting of seawater discuss the effects of $Na^+$ and $Cl^-$ on the photocatalytic performance. For example, Li et al. found that $Na^+$ abundantly adsorbs on the surface of $TiO_2$ leading to enhance adsorption of sacrificial agents under alkaline or neutral conditions [28]. These agents readily combine with the photogenerated holes, facilitate charge separation, and reduce electron–hole recombination. It should be noted that at high NaCl concentrations (>1.0 mol $L^{-1}$), sacrificial agents undergo indirect $Na^+$-induced adsorption on the photocatalyst surface where they reduce the charge transfer efficiency of the photocatalyst [33].

Two different perspectives can be used to consider the effects of $Cl^-$ on photocatalytic seawater splitting. Li et al. suggested earlier that although $Cl^-$ reacts with holes, it also participates in reduction reaction with electrons in the conduction band (Eqs. (8) and (9)), thus decreasing the photocatalytic activity [28]. Ho et al. also speculated on the reason why the $H_2$ evolution rate was lower in seawater than in pure water [34]. The rate reduction can also be the reaction of the $Cl^-$ in seawater with holes to generate $Cl\cdot$, which competes with the $H^+$ reduction reaction (Eqs. (9) and (10)). No other chlorine-containing compounds are produced in the reaction, and the $Cl^-$ concentration remains unchanged, which is consistent with the speculation.

$$Cl^- + h^+ \rightarrow \cdot Cl \tag{8}$$

$$\cdot Cl + e^- \rightarrow Cl^- \tag{9}$$

$$Cl\cdot + Cl^- \rightarrow Cl\cdot_2^- \tag{10}$$

$$Cl\cdot_2^- + e^- \rightarrow 2Cl^- \tag{11}$$

Simamora et al. [35] suggested that many hydroxyl groups, such as in the form of $TiOH_2$ and Ti–OH, react with $Cl^-$ on the surface of $TiO_2$ to form TiCl and reduce the photocatalytic activity. But in general, all the reasons presented above are speculative at this stage, and no additional experimental data has been provided to confirm the conclusion.

However, the results of some studies indicate that $Cl^-$ has a positive effect on the efficiency of PCSS. For example, Ji et al. [36] proved that no decrease in $Cl^-$ concentration occurs during a 6 h of photocatalytic reaction. Guan et al. found that although oxidation of $Cl^-$ takes place to form $Cl_2$ ($Cl_2/Cl^-$, 1.36 V vs. NHE, pH = 0), the process is thermodynamically more difficult than oxidation of $H_2O$ to form $O_2$ ($O_2/H_2O$, 1.23 V vs. NHE, pH = 0), since it is a two-electron redox process and kinetically more favorable [37]. Therefore, after the oxidation of $Cl^-$ takes place, oxidation of water occurs (Eqs. (12) and (13)). Yang et al. postulated that holes are consumed by participation in the $Cl^-$ oxidation reaction and, thereby, the rate of electron–hole recombination is lowered [38].

$$Cl_2 + H_2O \rightarrow H^+ + Cl^- + HClO \tag{12}$$

$$2HClO \rightarrow 2H^+ + 2Cl^- + O_2 \tag{13}$$

Lee et al. [36] tested the effects of NaCl, $MgCl_2$, $MgSO_4$, $CaSO_4$, $K_2SO_4$, $K_2CO_3$, and $MgBr_2$ on simulated seawater splitting. The results reveal that all these dissolved electrolytes except $K_2SO_4$ decrease the $H_2$ formation rate, and $MgCl_2$ is the most detrimental. A solution of natural seawater containing ca. 74% and 15% of $Mg^{2+}$ and $Cl^-$, respectively, has the lowest activity with a twofold decreased hydrogen formation rate compared to that of pure water. Note that without $MgCl_2$, photocatalyst in simulated seawater has better performance than in seawater containing all seven salts, indicating that $Mg^{2+}$ is the main deactivating species.

### 2.3.2 Sacrificial Agents

Sacrificial reagents are often introduced to enhance the separation of carriers in water splitting (Fig. 6). When the PCWS reaction is carried out in an aqueous solution containing a reducing reagent such as alcohols and sulfide ion, which serve as respective electron donors or hole scavengers, photogenerated holes are irreversibly reduced through oxidation of the reducing reagent instead of water. This process enriches the number of electrons in the photocatalyst which enhances the HER (Fig. 6a). When reducing reagents are present in biomass and compounds naturally occurring and industrial wastes, this reaction should be advantageous for hydrogen production [39]. On the other hand, photoexcited electrons are consumed by oxidizing agents (electron acceptors) such as $Ag^+$ and $Fe^{3+}$ and thus resulted in an enhancement of the OER (Fig. 6b). Reactions using sacrificial reagents which affect the half-reactions involved in water splitting are often used to determine if a photocatalyst has the required thermodynamics and kinetics for $H_2$ and $O_2$ evolution. Even when a photocatalyst is capable of promoting these half-reactions, no guarantee exists that it will be able to induce the HER and OER in the absence of sacrificial reagents.

In spite of the fact that photocatalytic splitting using pure water can be achieved without employing sacrificial agents, most of those in which $TiO_2$ is the photocatalyst still utilize sacrificial agents. Notably, some work reported that inorganic and organic substances indigenously present in seawater can play roles of sacrificial agents to improve performance [40].

#### $S^{2-}/SO_3^{2-}$ System

The $S^{2-}$ and $SO_3^{2-}$ ions can react with photogenerated holes to form $S_n^{2-}$ and $SO_4^{2-}$, respectively; therefore, they could be used as sacrificial reagents in photocatalytic reactions [41–46]. However, oxidation of $S^{2-}$ to form yellow polysulfides

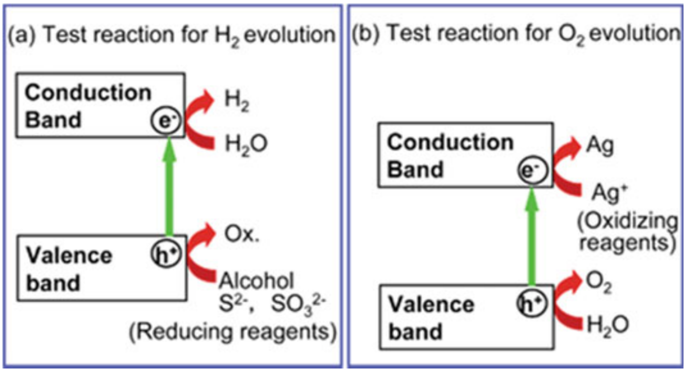

**Fig. 6** Description of half-reactions of water splitting in the presence of sacrificial reagents

$S_n{}^{2-}$ leads to a decrease in the rate of $H_2$ formation over time owing to competitive light absorption by $S_n{}^{2-}$ in the visible region and reduction of $S_n{}^{2-}$ is competitive with $H_2O$ [43, 47]. Fortunately, $SO_3{}^{2-}$ can act as an agent for regenerating $S^{2-}$ from $S_n{}^{2-}$ thus keeping the solution colorless [48]. Thus, the $S^{2-}/SO_3{}^{2-}$ mixture has been widely used as an electron donor to improve photoactivity and photostability for $H_2$ production from water splitting [49–54]. The mechanism for the reaction occurring in the presence of $S^{2-}/SO_3{}^{2-}$ as a sacrificial reagent is depicted in Eqs. (14)–(19).

$$\text{photocatalyst} + hv \rightarrow h^+ + e^- \tag{14}$$

$$2e^- + 2H_2O \rightarrow H_2 + 2OH^- \tag{15}$$

$$SO_3^{2-} + 2OH^- + 2h^+ \rightarrow SO_4^{2-} + 2H^+ \tag{16}$$

$$2S^{2-} + 2h^+ \rightarrow S_2^{2-} \tag{17}$$

$$S_2^{2-} + SO_3^{2-} \rightarrow S_2O_3^{2-} + S^{2-} \tag{18}$$

$$SO_3^{2-} + S^{2-} + 2h^+ \rightarrow S_2O_3^{2-} \tag{19}$$

Since $S_2O_3{}^{2-}$ can be oxidized by photogenerated holes to form $SO_3{}^{2-}$ and subsequently to $SO_4{}^{2-}$, it also can be used as a sacrificial reagent during the photocatalytic reaction.

### $H_2S$-Splitting System

Photocatalytic $H_2$ production from $H_2S$ dissolved in water is particularly interesting [55–62]. This process, in which sulfide ions generated by the reaction of $H_2S$ with hydroxide serve as sacrificial agents, could have practical applications to remove $H_2S$ from natural gas and to desulfurize petrochemicals. As shown in (14) and (20)–(22), the overall process corresponds to $H_2S$ splitting using two photons of visible light, which requires 39.3 kJ/mol.

$$H_2S + OH^- \rightarrow HS^- \tag{20}$$

$$2HS^- + 2h^+ \rightarrow S_2^{2-} + 2H^+ \tag{21}$$

$$2H^+ + 2e^- \rightarrow H_2 \tag{22}$$

### Other Inorganic Sacrificial Reagents

Other inorganic compounds containing ions, such as $Fe^{2+}$ [63], $Ce^{3+}$, [64] $I^-$, $Br^-$, and $CN^-$, [65] have been used as sacrificial reagents for hydrogen generation. These inorganic ions are easily oxidized by the photogenerated holes to form the corresponding $Fe^{3+}$, $Ce^{4+}$, $I^{3-}$ (or $IO^{3-}$), $Br_2$, and $OCN^-$ ions. Using $I^-$ as an example, the mechanism for photocatalytic $H_2$ production is described in Eqs. (23)–(25).

$$2H^+ + 2e^- \rightarrow H_2 \tag{23}$$

$$3I^- + 2h^+ \rightarrow I_3^- (\text{in acidic solution}) \tag{24}$$

$$I^- + 6OH^- + 6h^+ \rightarrow IO_3^- + 3H_2O(\text{in basic solution}) \tag{25}$$

Some of the species, such as $Fe^{3+}$, $Ce^{4+}$, and $IO^{3-}$, can be easily reduced by photogenerated electrons and, thus, act as electron acceptors for photocatalytic $O_2$ production from aqueous solution [66, 67].

### Organic Sacrificial Reagents

Organic compounds, for example, alcohols (methanol, ethanol, isopropanol, etc.) [68], carboxylic acids (formic acid, acetic acid, etc.), and aldehydes (formaldehyde, acetaldehyde, etc.) [69] could also be used as electron donors for photocatalysis. Among these, methanol has been most widely used, and the reaction is described in Eqs. (26)–(30) [70].

$$h^+ + H_2O \rightarrow \cdot OH + H^+ \tag{26}$$

$$CH_3OH + \cdot OH \rightarrow \cdot CH_2OH + H_2O \tag{27}$$

$$\cdot CH_2OH \rightarrow HCHO + H^+ + e^- \tag{28}$$

$$2H_2O + 2e^- \rightarrow H_2 + 2OH^- \tag{29}$$

$$\text{overall reaction}: CH_3OH \overset{hv,\text{catalyst}}{\rightarrow} HCHO + H_2 \tag{30}$$

Formaldehyde (HCHO) as the product can be further oxidized to form formic acid (HCOOH) and subsequently convert to $CO_2$ together with $H_2$ via Eqs. (31) and (32) [71]:

$$\mathrm{HCHO + H_2O \overset{hv,\text{catalyst}}{\rightarrow} HCOOH + H_2} \tag{31}$$

$$\mathrm{HCOOH \overset{hv,\text{catalyst}}{\rightarrow} CO_2 + H_2} \tag{32}$$

In these photocatalytic processes, organic compounds are oxidized by the photogenerated holes and the residual photogenerated electrons reduce water to form hydrogen. Thus, it is possible to design a bifunctional photocatalytic system in which organic pollutants in water act as electron donors to achieve photocatalytic production of hydrogen and simultaneous degradation of the pollutants [72]. Hashimoto et al. performed pioneering studies on photocatalytic $H_2$ production from fossil fuels and hydrocarbons in water where powdered Pt/$TiO_2$ is used as a suspended [73]. The mechanism in these reactions could be explained by Eqs. (14) and (33)–(39).

$$\mathrm{h^+ + H_2O \rightarrow \cdot OH + H^+} \tag{33}$$

$$\mathrm{H^+ + e^- \rightarrow 1/2H_2} \tag{34}$$

$$\mathrm{RCH_2CH_3 + 2 \cdot OH \rightarrow RCH_2CH_2OH + H_2O} \tag{35}$$

$$\mathrm{RCH_2CH_2OH \rightarrow RCH_2CHO + H_2} \tag{36}$$

$$\mathrm{RCH_2CHO + H_2O \rightarrow RCH_2COOH + H_2} \tag{37}$$

$$\mathrm{Photo - Kolbe\,reaction : RCH_2COOH \rightarrow RCH_3 + CO_2} \tag{38}$$

$$\mathrm{Overall\,reaction : RCH_2CH_3 + 2H_2O \overset{hv,\text{catalyst}}{\rightarrow} RCH_3 + 3H_2 + CO_2} \tag{39}$$

### 2.3.3 Cocatalysts

Electrocatalysts that specifically catalyze desired redox reactions when used in conjunction with a light-absorbing material are termed cocatalysts [4]. Cocatalysts continue to be materials of interest in the field of artificial photosynthesis. A cocatalyst can be vital for promoting the efficiency of charge separation and suppressing charge recombination of electrons and holes for photocatalytic water splitting. Specifically, the work functions or band levels of the cocatalysts need to be compatible with the Fermi-levels or electronic structures of the photocatalysts. When this occurs, desirable junctions (an Ohmic-type or Schottky-type contact) are generated that allow charges to flow in the correct direction at the interface.

**Fig. 7** Schematic diagram of charge transfer from inside to the surface

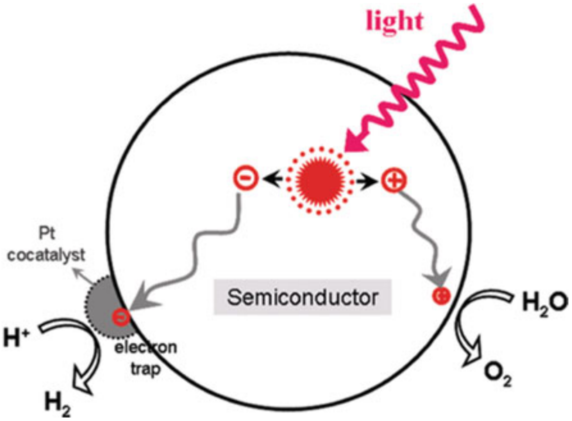

Generally speaking, cocatalysts are chosen from metals such as Pt, Rh, Ru, Ir, and Ni nanoparticles to accelerate $H_2$ evolution, and oxides of Co, Fe, Ni, Mn, Ru, and Ir function to accelerate $O_2$ evolution [74]. For a majority of the water splitting photocatalysts, a $H_2$ evolution cocatalyst is obligatory because of the existence of an insufficient overpotential for $H^+$ reduction compared to that for $H_2O$ oxidation.

Transition metals, especially noble metals, are commonly used as cocatalysts in PCWS. For example, charge transfer between Pt and host photocatalyst is displayed in Fig. 7. In this system, photogenerated electrons transfer to the surface and are entrapped by the noble metal due to its lower Fermi energy level than the photocatalyst. Meanwhile, the photogenerated holes migrate to the surface of the host photocatalyst, resulting in the efficient separation of electrons and holes.

### Noble Metal Cocatalysts

As a noble metal, Pt has been widely used as a cocatalyst in PCWS over many kinds of semiconductors including oxides [75–79], (oxy)sulfides [80–84], and (oxy)nitrides [85–88]. In all of these systems, the photocatalytic activity for hydrogen evolution is greatly enhanced. Until now, the highest photocatalytic activities for hydrogen production from water using visible light irradiation have been obtained using photocatalysts loaded with Pt as the cocatalyst [49, 50]. Other noble metals, for example, Au, [89–93] Ru, [94–96] Pd, [90, 97–99] Ag, [100–104], and Rh, [105–107] have also been employed as efficient cocatalysts. Iwase et al. [108] found that fine gold nanoparticles play an important role in creating active sites for $H_2$ evolution and enhancing charge separation. In addition, as compared to that on a Pt cocatalyst, the back-reaction between $H_2$ and $O_2$ to produce water is negligible on the Au. This phenomenon leads to improved overall water splitting photocatalytic activities of some titanate, niobate, and tantalate photocatalysts. Hara et al. [95] reported that $H_2$ evolution was unusually enhanced by Ru on a TaON photocatalyst under visible light irradiation. Note that other noble metals such as Pt, Ir, and Rh are ineffective in

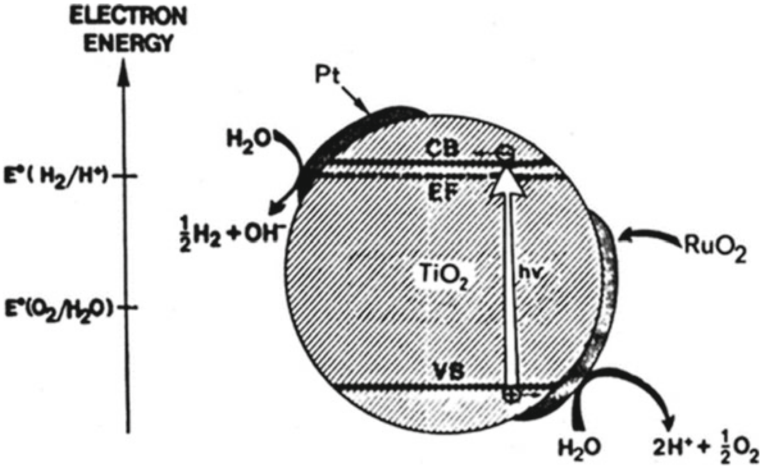

**Fig. 8** Electron and hole transfer and chemical reactions on Pt/$RuO_2$-$TiO_2$ composite catalyst

promoting $H_2$ evolution under these conditions. The authors deduced that the electronic structure of the interface facilitates electron transfer from TaON to Ru that results in charge separation.

### Transition Metal Oxide Cocatalysts

Some transition metal oxides such as $RuO_2$ [109–114] and NiO [115–118] act as efficient cocatalysts in photocatalytic reactions. Domen et al. found that β-$Ge_3N_4$ alone exhibits low photocatalytic activity [112, 119]. However, when loaded with $RuO_2$, β-$Ge_3N_4$ becomes photocatalytically active under UV irradiation ($\lambda > 200$ nm).

Borgarello et al. observed a pronounced synergistic effect on catalytic activity when both $RuO_2$ and Pt are co-deposited on $TiO_2$ particles [120]. As shown in Fig. 8, during the Pt/$RuO_2$-$TiO_2$ promoted water photosplitting reaction, Pt likely creates an ohmic contact whereas a Schottky barrier is formed by $RuO_2$. These effects direct electron flow to Pt sites and holes are trapped by $RuO_2$, resulting in enhanced charge separation.

In a series of studies, Maeda and co-workers explored the effect of loading Cr–M (M being one of the transition metals, Fe, Co, Ni, Cu, Ru, Rh, Pd, Ag, Ir, or Pt) using a co-impregnation method to form mixed oxide cocatalyst onto $(Ga_{1-x}Zn_x)(N_{1-x}O_x)$ [121–124]. The largest improvement in activity occurs by loading with the Rh–Cr mixed oxide (1 wt% Rh and 1.5 wt% Cr) followed by calcination at 623 K. It was proposed that the presence of Cr–Rh mixed oxide facilitates charge transfer from the photocatalyst to the cocatalyst. It is also possible that loading the mixed oxide also promotes the creation of active sites for hydrogen evolution, which results in the inhibition of charge recombination and enhanced photocatalytic activity [125].

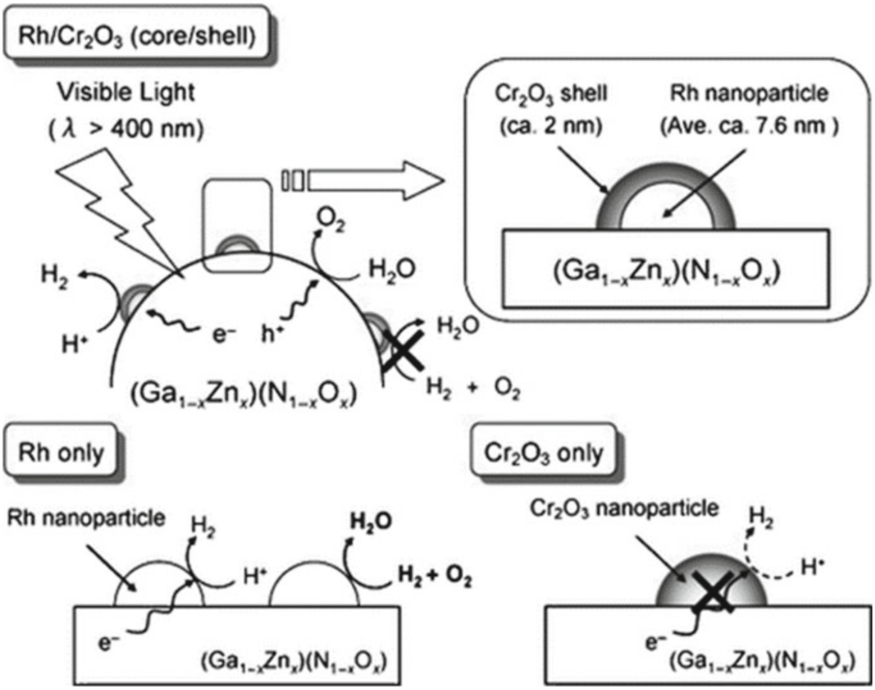

**Fig. 9** Schematic diagram of PCWS and the corresponding reactions on supported Rh and $Cr_2O_3$ nanoparticles

Maeda et al. have synthesized noble metal/$Cr_2O_3$ core/shell nanoparticles as a cocatalyst for PCWS [126–128]. Fig. 9 shows a schematic of the mechanism for overall water splitting on Rh/$Cr_2O_3$ core/shell-loaded $(Ga_{1-x}Zn_x)(N_{1-x}O_x)$. The mode of operation in this system is quite different from those containing other cocatalysts such as the Rh–Cr mixed oxide [129]. The activity enhancement is primarily due to the suppression of undesired $H_2$–$O_2$ recombination and/or $O_2$ photoreduction, and possibly protection of the core from corrosion. Among the core materials examined, Rh species exhibit relatively high performances. Interestingly, with the assistance of $Mn_3O_4$ nanoparticle co-loading, the photocatalytic activity for overall water splitting of $(Ga_{1-x}Zn_x)(N_{1-x}O_x)$, containing core/shell-structured Rh/$Cr_2O_3$ nanoparticles, is improved. In this system, $Mn_3O_4$ nanoparticles function as $O_2$ evolution sites, and Rh/$Cr_2O_3$ nanoparticles serve as $H_2$ evolution sites [130].

Tian et al. [131] investigated Pt, $RuO_2$, and $NiO_x$ nanoparticles loading on the narrow band gap photocatalysts $K_4Ce_2M_{10}O_{30}$ (M = Ta, Nb). The photocatalytic activity was markedly elevated by loading with cocatalysts, especially $NiO_x$ which creates a NiO/Ni double-layered structure. This observation resulted in enhanced electron migration from the conduction band of $K_4Ce_2M_{10}O_{30}$ to the NiO/Ni. Hwang et al. synthesized a series of metal oxide-loaded $Sr_2Nb_2O_7$ photocatalysts using the impregnation method followed by redox treatment [11]. The system that uses

$NiO_x$ as a cocatalyst was found to have the highest water splitting activity. Redox pretreatment to produce a double-layered structure is proven to be important to achieve high activity of the $NiO_x$-loaded catalysts. This phenomenon is ascribed to improved electron–hole separation by nickel in the p-type/n-type junction between $NiO_x$ and $Sr_2Nb_2O_7$ that is created by redox pretreatment. However, this marked dependence on pretreatment does not exist for other metal oxides explored in this study. Also, various metal oxides ($MO_x$: M = Cr, Mn, Fe, Co, Cu, Ru, Ag, Ce, Sm, and Pb) were included as a second component of $NiO_y$ cocatalyst to improve the activity of the photocatalyst $NiO_y$–$K_2La_2Ti_3O_{10}$. Among those fabricated, only $CrO_x$-$NiO_y$–$K_2La_2Ti_3O_{10}$ displays higher photocatalytic activity and durability over longer periods of irradiation as compared to those of the parent $NiO_y$–$K_2La_2Ti_3O_{10}$ [132].

### Nonmetal-Oxide Cocatalysts

Transition metal sulfides have been explored as cocatalysts for PCWS. Zong and co-workers showed that $MoS_2$ is a novel cocatalyst for PCWS. They found that the activity of CdS is more greatly increased by loading with $MoS_2$ than that by loading with Pt [133, 134]. In this system, coupling and formation of junctions between $MoS_2$ and CdS improves charge separation that leads to higher activity. $MoS_2$ nanoparticle cocatalysts were also found to be effective in enhancing $H_2$ evolution over CdSe nanoribbons [135].

Tabata et al. [136] found that dispersing transition metal sulfides such as NiS, FeS, $Ru_2S_3$, $Ag_2S$, CoS, and PdS increases the photocatalytic activity of $CuGa_3S_5$. It is postulated that transition metal sulfides in this system accept photogenerated electrons from $CuGa_3S_5$ for reductive conversion of $H^+$ to $H_2$.

Note that the stability of GaN:ZnO during the prolonged photocatalytic reaction (>6 months) is retained to a certain extent when an $O_2$ evolution cocatalyst is deposited on a $H_2$ evolution catalyst. For example, co-deposition suppresses oxidative deactivation of GaN:ZnO thereby prolonging its lifetime. Also, Al-doped $SrTiO_3$ with $RhCrO_x$ and $CoO_y$ cocatalysts has constant gas evolution activity during a 6 h water splitting, whereas the activity of $RhCrO_x$-loaded Al-doped $SrTiO_3$ decreases to 60% under the same conditions (Fig. 10a) [137]. The gas evolution rate of this photocatalyst coloaded with $RhCrO_x$ and $CoO_y$ using simulated sunlight remains almost unchanged over 150 h and then gradually decreases to 64% after 1000 h (Fig. 10b).

Although the dual cocatalyst tactic can be used to enhance the performance and durability of particulate photocatalysts, it must be thoughtfully applied to obtain a synergistic effect of double cocatalysts. Factors that need to be considered include careful control of the locations of the $H_2$ and $O_2$ evolution cocatalysts and meticulous optimization of the loading amount of each cocatalyst. The results of one study showed that randomly dispersed NiO on $NaTaO_3$ cubes with exposed isotropic facets is reduced in situ to form metallic Ni at reduction sites while being retained as NiO at oxidation sites. Thus, this material functions as a dual cocatalyst with a photocatalytic

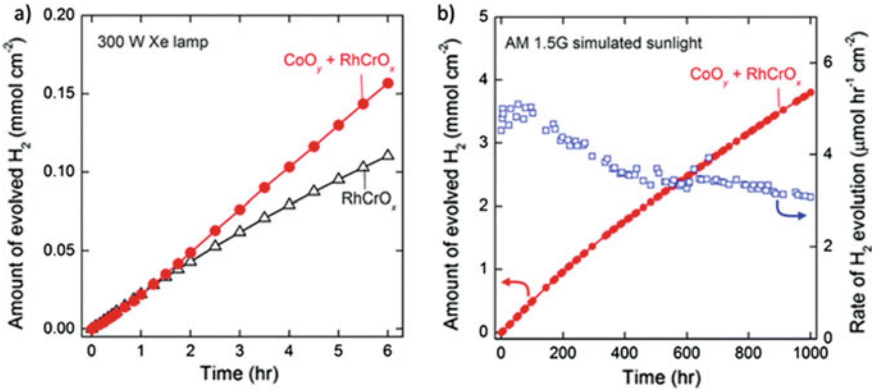

**Fig. 10** Time courses of $H_2$ production under different light irradiations. **a** 300 W Xe lamp and **b** simulated sunlight

performance that is improved over that of NiO selectively deposited only at the reduction sites of $NaTaO_3$ [138]. The balance between in situ formed Ni and NiO, as well as their locations, are important factors governing the promotion of the overall water splitting activity of $NaTaO_3$.

### 2.3.4 Light Source

Typical photocatalytic systems in laboratory studies include either internal or external irradiation-type reactors, depending on the light source used [13, 139]. Internal irradiation reactors with the longest cut-off wavelengths higher than 400 nm usually have high gas evolution rates because the particle suspensions are close to the light source. Because of irregular light intensity distribution and irradiation areas, apparent quantum yields of photocatalysts cannot be precisely measured using this reactor.

Thus, analysis of wavelength-dependent gas evolution and quantum yields requires the use of an external irradiation-type reactor [9]. The light sources used in these reactors determine the performance of the photocatalyst. Xenon (Xe) and mercury (Hg) lamps, AM1.5 G, and light-emitting diodes (LED) are the most widely used light sources in laboratory studies [3, 140–142]. However, big differences exist between these sources and, thus, developing a uniform standard is not possible. Both spectral ranges and light intensities vary greatly for different sources. Moreover, different incident photon fluxes can lead to different photocatalytic performances. As a result of these factors, most reports do not contain sufficient information to compare and evaluate the efficiencies of photocatalysts and other reactor components.

The three main deficiencies that can be identified are listed below.

(1) Ambiguous or incomplete information regarding light sources. The actual light intensity used in the experiment is as important as the light brand, type, and power.

(2) Absence of data about attenuation of incident photon flux during operation. Each light source has a specific life span. Changes in radiation output occur, thus, it is best to measure light intensity at both the start and end of the test period. If the light source is decaying, photon flux may decrease significantly over the operation time.

(3) Incomplete description of the configuration of the light source and reactor. The actual light intensity reaching the reaction surface greatly depends on the material the reactor is composed of, the distance between the light source and the reactor, and the irradiated area of the reactor. Even using the same weight of photocatalyst, different irradiation areas with different suspension conditions can lead to diverse photocatalytic performances.

The lack and inconsistency of accurate information regarding the light source prevent comparisons of experimental results. It has been shown that irradiation at different wavelengths, even within the same visible wavelength range, can lead to different photocatalytic performances (Fig. 11 a) [143]. Also, when the light intensities are different, the rate of $H_2$ production varies significantly even for the same photocatalyst (Fig. 11 b). Moreover, different light sources may promote different reaction mechanisms [144, 145]. Therefore, details on the wavelength of the light source, light intensity or density, and irradiation area on the surface of the photocatalytic system need to be specified.

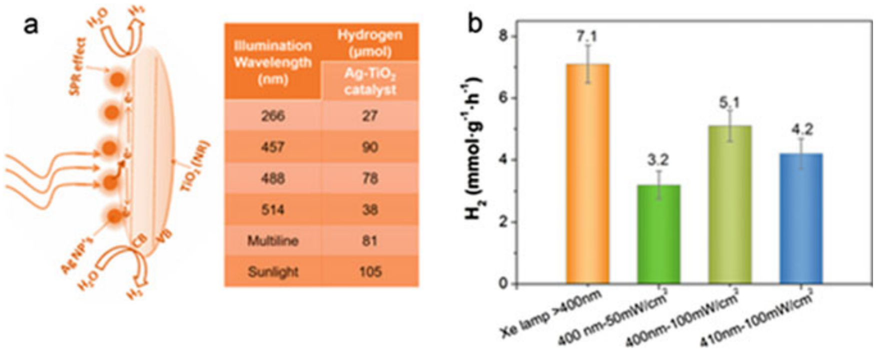

| Illumination Wavelength (nm) | Hydrogen (μmol) |
|---|---|
| | Ag-$TiO_2$ catalyst |
| 266 | 27 |
| 457 | 90 |
| 488 | 78 |
| 514 | 38 |
| Multiline | 81 |
| Sunlight | 105 |

**Fig. 11** **a** $H_2$ production under different lighting conditions. **b** The efficiency of the photocatalytic dehydrogenation of formic acid ($H_2$ production) at different wavelengths or intensities for Pt/$C_3N_4$ photocatalyst after 5 h of irradiation

# 3 Materials Used for PCSS

## 3.1 *Introduction (Material Type, Synthesis, Structure, Characteristic Properties, and Performance in Seawater Splitting)*

Hydrogen, a clean and storable energy source with a high energy density of 142 MJ $kg^{-1}$, through photochemical water splitting with abundant seawater would address challenging issues such as the increasing energy demand and depletion of fossil fuels. In addition, it could also alleviate the consumption of scarce fresh water and have use in arid coastal areas. In this chapter, the earth-abundant photocatalysts including $TiO_2$, conjugated polymers, solid solution materials, and other semiconductor nanomaterials that have been developed for seawater splitting are discussed.

## 3.2 *$TiO_2$-based Materials*

Due to merits associated with high stability, low cost, and low toxicity, $TiO_2$-based photocatalysts have attracted extensive attention and have become the most widely used for PCSS. All reported $TiO_2$ photocatalysts are based on structure design, modification by other semiconductors, defect engineering, and so on.

In a series of studies on PCSS using $TiO_2$ materials, Yang et al. [146] using calcination at high temperatures prepared nano-$TiO_2$, referred to as $TiO_2$-OH, a material that has surface hydroxyl groups and high crystallinity. The morphology and structure of $TiO_2$-OH revealed by TEM images consist of aggregates of uniform $TiO_2$ nanocrystals with uniform sizes ranging from 30 to 40 nm. As can be seen in the magnified TEM images (Fig. 12a, b), single $TiO_2$ nanocrystals contain inner defect-like pores with a size of about 4 nm. Experimental measurements show the $TiO_2$-OH has defects (Fig. 12c). The rich array of surface hydroxyl groups and Ti-vacancies in $TiO_2$ significantly enhance its activity in photocatalytic $H_2$ production from (sea)water (Fig. 12d). [146, 147] Their group also developed a low-temperature method to introduce oxygen/metal vacancies in $TiO_2$ that increase the interfacial n-p effect. Interfacial n-p homojunctions of $TiO_2$ are fabricated by directly decorating interfacial p-type $TiO_2$ with Ti-vacancy around n-type $TiO_2$ nanocrystals.

Beads of $TiO_2$ that are calcined at 350 °C show a uniform diameter of about 500–600 nm (Fig. 13a) and consist of uniform nanoparticles with a diameter of about 15 nm (Fig. 13b). The nanocrystals with a size of around 8–10 nm (Fig. 13c, blue areas) are bonded together through an interconnecting amorphous/semi-crystalline interface of around 1–4 nm (Fig. 13c, yellow areas). The amorphous/semi-crystalline/highly crystalline phase can be well visualized by viewing the HRTEM image and inverse FFT in Fig. 13d, e. This highly crystalline/semi-crystalline/amorphous phase is coherent

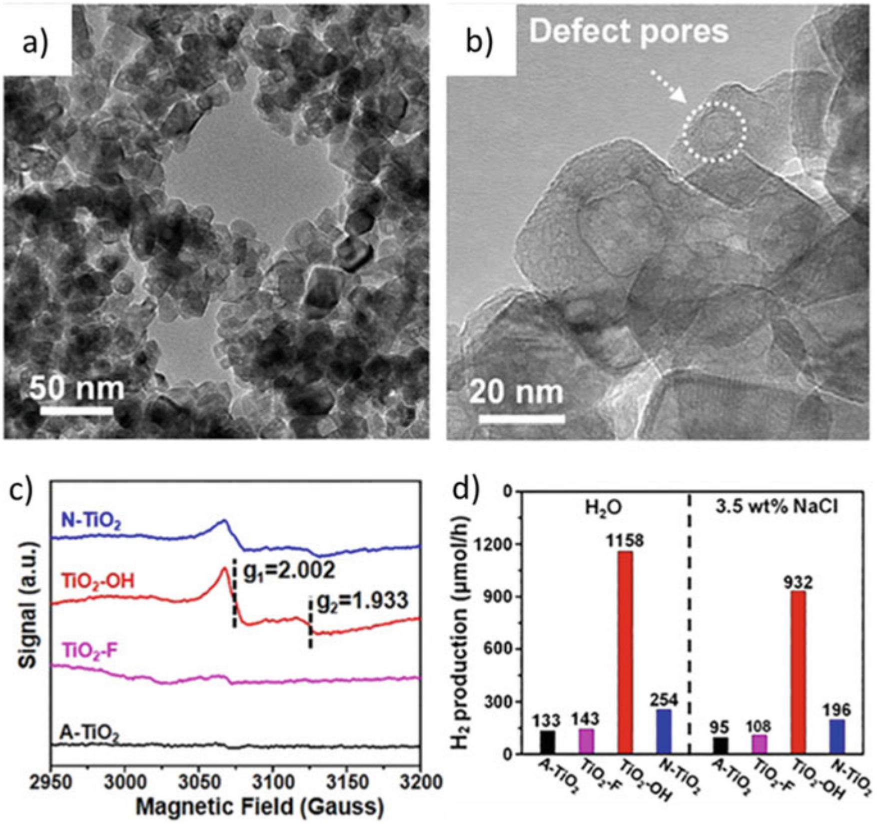

**Fig. 12** **a**, **b** TEM images of $TiO_2$-OH, **c** EPR spectra, and **d** photocatalytic $H_2$ production rates from (sea)water of different samples

at the atomic scale, and defect generation mainly occurs at the interface region. In the EPR spectrum of $TiO_2$-350, the sharp peak corresponding to $g_{yy} = 2.001$ is assigned to oxygen vacancies and the high intensity of this peak means that $TiO_2$-350 has the highest level of oxygen vacancies of all the samples treated at different temperatures. The EPR signals at $g_{zz} = 2.020$ and $g_{xx} = 1.98$ are attributed to $O^{2-}$ and $Ti^{3+}$.

To determine the Ti-vacancies in $TiO_2$, Yang et al. performed a 2D1H TQ-SQ magic-angle spinning (MAS) NMR experiment. Signals in the spectrum at (7.10, 7.10 + 7.10 + 1.84) (Fig. 14a) demonstrate the presence of Ti–OH species near the solid surface ($\delta_H = 1.84$ ppm) exist in $TiO_2$-A, and Ti–OH species from broken Ti–O–Ti bonds ($\delta_H = 7.10$ ppm) which were forming hydrogen bonds. At 250 °C, the signals at (6.00, 6.00 + 6.00 + 6.00) (Fig. 14b) show that Ti-vacancies start to form, and Ti–OH species from broken Ti–O–Ti bonds and surface Ti–OH groups are in the phases. When the temperature reaches 350 °C, Ti–OH nests remain and almost no other Ti–OH species are present in the bulk (Fig. 14c). Further increasing

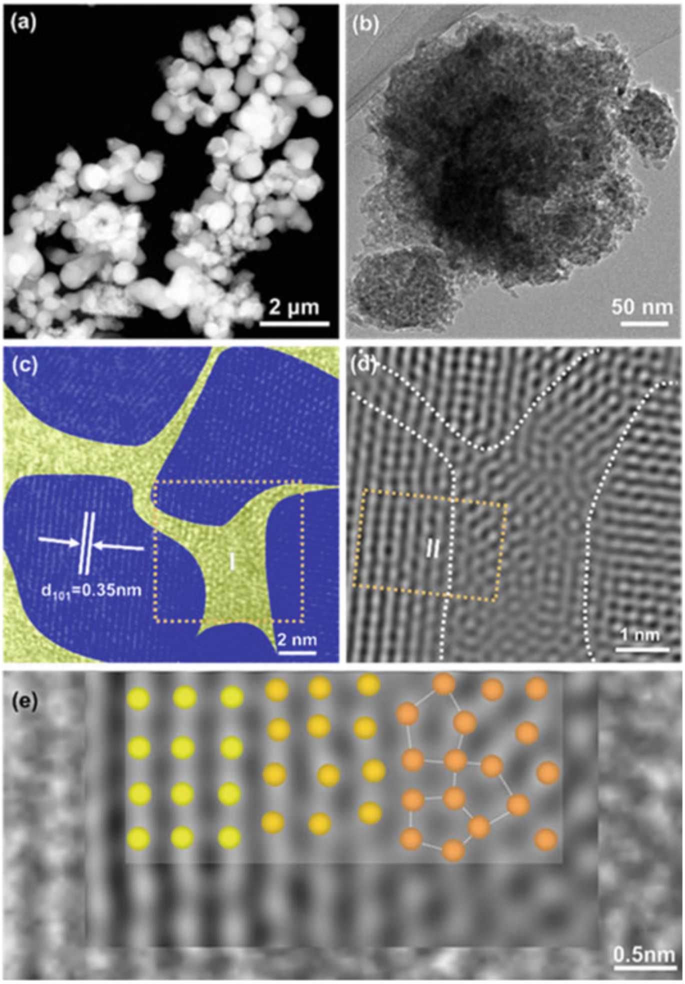

**Fig. 13** The morphology of $TiO_2$ via TEM and corresponding Inverse FFT

the temperature only causes the loss of Ti–OH nests, and only Ti–OH species from broken Ti–O–Ti bonds and surface Ti–OH species remain (Fig. 14d–h).

As foreign phase-junctions, nanocarbons are very efficient dopants for semiconductor fabrication [148, 149]. Yang et al. found that graphene nanosheets or nanodots can capture oxygen atoms of $TiO_2$ thereby creating O- and Ti-vacancies. This group developed a two-step calcination treatment, involving starting at 500 °C calcination in an Ar flow and followed by 350 °C calcination in air. Application of this procedure enabled the formation of a junction of O-vacancies and Ti-vacancies in $TiO_2$ with the assistance of reduced graphene oxide (rGO) sheets [150]. As shown in Fig. 15a, rGO sheets have a thickness of about 3–5 nm that is intimately coated on the external

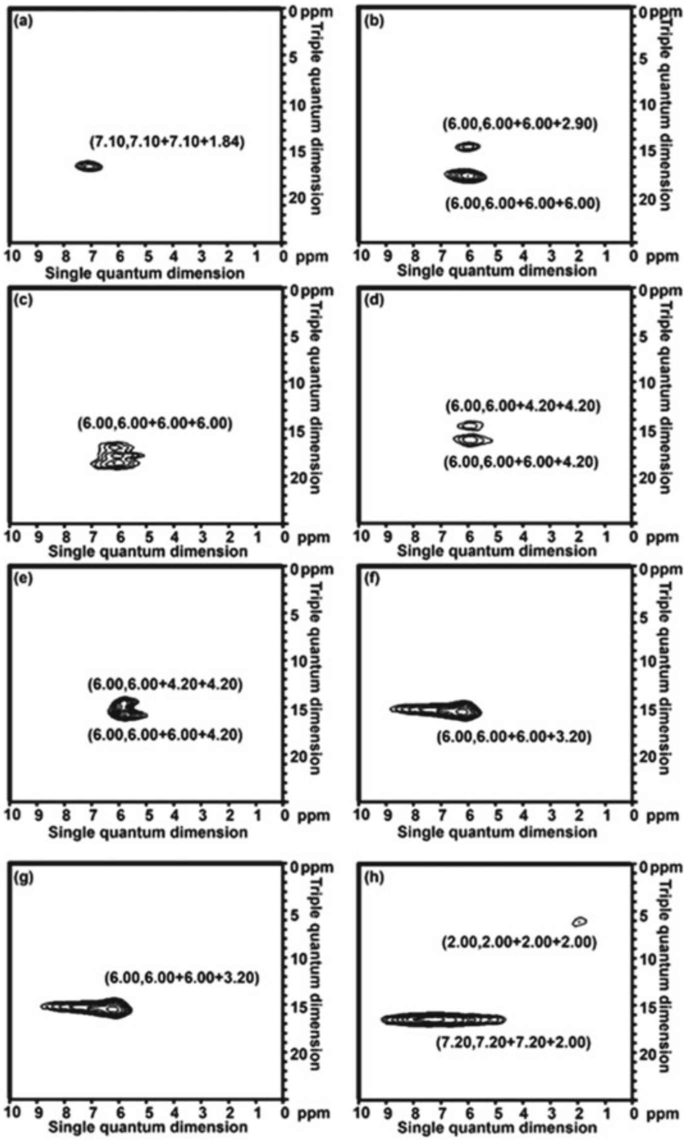

**Fig. 14** 1H TQ-SQ MAS NMR spectra of **a** $TiO_2$-A, **b** $TiO_2$-250, **c** $TiO_2$-350, **d** $TiO_2$-450, **e** $TiO_2$-550, **f** $TiO_2$-650, **g** $TiO_2$-750, and **h** $TiO_2$-850

surface of $TiO_2$ beads (Fig. 15a). It also shows a strong electron paramagnetic resonance (EPR) signal at $g = 2.002$ in the spectrum of $TiO_2$@rGO, which is attributed to O-vacancies in $TiO_2$ lattices, while the weak signal at $g = 1.965$ in that of $TiO_2$@rGO is related to the $Ti^{3+}$ defects associated with O-vacancies (Fig. 15b) [151]. Interfacial junction of O-vacancies and Ti-vacancies significantly enhances *t* transport of

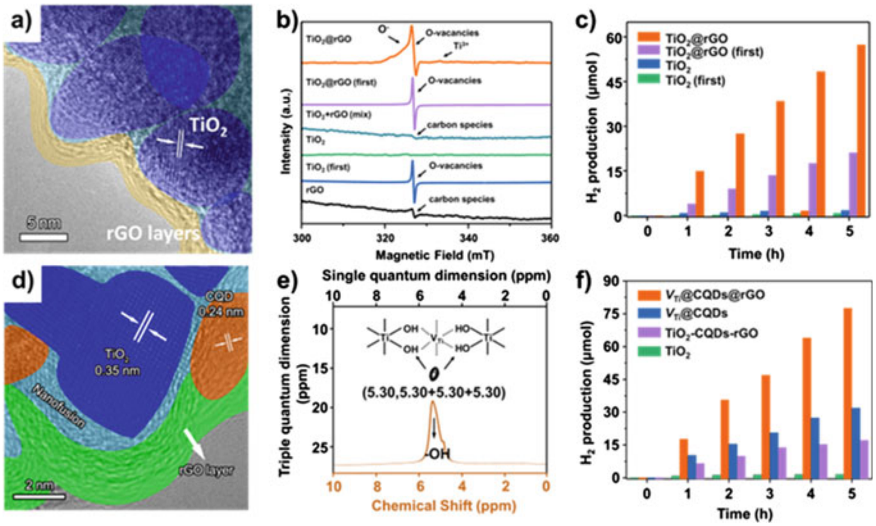

**Fig. 15** **a**, **d** Structure, **b**, **e** defects, and **c**, **f** photocatalytic $H_2$ production from PCSS

interfacial carrier. The final sample exhibits a $H_2$ production rate of 570 $\mu$mol/h g$^{-1}$ from seawater splitting (Fig. 15c).

Next, Yang and co-workers constructed a spatially ternary titanium-defected $TiO_2$@carbon quantum dots@reduced graphene oxide (denoted as $V_{Ti}$@CQDs@rGO) to demonstrate the cascade effect of charges [152]. The clear lattice fringes of $TiO_2$ and CQDs in the HRTEK image are in agreement with the anatase $TiO_2$ (101) planes and (110) lattice fringes of graphite, respectively (Fig. 17d). The uniform distribution of CQDs in overall mesostructured $TiO_2$ nanocrystals and outer coating of rGO can be clearly observed in this image. The Ti–OH nests with pairs of off-diagonal peaks at (5.3, 5.3 + 5.3 + 5.3) and (5.5, 5.5 + 5.5 + 5.5) appear in $V_{Ti}$@CQDs@rGO (Fig. 17e), which are attributed to Ti–OH nests referring to the Ti-vacancies, and almost no other Ti–OH species are present [153]. As components of the photo-energy conversion efficiency ($\eta_c$) of the cascade photo-conversion system, charge separation efficiency ($\eta_{cs}$) depends on the charge separation from the inner lattice to the Ti-vacancies, charge separation efficiency ($\eta_{ct}$) depends on the charge transport from the Ti-vacancies to the CQDs, and charge utilization efficiency ($\eta_{cu}$) depends on the charge collection and utilization from the CQDs and $TiO_2$ nanocrystals to the rGO sheets. This spatial heterojunction exhibits a $H_2$ production rate of 750 $\mu$mol/h g$^{-1}$ from seawater splitting, which is 4.4-fold higher than that arising from a random surface heterojunction (Fig. 17f).

Zeng et al. [30] display an uncomplicated post-processing method to synthesize a $Ti^{3+}$ self-doped titanium-silicon material with corrosion resistance. These workers demonstrated that Ti–O–Si materials created using different calcination temperatures serve as a highly efficient and convenient catalyst for the photogeneration of hydrogen from water and simulated seawater. The optimized Ti–O–Si (400) material has an impressive 10-times enhanced photocatalytic $H_2$ production performance that is 43.1 times that of $TiO_2$ nanoparticles in water and simulated seawater.

Yang et al. [154] developed nonmetal plasmonic $MoS_2@TiO_2$ heterostructures for highly efficient photocatalytic $H_2$ generation. A combination of physical vapor deposition (PVD) and chemical vapor deposition (CVD) strategies was used to create few-layered $MoS_2$ nanoflake uniform coatings of different thicknesses on the inner surface of anodized $TiO_2$ nanocavities (referred to as $MoS_2@TiO_2$) to produce a highly ordered 3D hierarchical configuration (Fig. 16a). CVD sulfurization was carried out at 400 °C for 10 min on these coated $TiO_2$ arrays (abbreviated as $MoS_2(10)@TiO_2$, $MoS_220)@TiO_2$, $MoS_2(30)@TiO_2$, respectively). In the bright-field (BF) STEM image of $MoS_2$ nanoflakes shown in Fig. 16b, a relationship with respect to the atomic number (Z) reveals the presence of sandwich structured $MoS_2$ and S-vacancies identified by blue dashed circles and blue arrows in Fig. 16c. These structures display intense LSPR throughout regulating the S stoichiometry of $MoS_2$ surfaces. The photocatalytic activities of members of the series of $MoS_2@TiO_2$ cocatalysts for $H_2$ under simulated solar light illumination (Fig. 16d, e). Pure $TiO_2$, sulfurized $TiO_{2,}$ and $MoO_3@TiO_2$ hybrid are nearly photocatalytically inert toward $H_2$ production, associated with a reaction rate lower than 10 μmol $h^{-1}$. Notably, photocatalytic activity is greatly enhanced by the presence of the $MoS_2$ loading, reaching a maximum value of 84 μmol $h^{-1}$ for $MoS_2(30)@TiO_2$ which is 8 times larger than that of pure $TiO_2$.

Ho et al. designed the $SiO_2/Ag@TiO_2$ core–shell solar thermal collector that possesses photothermic properties needed for highly targeted interfacial phase transition reactions that are synergistically favorable for both seawater splitting and desalination reactions [34]. In Fig. 17a is shown the photocatalytic performance trend in simulated seawater under full spectrum irradiation. Both $SiO_2@TiO_2$ and $TiO_2$ spheres undergo increases from 156 μmol $g^{-1}$ $h^{-1}$ to 192 μmol $g^{-1}$ $h^{-1}$ and from 138 μmol $g^{-1}$ $h^{-1}$ to 156 μmol $g^{-1}$ $h^{-1}$, respectively. $H_2$ generation rates for the splitting of simulated seawater catalyzed by all three materials are lower than those for the splitting of pure water.

In this effort, chloride concentration as a function of time was measured during photocatalytic hydrogen generation reaction of the SiO during the photocatalytic hydrogen generation reaction during the photocatalytic hydrogen generation reaction catalyzed by the $SiO_2/Ag@TiO_2$ core–shell nanocomposite during the photocatalytic hydrogen generation reaction using a chloride ion selective electrode. Hydrogen is produced at a steady rate of 370 μmol $g^{-1}$ $h^{-1}$ under UV light irradiation and 857 μmol $g^{-1}$ $h^{-1}$ under full solar spectrum irradiation (Fig. 17). Concomitantly, the chloride concentration remains unchanged throughout the process (Fig. 17b) and, hence, no chloride derived compounds are produced. Based on these findings, seawater collected from the Strait of Singapore, combined with glycerol in a 20% v/v ratio, was subjected to photocatalytic hydrogen production. The results show that the photocatalytic performance using actual seawater was better than that utilizing simulated seawater. The second issue assessed is the stability of the photocatalyst. These workers found that the hydrogen generation rate remains relatively constant

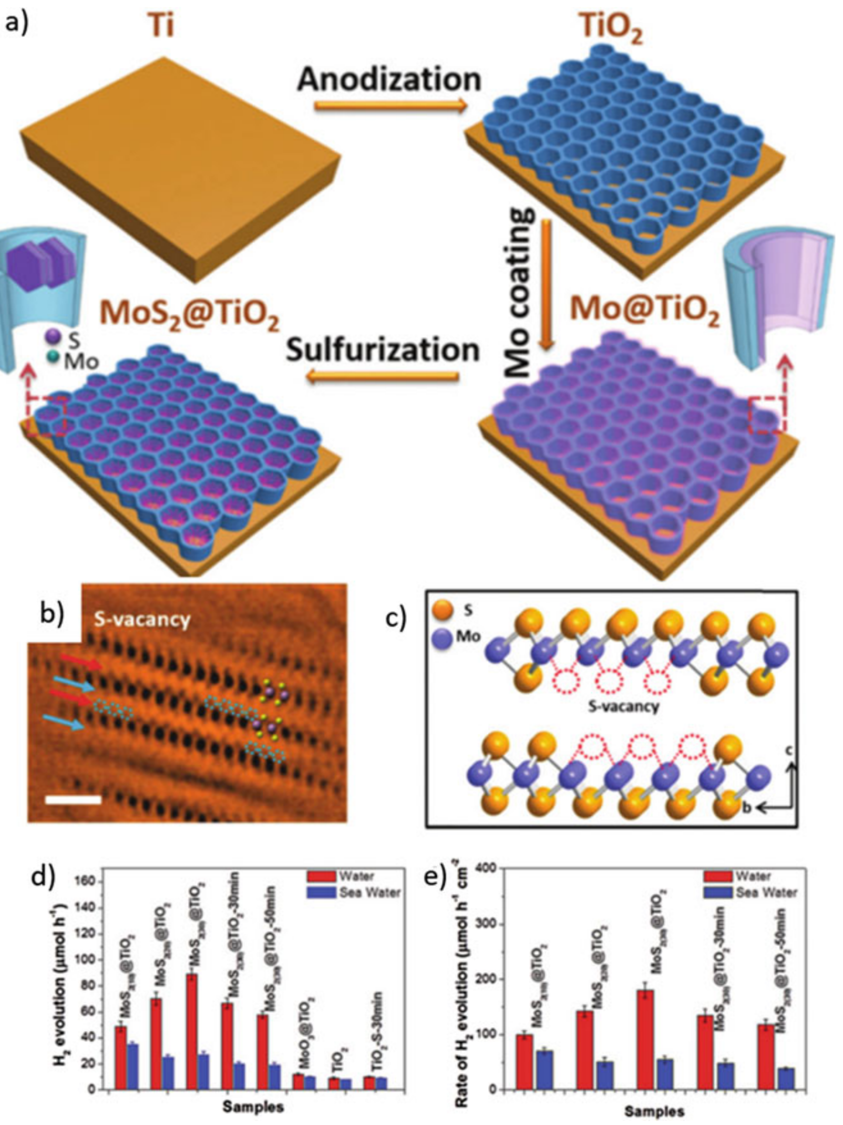

**Fig. 16** **a** Synthesis process of the $MoS_2$@$TiO_2$ heterostructure. **b**, **c** BF-STEM image, and **d**, **e** $H_2$ production rate over different samples in water and seawater condition

at about 7% during the process (Fig. 17c) which suggests that the $SiO_2$/Ag@$TiO_2$ core–shell nanocomposite is chemically stable during seawater splitting.

Wu et al. [155] investigated the Pt/GaP-$TiO_2$-$SiO_2$:Rh (PGTSR) composite composed of the $d^0$ metal oxide photocatalyst $TiO_2$ and $d^{10}$ photocatalyst (GaP). The noble metal Pt and supporter $SiO_2$ are employed to enhance the transfer of the

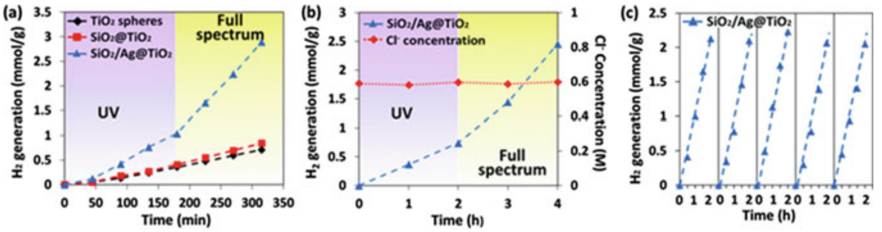

**Fig. 17** **a** $H_2$ production of different samples in simulated seawater. **b** $H_2$ production and chlorine concentration of $SiO_2/Ag@TiO_2$. **c** Cycling test for $H_2$ production

photogenerated electrons and the adsorption capacity of the composite. The photocatalytic performance and stability of the prepared photocatalyst were evaluated by measuring the hydrogen and oxygen generation from pure water or seawater in a single photoreactor without using sacrificial agents. This PCSS system achieved a HER/OER ratio of 41.5/26.1 $\mu$mol $g^{-1}$.

### *3.3 Polymer-Based Materials*

A series of water splitting systems that utilize UV light have been developed since 1980. However, it is unlikely that STH efficiencies of these systems will reach the threshold value required to make the cost of hydrogen production by this process competitive with those of fossil fuels [156]. UV light (i.e., $\lambda < 400$ nm) only accounts for approximately 5% of the solar spectrum. In contrast, visible light (400 nm $< \lambda <$ 800 nm) represents more than 50% of the solar spectrum, and close to a 16% STH efficiency is possible by using visible light-absorbing photocatalysts that utilize >600 nm sunlight with 100% efficiency [157]. Therefore, developing long-wavelength-responsive photocatalysts is a critical aspect of truly efficient renewable hydrogen production.

Conjugated polymers are new types of photocatalysts that have been developed for water splitting since they have similar band structures with semiconductors. Early studies primarily of these materials focused on the photocatalytic half-reactions promoted by polymeric carbon nitride (PCN) [158, 159]. After persistent efforts, by loading suitable cocatalysts on PCN loaded with suitable cocatalysts were identified that promote water splitting using both UV and visible light [160]. In addition, single-site cocatalysts have been found to significantly improve catalytic performance. A conjugated polymer, comprised of 1,3-diyne-linked conjugated microporous polymer nanosheets (CMPNs) and synthesized via the oxidative coupling of terminal alkynes, was found to function as a visible light-responsive photocatalyst for overall water splitting [161]. Although the efficiencies of processes promoted by conjugated polymers are relatively low, their performances can be improved by using the crystallinities of the polymers [162]. In addition, the incorporation of functional groups can be used to tune band gaps and enhance charge separation, and high-efficiency cocatalysts, doping, and morphologic control can be employed to enhance activities.

In 2015, Kang et al. [163] described the design and fabrication of a metal-free carbon nanodot-carbon nitride ($C_3N_4$) nanocomposite and demonstrated its impressive performance for photocatalytic-solar water splitting. The measured wavelength-dependent quantum efficiencies of the system are 16% for $\lambda = 420 \pm 20$ nm, 6.29% for $\lambda = 580 \pm 15$ nm, and 4.42% for $\lambda = 600 \pm 10$ nm, and the overall solar energy conversion efficiency is 2.0%. Even though seawater was not used for these measurements, they highlight the bright future that this low-cost, Earth-abundant, environmentally friendly, and stable material has in $H_2$ production.

Xiang et al. [164] developed the organic hybridized photocatalyst, COP-TF@CNi$_2$P), comprised of a carbon-encapsulated nickel phosphide, as a cocatalyst loaded on a fully conjugated organic polymer (Fig. 18a). COP-TF@CNi$_2$P exhibits has a photocatalytic $H_2$ evolution rate up to 2500 $\mu$ mol $g^{-1}$ h $^{-1}$ ($\lambda \geq 400$ nm) using seawater and it maintains 92% of its initial efficiency after 16 intermittent cycles occurring over a half month (Fig. 18b, c). The excellent activity and long-term stability of this material are ascribed to the presence of a tight combination between CNi2P and pristine COP-TF, which is conducive to the transfer of photoexcited electrons to the surface of CNi$_2$P and its resistance to shedding during photocatalytic hydrogen evolution.

Huang et al. [165] reported the results of a study of an electrostatically induced supramolecular approach in which small molecules form self-assembled superstructures as they provide a platform for loading Pt nanoparticle catalyst and facilitate charge transfer. This group took unprecedented advantage of chloride ions in seawater to promote superstructure formation by their electrostatic interactions with the fine-designed conjugated small-molecule PorFN. The observations show that the photocatalytic activity of the system in simulated seawater reached 10.8 mmol $h^{-1}$ $g^{-1}$.

Yu et al. [166] described the thioether-functionalized covalent organic framework, TTR-COF, and its use in visible light-driven photocatalytic $H_2$ production from seawater (Fig. 19a). Owing to the specific affinity of thioether groups for Au ions, TTR-COF selectively adsorbs Au over other alkaline and alkaline-earth metal cations in seawater, to produce a uniform loading of Au as a cocatalyst. This loading along with the highly conjugated structure containing triazine units in TTR-COF contributes to enhancing the visible light harvesting and photoinduced charge generation and separation ability, as well as the stability of the system. The results suggest that COFs have great potential for photocatalytic $H_2$ production from seawater. TTR-COF also has an ability to selectively capture Au ions over other common transition and basic metal ions (Fig. 19b). The $H_2$ evolution capacity of TTR-COF is up to 1720 $\mu$ mol $g^{-1}$ in a 4 h reaction and is stable at that level for at least 20 h (Fig. 19c). Moreover, TTR-COF displays continuous and stable $H_2$ production of 501 $\mu$mol $g^{-1}$ and an $H_2$ evolution rate of 141 $\mu$mol $h^{-1}$ $g^{-1}$ over a 20 h irradiation

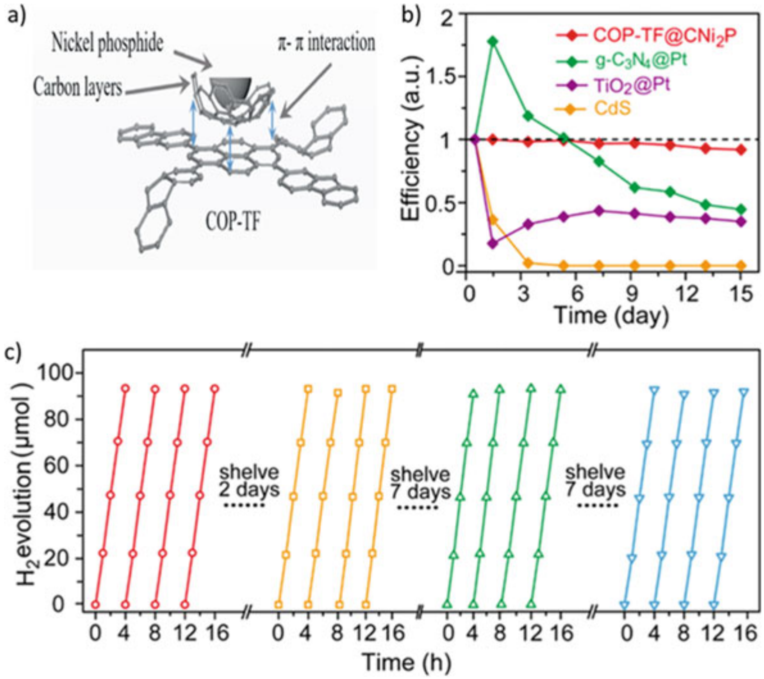

**Fig. 18** **a** Structure diagram of $CNi_2P$ and COP-TF. **b** Photocatalytic stabilities of different samples in seawater. **c** Cycling test of $H_2$ production from seawater

time (Fig. 19d), although a relatively higher $H_2$ evolution rate was obtained using TFPT-COF (Fig. 19e).

Babu et al. [167] demonstrated the success of solar seawater splitting by using a two-dimensional polymer catalyst derived from metalloporphyrin-bearing multi-hydroxyl groups. A bimetallic (Co and Ni) derivative of the porphyrin 2D-polymer exhibits excellent long-term durability over 15 cycles of $H_2$ and $O_2$ generation in 200 d from pure water. Detailed studies using rivers and seawaters also show that the catalyst has reliable performance over repeated cycles.

Studies by Lyutakov et al. [168] resulted in the formation of rationally designed two-dimensional (2D) flexible heterostructures with photocatalytic activity for the production of "clean" hydrogen under NIR illumination. The system displays a hydrogen production rate exceeding that of most other 2D materials and it has the ability to use the seawater. The material has a hybrid bimetallic (Au/Pt) periodic structure, which is covalently grafted with a metal–organic framework MIL-101(Cr). The periodic gold structure effectively supports a plasmon-polariton wave to excite the hot electrons, which are injected into the Pt and MIL-101(Cr) layers. The Pt and MIL-101(Cr) structures contain catalytic sites, which are saturated with hot electrons that efficiently initiate water splitting and hydrogen production. The MIL-101(Cr) layer also serves to repel generated hydrogen bubbles. The results of mechanistic studies

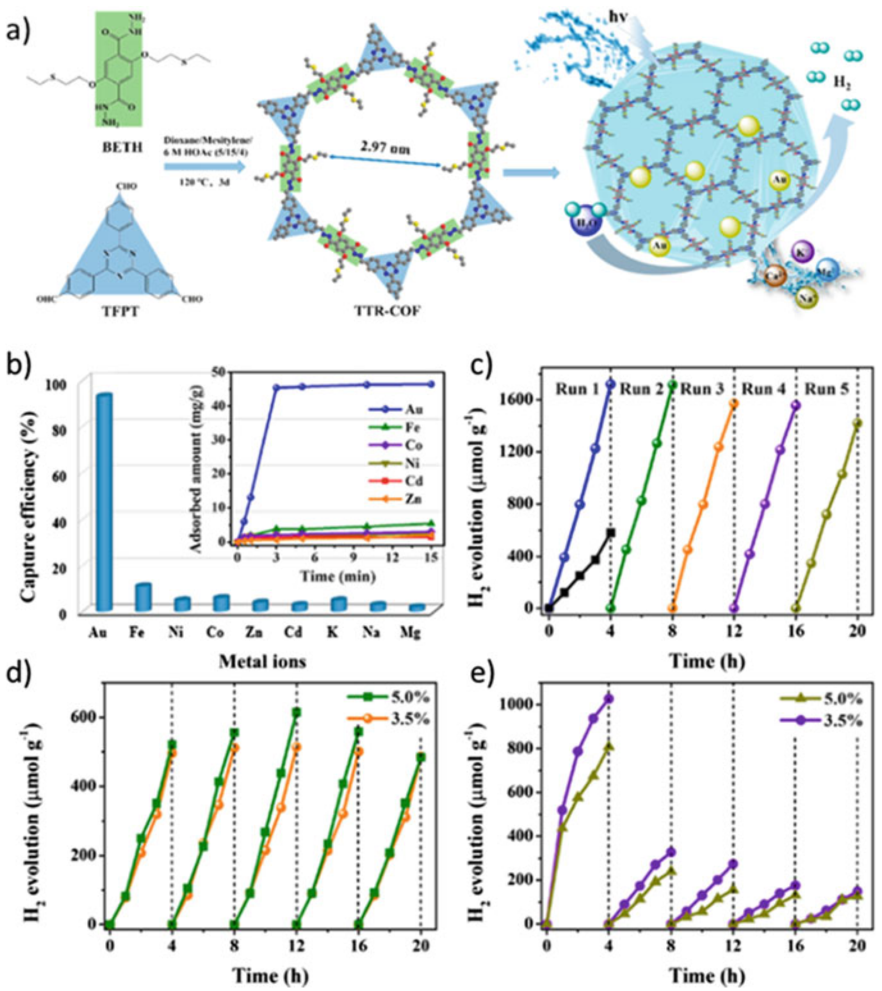

**Fig. 19** **a** Synthesis and application of TTR-COF in PCSS. **b** Capture efficiency for various metal ions of TTP-COF from $H_2O$. Inset: adsorption curve of various metal ions, **c** Photocatalytic performances of TTR-COF and TTB-COF (black) in water, Photocatalytic performances of **d** TTR-COF and e) TTB-COF (black) in seawater conditions

reveal the catalytic role played by every element in the 2D flexible heterostructures. A maximum hydrogen output was achieved under plasmon resonance excitation in the NIR range, and it could be controlled by varying the applied LED wavelength. Moreover, water or seawater is converted into $H_2$ at 193.5 $\mu$mol h$^{-1}$ cm$^{-2}$ rate under irradiation with the NIR part of the solar spectrum.

## 3.4 Solid Solution-Based Materials

Solid solution photocatalysts can optimize the band structures of materials, leading to a reduction of the band gap of photocatalysts, broadening the light absorption range, and improving the sunlight utilization rate. Thus, these photocatalysts provide a more controllable way to realize continuous regulation of the physicochemical properties of materials [169, 170]. Furthermore, their optimized band structures may promote the delocalization of photogenerated electrons, which boosts diffusion and disconnection of photogenerated carriers and improvement of photocatalytic performances [171]. Finally, solid solution materials enable better adjustability in compositions and structures than single component materials which considerably affect photocatalytic performance [172].

K. Domen was the first to use a solid solution as a photocatalyst for overall water splitting under visible light irradiation ($\lambda > 400$ nm). [173] To devise a new $d_{10}$-(oxy)nitride having a visible light response, the attention of this group initially focused on gallium nitride (GaN). Since both GaN and ZnO have wurtzite structures with similar lattice parameters [174, 175]. They participate in forming a solid solution (Fig. 20a). The expected band structure of the GaN–ZnO solid solution ($(Ga_{1-x}Zn_x)(N_{1-x}O_x)$) is illustrated in Fig. 20b [23]. Experiments confirmed that by using Xe (300 W) irradiation, the GaN:ZnO photocatalyst system functions at wavelengths as long as 460 nm and has an average apparent quantum efficiency in the range of 300–480 nm of 0.14% [173]. Upon modification by using suitable cocatalysts (such as $RH_{2-y}Cr_yO_3$), GaN:ZnO becomes active for the $H_2$ evolution under visible light ($400 < \lambda < 500$ nm). The rate of visible light water splitting producing $H_2$ and $O_2$ continuously in stoichiometric amounts remains unchanged for 3 months (2160 h). After 6 months of operation, a 50% loss of initial activity occurs. Regeneration of deactivated catalysts was attempted by the reloading of the $RH_{2-y}Cr_yO_3$ cocatalyst. The degree of activity regeneration was found to depend on the reloading amount, with up to 80% of the initial activity for $H_2$ evolution being recovered optimally. It was also found that the deactivation of GaN:ZnO is suppressed to some extent by prior co-loading of an $O_2$ evolution cocatalyst, which helps to suppress oxidative decomposition of GaN:ZnO by valence band holes, thereby improving durability [176]. Furthermore, these workers investigated the effects of electrolytes on photocatalytic activity in seawater [177]. The cocatalyst $RH_{2-y}CryO_2$ was found to selectively promote photoreduction of $H^+$, while $RuO_2$ functions as both $H_2$ evolution and efficient $O_2$ evolution sites.

Zhang et al. [178] employed a simple mechanical mixing method to combine $Cd_xZn_{1-x}Se$ and CoP. They found that the $Cd_xZn_{1-x}Se$ energy band could be tuned by changing Cd concentrations due to the acceptance of photoelectrons on CoP nanoparticles. The higher CB generates electrons with stronger reduction capacity for $H_2$ evolution. Considering various electrolytes exist in natural seawater besides NaCl, Li et al. studied possible reactions of ions during the photocatalytic process. These workers synthesized $ZnS_{1-x-0.5y}O_x(OH)_y$–ZnO photocatalyst with NiS loading by using two methods [179]. When $Na_2S{\cdot}9H_2O$ and $Na_2SO_3$ are added as sacrificial

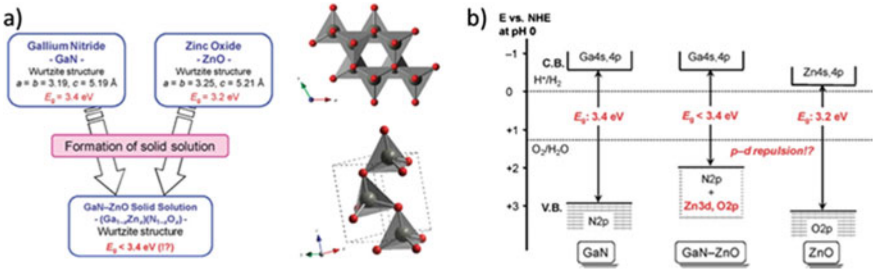

**Fig. 20** **a** Crystal data and structure of GaN and ZnO and **b** band structures of different samples

agents to seawater, a precipitate of a mixture of $Mg(OH)_2$ and $CaSO_3$ is produced. Although the surfaces of both the precipitate and photocatalyst are negatively charged in the seawater-electron donor reaction system, part of the precipitate particles cover the active sites of the photocatalyst. The precipitate can also screen light absorbed by the photocatalyst. The surface charge of the modified photocatalyst changes to more negative when NiS loaded, which leads to decreasing coverage of the photocatalyst surface with the precipitate particles due to increased electrostatic repulsion. Thus, the detrimental effect of precipitation decreases, and the photoactivity of the modified photocatalyst in seawater-electron donors with the precipitate is higher than that in pure water-electron donors without the precipitate.

Chai et al. [180] prepared a photocatalytic system comprised of p-doped $Zn_{0.5}Cd_{0.5}S$ (pZCS) and CoP as a noble-metal-free cocatalyst for photocatalytic HER in both pure water and seawater. Through a series of detailed characterization experiments, they deduced that the P atoms interstitially doped into the lattice framework amplify the S-vacancies present in ZCS. The electron trapping effect becomes even more pronounced because the P dopant shifts the Fermi level to a location that is in closer proximity to the midgap state. The multiple extents of electron entrapment within the composite result in highly efficient HEP in pure water and 3864.1 $\mu$mol $g^{-1}$ $h^{-1}$ in seawater. Overall, this study offers new insight into photocatalytic seawater splitting by highlighting a new approach to produce a composite that functions as an innate dual-stage electron trapping system for hindering charge carrier recombination.

Huang et al. [181] prepared $Cd_{0.5}Zn_{0.5}S/Ti_3C_2$ composites containing $Ti_3C_2$ nanosheets that have excellent metal conductivity with $Cd_{0.5}Zn_{0.5}S$ to form a non-precious Schottky photocatalyst. The rate of hydrogen production promoted by this composite in seawater is 9.071 mmol $g^{-1}$ $h^{-1}$, which is 33 times higher than that of Pt-loaded photocatalysts in seawater. In addition, Silva [182] prepared selenium/selenide containing Cd and Zn in aqueous solution at room temperature by using co-precipitation. The cubic structure formed has a wide size distribution of CdSe and ZnSe solids and produces 16% more hydrogen in natural seawater with added lactic acid as a sacrificial agent than in deionized water. The hydrogen production rate of $Cd_{0.5}Zn_{0.5}S_{0.1}Se_{0.9}$ is 350 umol $g^{-1}$ $h^{-1}$, and the CdSe composite $Zn_5(OH)_8Cl_2 \cdot H_2O$ produces hydrogen at a rate of 395 umol $g^{-1}$ $h^{-1}$. Based on considerations of a computational phase diagram, band gap, and band edge position, Gerbrand Ceder et al. [183] devised the solid solution $Ta_{3x}Ti_{3-3x}O_{3-3x}N_{2+3x}$ as a promising water splitting photocatalyst. The minimal band gap is around 2.0 eV, indicating that high efficiency under solar illumination may be achieved.

## *3.5 Other Types of Materials*

Wu et al. [184] designed and synthesized few-layer heterostructure $ReS_2$ nanosheets with a lateral metallic T and semiconducting Td phase interface, in which cationic vacancies are intentionally introduced as active sites. Six representative samples of seawater of different salinities including 0.8 (Baltic Sea), 2.8 (Yellow Sea), 3.6 (Caribbean Sea), 3.9 (Arabian Sea), 10 (Dead Sea), and 36wt% (saturated salt solution) were analyzed. The plot in Fig. 21a shows that the $H_2$ production rate increases with increasing salinity. The process promoted by T3 in saturated salt solution exhibits the highest hydrogen evolution activity with a hydrogen production rate of 216 $\mu$mol $cm^{-2}$ $h^{-1}$, and the hydrogen production efficiency in Arabian seawater is slightly larger than that in freshwater (0.5 M sodium sulfate solution). The sample from the East Sea, China, was further tested to evaluate the EC performance of T3 in the presence of light. The hydrogen production rate is higher in real seawater than in simulated seawater (Fig. 21b) because cations such as $Na^+$, $Mg^{2+}$, $Ca^{2+}$, $K^+$, and $B^{3+}$ present in the former improve conductivity. The performance lasts over a long period without obvious decay compared to that promoted by nanosheets with S-vacancies (Fig. 21c). Compared to S-vacancies, the Re vacancies in the $ReS_2$ nanosheets adsorb $H^+$ ions more easily than they do the other five cationic ions. Hence, degeneration of active sites is avoided as manifested in the durability of the system (Fig. 21c, d). The study demonstrates that T@Td-$ReS_2$ nanosheets are practical and versatile photocatalysts in different environments.

Tang et al. [185] constructed an IR-driven PCSS system based on $WO_2$-$Na_xWO_3$ ($x > 0.25$) by reduction of semiconductor $Na_xWO_3$ ($x < 0.25$) nanowire bundles at high temperatures. During the calcination process, the nanowire bundles are reconstructed into micron-sized crystals. The residual reducing agents and carbon particles mostly exist either independently or on the surface of the micron-sized crystals. The seawater splitting activity of this system was demonstrated. In addition to the tungsten conductive oxides, other hybrid conductive oxides with the general formula of $MO_2$-$A_xMO_3$ (M = V, Mo, Ta, Re, Nb, Tc, Ru; A = Na, K, Sr) in the material have potentially similar photocatalytic properties.

Wang et al. [186] prepared (Ni-ZnO)@C core–shell and yolk-shell nanoparticles for photocatalytic $H_2$ production from seawater. The average particle diameters of the embedded photoactive species (Ni and ZnO) in the carbon-shell are in the range of 7–23 nm. The collision frequency between water and photoactive sites is also highly increased within the confined space in the nanoreactors. The photocatalytic splitting of seawater promoted by the nanoreactors has a 5.01 mmol/h gcat yield of $H_2$.

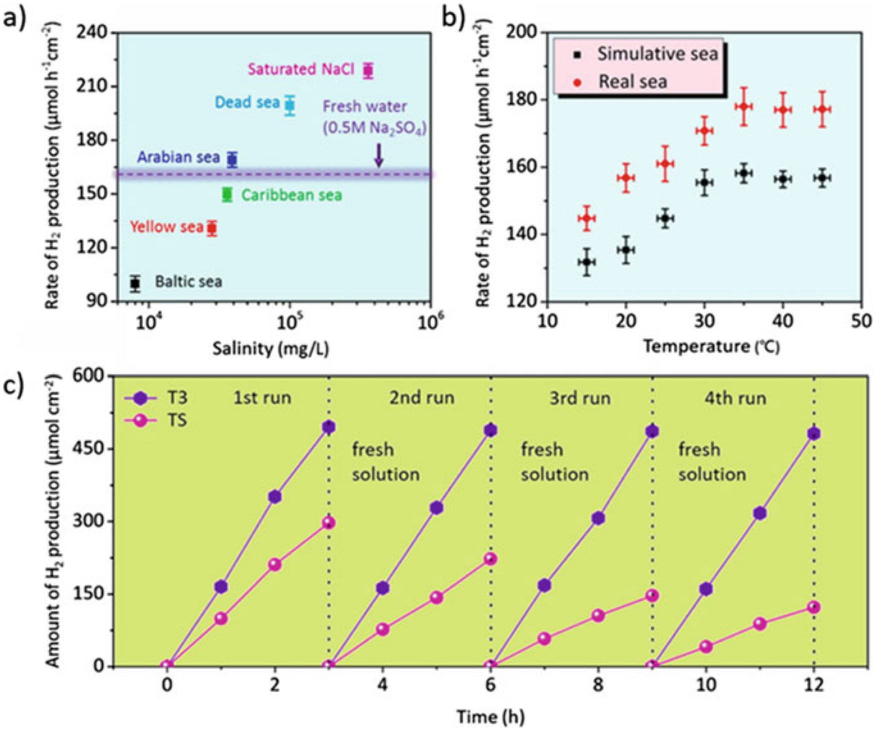

**Fig. 21** $H_2$ production rate in **a** different concentrations of seawater and **b** simulated and natural seawater at different temperatures. **c** Cycling test of $H_2$ production of T3 and TS in natural seawater

Mu-Hsiang Hsu et al. [187] have developed the Ce-doped ZnO/ZnS photocatalyst. The results of XPS Ce 3d spectra indicate that a mixed valence state ($Ce^{3+}$ and $Ce^{4+}$) is present in the photocatalysts. The activity for optimized Ce-doped ZnO/ZnS photocatalyst in an aqueous NaCl solution containing electron donors ($Na_2S$ and $Na_2SO_3$) (1200 μmol/g/h) is 5.2 times as high as that of undoped ZnO/ZnS photocatalyst. The improved activity using Ce doping originates from empty or half-filled Ce4f electron configurations which make the redox cycle between $Ce^{3+}$ and $Ce^{4+}$ rapid and repeatable. The recycled photocatalyst has only a limited activity loss, with the $H_2$ production rate for the fourth cycle being 85% of the first.

Kang et al. [31] report the results of studies of a CDs-CdS photocatalyst, comprised of cadmium sulfide (CdS) cocatalyst and carbon dots (CDs) as cocatalyst. A series of CDs/CdS composites were observed to be efficient hydrogen production photocatalysts in both water and seawater. Four typical morphologies of CDs/CdS composites have been successfully synthesized with different sulfur sources and solvents. As shown in Fig. 22a, CDs/CdS composites were rod-like CDs/CdS-R with a diameter from 50 to 60 nm, CDs/CdS-S nanosheets with thin layers (Fig. 22b), CDs/CdS nanospheres with uniform size (diameter around 60 nm) and distribution with vesicle-like structure (Fig. 22c), and irregular large bulk CDs/CdS-I composites not having a

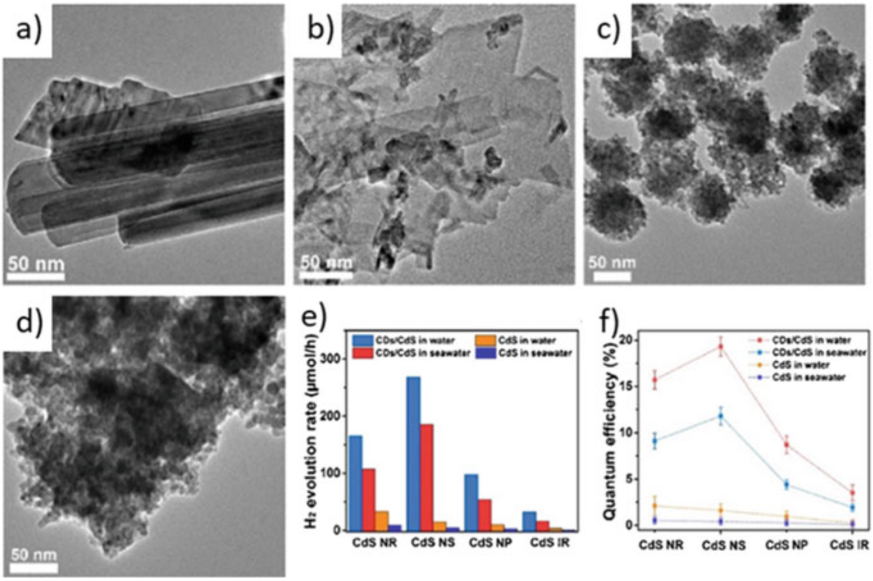

**Fig. 22** **a**–**d** TEM images of different samples. **e** Photocatalytic performance of different samples in water and seawater. **f** AQE tests for different samples

characteristic morphological structure (Fig. 22d). The introduction of CDs into CdS nanocrystals remarkably enhances photocatalytic activity. Figure 25e shows that the composite photocatalysts have photocatalytic activity in seawater, corresponding to 65%, 70%, 55%, and 50% of those in water, respectively. On the contrary, CdS not loaded with CDs exhibits low activity, which is even lower in seawater (30% of that in water). The AQY values under optimal conditions with irradiation at 420 nm are 15.7%, 19.3%, 8.7%, and 3.5% for CDs/CdS-R, CDs/CdS-S, CDs/CdS-N, and CDs/CdS-I, respectively. In contrast, a AQY value of 2.1% is obtained using CdS-R, which is lower that the lowest value for CDs/CdS-I. In seawater, CDs/CdS composites maintain about 50–60% of their AQYs in water with the highest value being 11.8% for CDs/CdS-S. Additionally, the highest AQY value in seawater for CdS is only 0.53% while the lowest is 0.07%.

# 4 Industrialization

## 4.1 Introduction

Global energy consumption has increased by about 1.7% annually over the past 10 years and reached 17.9 TW (terawatts) in 2017, a value that is estimated to increase to 22 TW by 2030. About 80% of the energy consumption relies on fossil fuels during the period of transition, and carbon dioxide emissions should also increase over the next several decades. In the early 1970s, Fujishima and Honda reported the results of a study of photochemical water oxidation on a $TiO_2$ photoanode. Although an electrical or chemical bias was necessary to drive the process, this phenomenon now known as the Honda-Fujishima effect laid the foundation for using semiconducting materials in the thermodynamically uphill water splitting reaction to convert light into chemical and storable energy. Photocatalytic hydrogen production is among a group of catalytic processes that could potentially address the above challenges, and it can contribute to the realization of sustainable societies. However, many obstacles exist in developing a practical and renewable solar-driven $H_2$ production technology. An economic analysis of solar $H_2$ production by the U.S. Department of Energy estimated that a photocatalytic system with an STH efficiency of 5% would produce $H_2$ at a cost of \$2.30 $kg^{-1}$. Recent progress shows that achieving the goal of attaining a 5% STH efficiency for photocatalytic $H_2$ production is not far off. The results obtained thus far suggest that the photocatalysis approach is a promising strategy for large-scale solar $H_2$ production because the reactor designed for this purpose is easily scaled up. However, a major issue still to be considered is the need to separate $H_2$ and $O_2$ from the explosive product gas mixture [188].

In this chapter, we introduce the economic cost and practical value of photocatalytic hydrogen industrialization and briefly summarize the design of large-scale synthesis and catalytic systems for photocatalysts and explore their cost competitiveness.

## *4.2 Economical Costs versus Practical Value*

The United States Department of Energy (US DOE) had estimated that the maximum cost of hydrogen in 2020 of US\$ 2–4 $kg^{-1}$ would make this gas an economically viable fuel [189]. The cost of photoelectrochemical hydrogen production was predicted to be US\$ 5.7 $kg^{-1}$ in 2020 and to decrease to US\$2.1 $kg^{-1}$ in the more distant future based on market competition. In 2013, Pinaud et al. conducted a techno-economic analysis of the cost of producing hydrogen using various photocatalytic and photoelectrochemical systems (Fig. 23) [190]. Based on assumptions of the STH values of 10% and 5% and a common lifetime of five years, the analysis estimated that the cost would be US\$1.6 and US\$3.2 $kg^{-1}$ for respective single and dual bed particle suspension systems. Using assumed STH values of 10% and 15% and a lifetime of 10 years, hydrogen generated using photoelectrochemical systems with fixed planar and tracking concentrator arrays was predicted to cost US\$10.4 and US\$4.0 $kg^{-1}$, respectively. Because suspended photocatalyst systems containing simple plastic bag reactors are expected to have lower capital costs than photoelectrochemical systems, the cost of their implementation could meet the target hydrogen price of US\$2–4 $kg^{-1}$ suggested by the US DOE. If significant improvements are made in STH efficiencies and cell lifetimes, it might be possible to utilize additional energy and material inputs and still maintain costs in the target region.

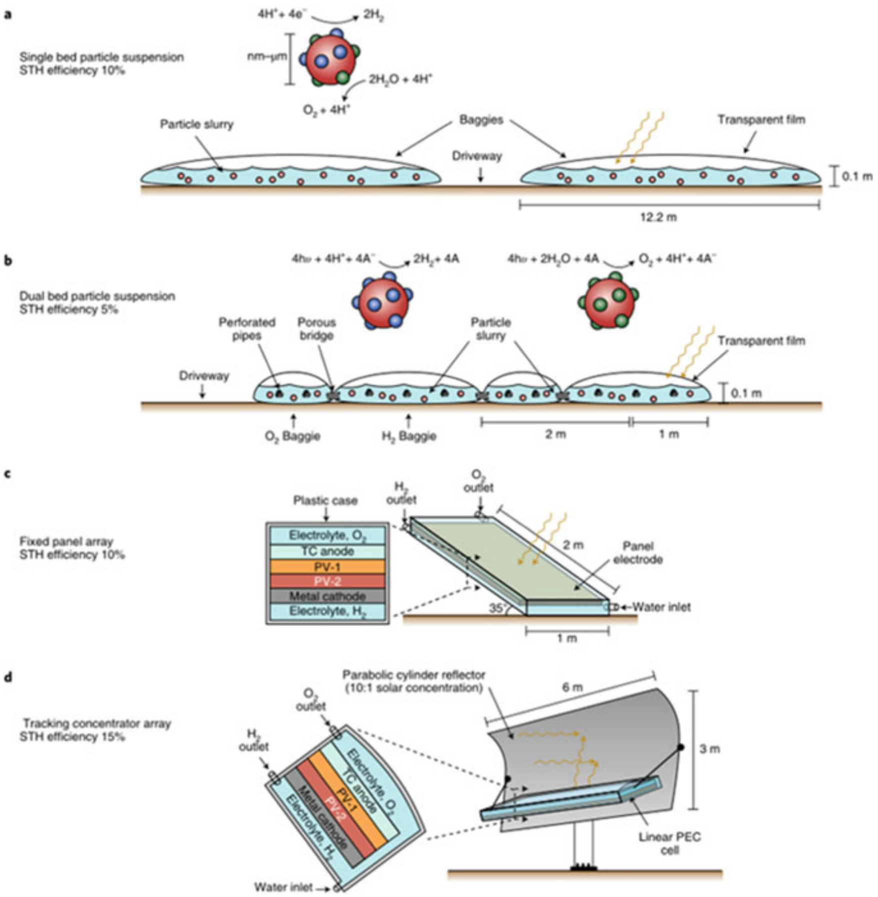

**Fig. 23** Four different types of reactors. **a** Single bed type, **b** dual bed type, **c** fixed panel array type, and **d** tracking concentrator array type

In earlier evaluations, the cost of solar hydrogen production was estimated by assessing the capital and operating costs of the systems [190]. However, the allowable cost can also be estimated using the resulting hydrogen and oxygen products as metrics [191]. Fig. 24 gives an overview of a blueprint of photocatalytic $H_2$ production plant with an area of 100 m * 100 m. In this setup, 228 kg of hydrogen is produced and 2 tons of water is consumed daily. Assuming an STH efficiency of 10%, daily AM1.5 G irradiation for 7.6 h (corresponding to 317 W $m^{-2}$), a lifetime of 10 years, and an annual depreciation rate of 4%. Using this approach, the cost of the system was calculated to be US\$136 $m^{-2}$, and the respective prices of $H_2$ and $O_2$ would be US\$3.5 $kg^{-1}$ and US\$0.1 $kg^{-1}$. However, solar irradiance is typically 240 W $m^{-2}$ at most, [190]. So the accurate cost would be US\$102 $m^{-2}$. It is estimated that the balance of system expenses alone will exceed the target [192]. Thus, a significant

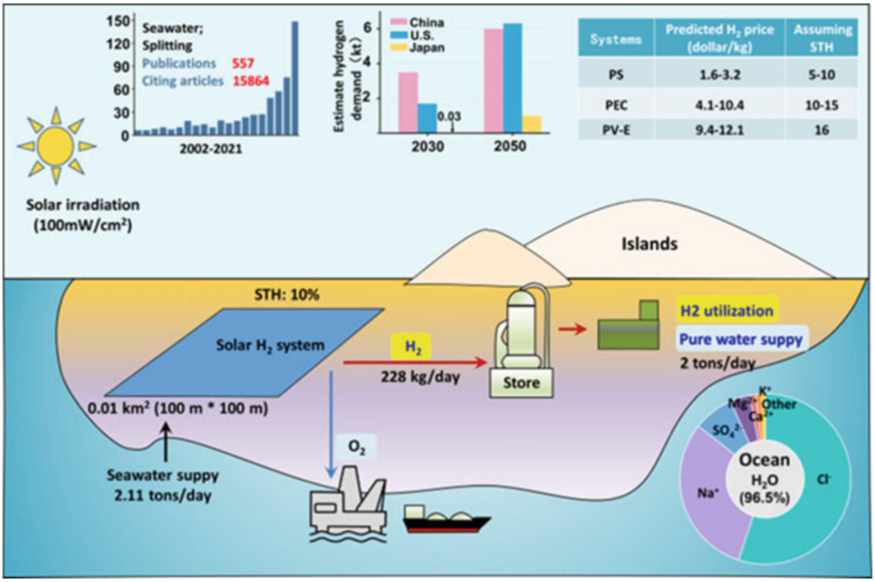

| Systems | Predicted $H_2$ price (dollar/kg) | Assuming STH |
|---|---|---|
| PS | 1.6-3.2 | 5-10 |
| PEC | 4.1-10.4 | 10-15 |
| PV-E | 9.4-12.1 | 16 |

**Fig. 24** A proposed scheme for large-scale $H_2$ production via solar seawater splitting

need exists for developing new materials and techniques for photocatalytic systems for hydrogen generation.

Before solar hydrogen take the place of fossil fuels, many hurdles facing solar photochemical water splitting must be overcome. To make solar hydrogen a feasible fuel, the design principle of photocatalytic systems must be coupled with uncovering low-cost, stable, and efficient materials. Specifically, the ultimate goal is to reach >10% efficiency, >10 years of stability, and a hydrogen cost that is competitive on an energy equivalent basis with those of fossil fuels.

In 2020, Domen et al. [193] reported the development of a 100-$m^2$ scale prototype solar hydrogen production system consisting of an array of 1,600 reactor units composed of mass-produced $SrTiO_3$:Al as the photocatalyst and loaded with Rh, Cr, and Co as cocatalysts. The photocatalyst was fabricated as individual units with the light receiving areas of 625 $cm^2$, and gaps between the ultraviolet-transparent glass windows and photocatalyst sheets adjusted to 0.1 mm (Fig. 25a, b) to minimize the water load and prevent accumulation and ignition of the product gases. A 100-$m^2$ water splitting photocatalyst panel array, consisting of $33\frac{1}{3}$ modules of 3 $m^2$ each, is shown in Fig. 28c. The entire hydrogen production system operated under field conditions for more than a year reached a maximum STH of 0.76% under natural sunlight.

It should be noted that economically large-scale $H_2$ production by water splitting, let alone seawater splitting, using photocatalysis is still a challenge. Observations made by Domen and colleagues should inspire and encourage other researchers.

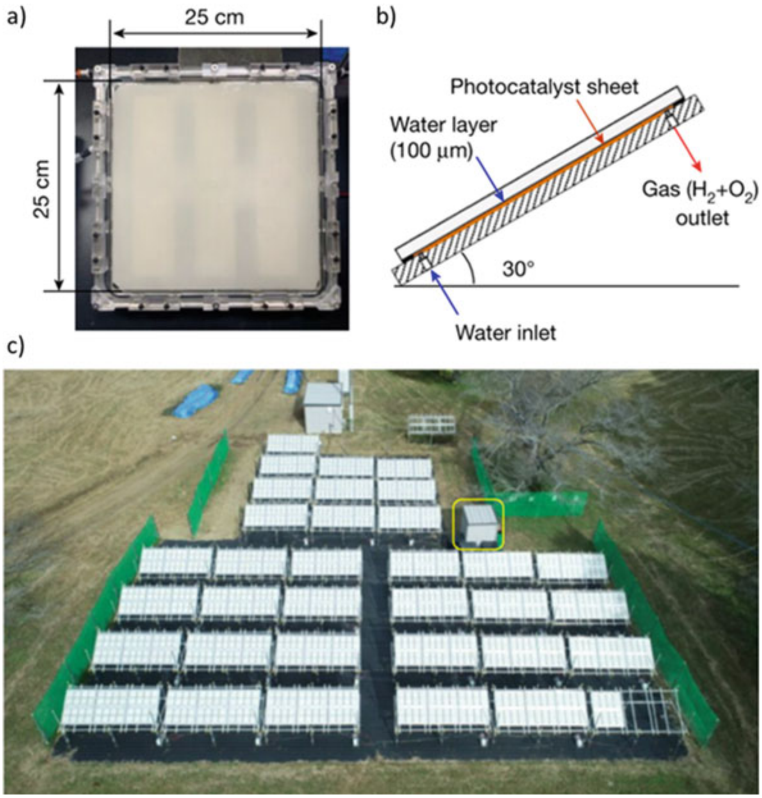

**Fig. 25** A 100-m$^2$ solar panel reactor for $H_2$ production. **a** A picture of a panel photoreactor unit. **b** Side view of the panel reactor unit. **c** An 100-m$^2$ solar hydrogen production system

Their results indicate the timescale needed for developing a successful system for the production of hydrogen.

## *4.3 Large-Scale Synthesis of Photocatalysts*

### 4.3.1 Large-Scale Batch Synthesis

To date, batch-wise wet chemical processing has remained the dominant method for laboratory synthesis of photocatalysts. This approach requires minimal investment in equipment and is supported by extensive knowledge available in the literature. The self-contained apparatus also contained components for reagent storage, product separation, and waste gas treatment (Fig. 26). Importantly, the produced nanocrystals are separated using ultrafiltration, which requires a lower energy input than centrifugation. The catalyst generated in this manner has an energy conversion efficiency of up to 4.3% and an AQY of 40.5% at 425 nm, which is nearly equal to the activity of a similar catalyst synthesized in a 130-fold smaller batch. However, the particle size distribution and catalytic activity are noticeably worse than those obtained using a twofold diluted, laboratory-scale synthesis system that does not require stirring [194]. This observation highlights the difficulty associated with the scale-up of process employed for nanomaterials synthesis using batch-wise wet chemical systems.

Besides increasing the batch size, improving the throughput of batch-wise synthesis is an alternative route, for example, shortening the processing time or increasing the reaction temperature. Completion of reactions, required to obtain reasonable yields, can be achieved by using more efficient heating methods such as microwave heating. For example, $\alpha$-$Fe_2O_3$ particles with an average size of 200 nm have been fabricated in a 5 L microwave-heated hydrothermal reactor, and the production rate is claimed to be comparable to 2.1 $m^3$ conventional reactors [195]. Many photocatalysts have been prepared by using similar methods where the required reaction time, typically a few minutes to hours, is an order of magnitude lower than those utilizing conventional hydrothermal methods [196]. However, the photocatalysts that are synthesized using microwave-assisted methods have not yet exceeded the gram scale in laboratory research, mainly because of the limited penetration of 2.45 GHz microwaves [197].

Lasers and direct currents have also been used for efficient heat delivery. In the former method, optical energy is converted to heat that melts/vaporizes a starting

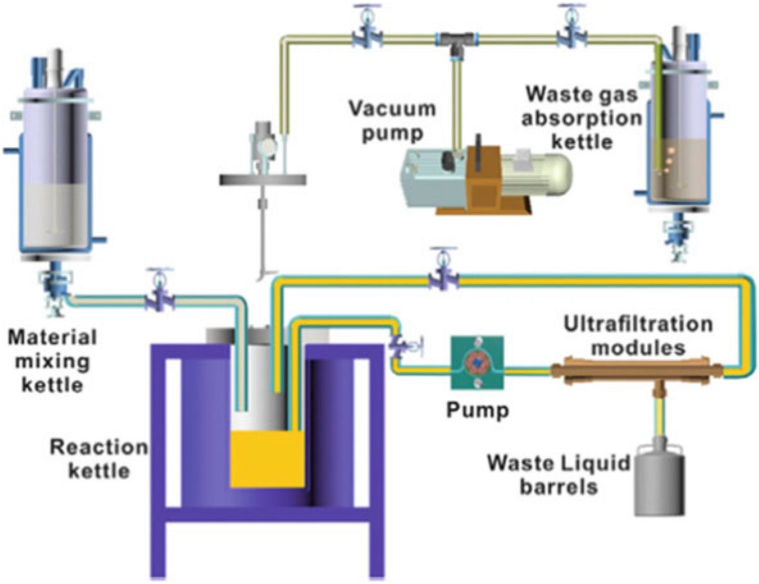

**Fig. 26** Schematic diagram of a pilot plant in large-scale batch hydrothermal synthesis mode

material, which is then transferred to the reaction medium [198]. Similar to lasers, high voltages applied to solid–liquid interfaces generate localized heating through plasma discharge. This method has been employed in the one-step synthesis of $TiO_2$-$x$ [199, 200], which is promoted by applying high voltage pulses to Ti electrodes immersed in $NH_4NO_3$ or $HNO_3$ electrolyte. It was suggested that metallic Ti melted/vaporized by the plasma at the cathode transfers heat to the electrolyte while being partially oxidized. In both of these heating methods, the amount of materials converted to heat by each laser/electrical pulse is microscopic, but production of the extreme temperatures occurs within 1 ms. As most of the input energy is delivered to the solid–liquid interface instead of the bulk mixture, these methods are energy-efficient and, hence, they have the potential for scale-up provided that low-cost processes exist for economic processes for product recovery.

Solid-state synthesis uses much higher precursor concentrations and hence it makes more efficient use of reactor volumes than wet chemistry. Due to sluggish diffusion and interaction between solid precursors, which necessitates the use of high temperatures for acceptable reaction rates, these processes are slow, energy-intensive, and accompanied by severe sintering. The high temperatures facilitate the removal of structural defects from the semiconductor crystals and improve carrier diffusion lengths. The negative effects of small surface areas can be compensated for by an increase in the number of charge carriers reaching catalytic sites. Furthermore, this method, which is applicable for industrial-level production, has a close to 100% yield based on the metal. Despite the fact that throughputs employed in research laboratories are limited to several grams, solid-state synthesis has great potential for use in the production of photocatalysts on large scales.

Similar to using wet chemical methods, solid-state synthesis of photocatalysts has also taken advantage of microwave heating. However, heating efficiency depends on the properties of the materials being processed, and it is modulated by the copious amount of solvent present in wet chemical but not solid-state synthesis systems. Microwave heating in solid-state mixtures is therefore non-uniform due to inhomogeneity. The strong microwave absorber CuO has been used as a medium to deliver heat to a reaction mixture. Although the uniformity of heating is affected, the reaction time is reduced to 18 min from the 3–4 h required using conventional heating. The product generated in this manner has a 50% improved PCWS activity compared with that using g-$C_3N_4$ synthesized in a furnace, because it has higher crystallinity.

A solid phase reaction can not only be accelerated using efficient heating but also by a flux which forms a melt that acts like a solvent to promote local diffusion of reactants. Recently, this method has been improved by increasing the amount of flux so that a significant fraction if not all of the precursors are in the solution phase during the reaction [201]. The resulting molten salt process enables the controllable formation of nanocrystals because crystal nucleation and growth occur more uniformly than in conventional solid-state synthesis systems. In this sense, this process parallels wet chemical synthesis with the exception of having significantly higher reactant concentrations. For example, Sr-doped $NaTaO_3$ nanocubes with sizes of 20–60 nm have been synthesized in molten NaCl–KCl and the material generated has remarkable overall water splitting activity under UV radiation [202].

### 4.3.2 Large-Scale Continuous Synthesis

Batch-wise synthesis requires that reactors be evacuated and recharged which leads to long down-times and batch-to-batch variations caused by non-linear heat/mass transport, particularly when using wet chemical processes. As a result, the use of continuous processes is preferred for industrial-level production. Considerable studies have been conducted since the 1990s on continuous hydrothermal flow synthesis (CHFS) of inorganic nanomaterials [203]. In contrast to laboratory-scale batch synthesis where the reaction mixture is usually heated for several hours at temperatures up to 200 °C, industrial-level production usually utilizes temperatures of 200–400 °C, thus, reducing the required residence time to a few seconds or minutes. In order to achieve these high temperatures in an even smaller timescale before the product formation starts, precursor solutions are often heated by direct mixing with supercritical water. Using this approach, small sizes of metal oxide, hydroxide, sulfide, and phosphate nanoparticles (less than 100 nm) have achieved a kg $h^{-1}$ scale. Figure 27 contains a schematic diagram of a representative CHFS system.

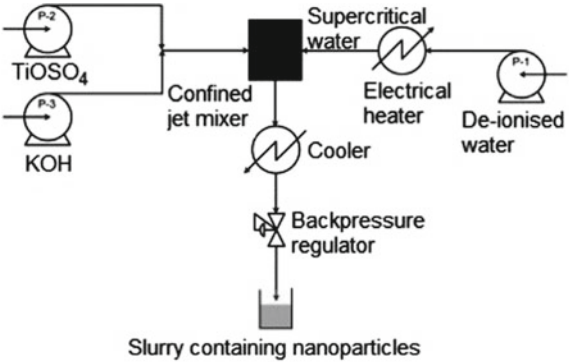

**Fig. 27** Schematic diagram of a CHFS system

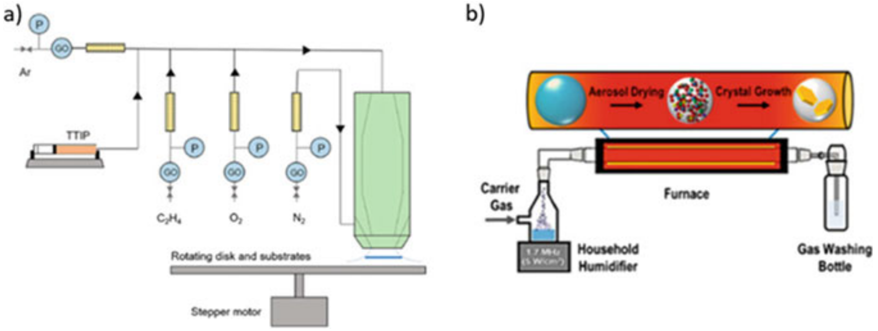

**Fig. 28** **a** Schematic diagram of vapor-fed flat flame aerosol synthesis. **b** Schematic diagram of a ultrasonic spray pyrolysis process

While many photocatalytically active materials including $TiO_2$, α-$Fe_2O_3$, CdS, ZnO, and $WO_3$ have been prepared by this method, [204] research works on their PCWS activity have been extensively reported. Makwana et al. synthesized anatase $TiO_2$ with $TiOSO_4$ and KOH, and the fabricated sample has tunable sizes of 5–18 nm and displayed high PCWS activity. More recently, a 5 nm $Ti^{3+}$-doped $TiO_2$/C composite was synthesized on a small scale using 45 mmol $h^{-1}$ throughput of the Ti precursor [205]. The composite has a higher hydrogen evolution activity than that of commercial $TiO_2$. In an earlier study, a similar activity was achieved by employing $K_2Ti_6O_{13}$ nanofibers. This material was synthesized using a residence time of $\sim$2 s and a production rate of 0.3 g $h^{-1}$. Notably, the throughput of CHFS still has a bottleneck associated with time-consuming product separation.

Although not used often in chemistry, gas-phase synthesis is by far the most useful method for industrial production. For example, carbon black, fumed silica, and the commercial P25 et al. are fabricated using a type of gas-phase process called flame aerosol synthesis (FAS), which was first commercialized in the 1940s. In FAS, precursors and supporting fuels in the forms of either vapors or atomized liquids are introduced continuously into a flame, where they undergo pyrolysis to form nanoparticles along with exhaust gases which can be recovered by using cyclone separators or filters.

Wu et al. [206] reported that a methanol solution of a FAS-derived 10–20 nm $TiO_2$ photocatalyst promotes photocatalytic $H_2$ evolution with a AQY of 39.4% at 360 nm. $TiO_2$ was synthesized by feeding vaporized titanium(IV) tetraisopropoxide along with ethylene, oxygen, and argon into a flat flame on the surface of a rotating collection disk (Fig. 28a). Fast quenching of metastable intermediates before rutile crystallization leads a $TiO_2$ II phase during this process [207]. A flame is not the only heat source that can be used for the gas-phase synthesis of nanomaterials. As depicted in Fig. 28b, the so-called ultrasonic spray pyrolysis process, in which a conventional tube furnace is used to continuously dry and pyrolyze fine droplets of precursor solution without combustion, can also be employed for this purpose. Compared with FAS, ultrasonic spray pyrolysis does not involve rapid heating of precursors, which causes incomplete vaporization of droplets before a significant amount of product forms. The resulting particles in the form of polycrystalline aggregates retain the shape of the precursor droplets. It has been noted that despite the large potential of using gas-phase nanomaterial synthesis at commercial levels, short residence times of particles prevent the healing of structural defects which compromises photocatalytic activity [208]. Thus, to achieve desirable results, this approach could be used in combination with an annealing or wet chemical step. In addition, how species adsorbed on nanoparticles affect morphological control during FAS is poorly understood.

## *4.4 System Design*

### 4.4.1 Reactors Design

Conventionally, laboratory-scale PCWS use suspensions of particulate photocatalysts in flask-type reactors. However, the difficulty in the scale-up of suspension systems might be reflected in the absence of large-scale demonstrations with appreciable STH values. This approach has difficulties on large scales for several reasons. Firstly, considering the larger volumes of water required, minimizing of reactor costs is still challenging. For example, a 1 cm depth of water in a reactor has a mass that reaches 10 kg $m^{-2}$. Thus, large-scale use of these types of reactors is not feasible considering that the target cost for the entire system needs to be US$102 $m^{-2}$ [209]. Secondly, sedimentation of particulate photocatalysts in the reactor leads to an insufficient irradiation unless stirring is used. Tubular reactors coupled with compound parabolic concentrators (CPC) have been examined for large-scale outdoor operation of PCWS reactions using sacrificial reagents. [210] No daily light tracking is required when CPCs are utilized. In a system developed by Jing et al., the CPC has a maximum half incident angle of 14°, aperture length of 0.4 m, and total length of 1.5 m, along with 1.6 m long Pyrex glass reactor tubes. This configuration has a concentration factor of four. Thirdly, recovering suspended catalytic powder using filtration or centrifugation is energy- and time-consuming. Processes associated with spent photocatalyst replacement would be simpler considering the large footprints of PCWS systems. Because fixed particulate photocatalysts address these problems, it has been suggested that photocatalysts should be generated as planar panel modules such as those used in photovoltaic systems.

Water splitting systems using photocatalyst powders thinly fixed on substrates have been described in several recent publications [211, 212]. It is possible to fix particulate photocatalysts onto substrates by using drop-cast methods along with silica binders. Controlling the hydrophilicity and porosity of these layers is important to preserve the intrinsic activities of particulate photocatalysts fixed to substrates. For example, photocatalyst particles fixed on glass substrates exhibit lower activities than suspensions of the same materials [137, 211]. This activity retardation is caused by the inefficiency of penetration of water and desorption of gaseous products from the dense particulate photocatalyst layer. Hydrophilic silica particles accelerate water splitting promoted by photocatalyst panels because they create voids in the particles and, thus, promote the diffusion of substances in solutions and product gas bubbles. The properties of Z-scheme-type sheets of OER and HER photocatalysts fixed on conductive materials have been reviewed recently [213–215]. The size of the photocatalyst sheet can be scaled up without special consideration being given to electron and mass transfer between the OER and HER photocatalysts.

In 2015, Schröder et al. [212] described a 0.76 $m^2$ flat panel-type reactor employing a $C_3N_4$ photocatalyst and triethanolamine as a sacrificial electron donor. The reactor contained a reactor body composed of an etched Teflon plate (6 mm in depth), exchangeable stainless-steel plates coated with the photocatalyst using a

Nafion binder, a plexiglass window (8 mm in thickness), a reaction solution reservoir (10 vol% aqueous triethanolamine), and a pump for circulation (Fig. 29). The photocatalytic $H_2$ production rate has decreased by 40% after continuous operation over 30 d. Unfortunately, the STH efficiency of this device was not correctly calculated due to the participation of the sacrificial reagent. In fact, a majority of the energy stored as hydrogen in this system originates from the chemical energy of the sacrificial reagent and not from the solar energy harvested by photocatalysis.

K. Domen et al. [137] has reported panel-type reactors intended for large-scale via highly active $SrTiO_3$:Al photocatalyst sheets. $SrTiO_3$:Al has an absorption edge of 390 nm and a wide band gap of 3.2 eV. In a scaled-up system, $SrTiO_3$:Al materials were fabricated by depositing the $SrTiO_3$:Al photocatalyst on frosted glass plates. The plates were immersed in a laboratory-scale panel-type reactor filled with water. Under UV light illumination over the entire plate, the rate of hydrogen and oxygen evolution was tested to reach 5.6 mL $cm^{-2}$ $h^{-1}$. During the process, small bubbles of hydrogen and oxygen migrate upward due to the buoyant force without forced convection. The STH of the water splitting reaction reaches 10%, while producing a mixture of hydrogen and oxygen at a rate of 5.6 mL $cm^{-2}$ $h^{-1}$. In addition, they constructed 1 $m^2$ panel reactors by using plexiglass plates for the body and window, and 8 g $m^{-2}$ $SrTiO_3$:Al sheets and distilled water were loaded into the device (Fig. 30). The STH efficiency of this reactor for non-sacrificial solar-driven water splitting under natural

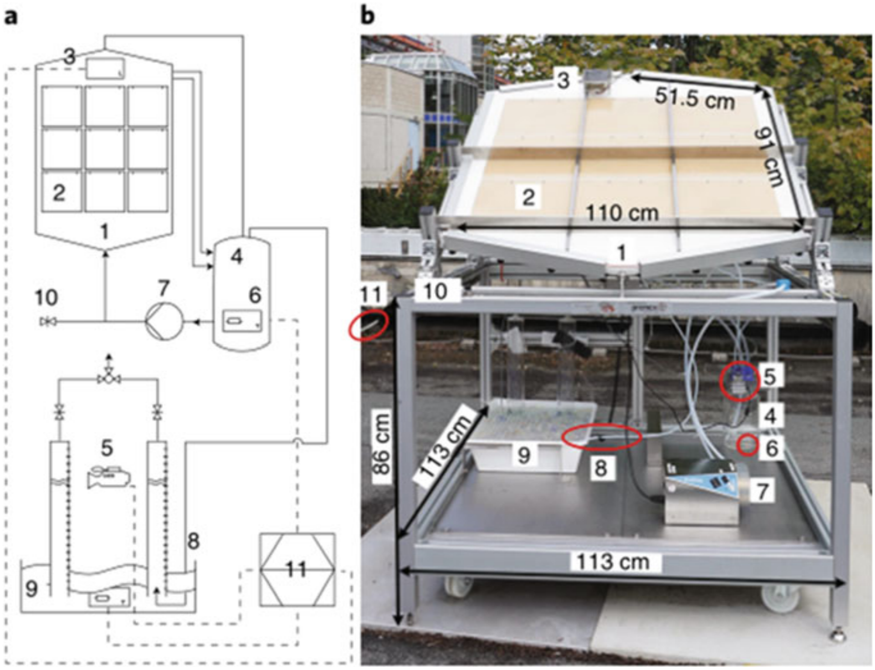

**Fig. 29** **a** Schematic diagram and **b** photograph of large-scale photoreactor

sunlight was estimated to be 0.4%. This value is very close to that obtained during laboratory-scale experiments. The results suggest that a panel-type reactor with an area greater than 1 $m^2$ could obtain STH of 10% under AM1.5 G irradiation without using forced convection.

One of the critical issues that needs to be considered in creating scaled-up or overall water splitting reactors is the fire/explosion hazard arising from the fact that $H_2$ and $O_2$ are generated simultaneously. The produced $H_2$ could be diluted with an inert gas, for example, $N_2$ or $CO_2$, so that its concentration is below the lower flammability limit before being separated by selective permeable membranes [216, 217]. However, considering that hydrogen's lower flammability limit is only 4% (in air/oxygen, at normal temperatures and pressures). However, the large amount of diluent required limits the process.

A shallow funnel-shaped photoreactor without active stirring has a similar STH as that of an ordinary stirred tank photoreactor [218]. In Fig. 31 a, b is shown the reactor in which a slurry is introduced tangentially to induce mixing. Notably, a 44% improvement in AQY was obtained in a more recent study using $Pt/TiO_2$ catalyst beads in a fluidized bed reactor rather than a recirculating suspension of $Pt/TiO_2$ nanoparticles [219]. The system also included a sparger downstream of the reactor to extract $H_2$ and $O_2$ with an inert gas (Fig. 31c). Efficient mass transfer and fast removal of product gasses are proven to be key factors leading to high AQY because they suppress reverse reactions via a computational modeling [220].

Low-pressure operation on large scales is a burden unless the sacrificial reagent is waste or can be simply regenerated. Specifically, the production of hydrogen as a

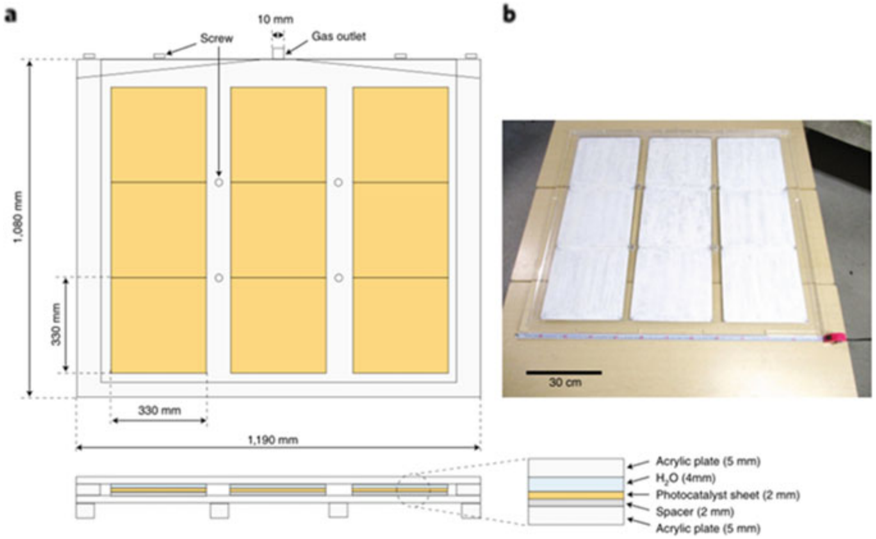

**Fig. 30** **a** Schematis of a 1 × 1 m panel-type reactor containing photocatalyst coating sheets and **b** a photograph of a 1 × 1 m panel containing $SrTiO_3$:Al photocatalyst

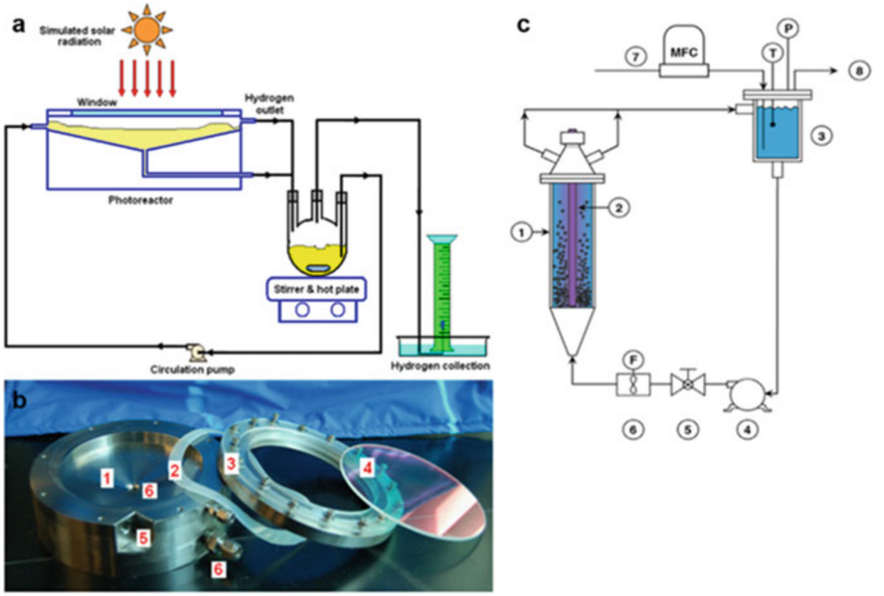

**Fig. 31** **a** Schematic diagram of flow photoreactor and **b** a photograph of laboratory-scale flow photoreactor. **c** Schematic diagram of a fluidized bed photoreactor system

basic feedstock at the expense of using downstream chemicals cannot be justified. With this in mind, a hybrid photocatalytic-solar thermal cycle has been devised [221] in which photocatalytic hydrogen production occurs together with the oxidation of aqueous $(NH_4)_2SO_3$ to form $(NH_4)_2SO_4$ by photogenerated holes, which then passes through a metal oxide-assisted multistep solar thermal process to regenerate a more recent study and produce oxygen.

### 4.4.2 Optical Design

The design of a photoreactor needs to consider the maximum exposure of catalyst particles to solar radiation. The simplest way is comprised of a flat panel-type container (Fig. 32a), which has been proven to be a cost-effective approach to water treatment [222]. However, for water splitting the reactor needs to be sealed with a highly UV transparent cover, which leads to capital cost increases. In typical laboratory studies, quartz glass is employed as the cover. However, the use of this type of glass in large reactors is too costly. While thin borosilicate and soda lime glass have satisfactory transparencies in the UV region, when they are utilized to cover large areas, their thicknesses need to be large to support their weights, which leads to UV transmission decreases. Polymethyl acrylate is commended for use as alternative [218], but its reliability under constant exposure to direct sunlight is questionable.

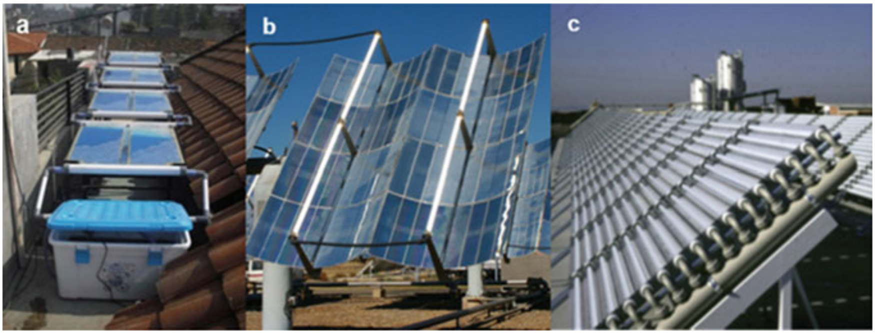

**Fig. 32** **a** Flat panel-type photoreactors. **b** Tubular photoreactors with parabolic trough collectors and **c** tubular photoreactors with compound parabolic collectors

Based on the above reasons, tubular glass reactors have become the compromise between transparency and mechanical strength. Moreover, flat panel reactors were employed in recent pilot-scale trials of PCWS as elaborated further in Progress in pilot tests due to its low cost and ease of reactor construction on such scales [211].

To fully utilize the surface area of a tubular reactor, light reflectors have been employed to enable illumination of the underside of the reactor. Originating from solar thermal engineering studies, the old-type reflectors have single parabolic profiles. This configuration, known as a parabolic trough (Fig. 32b), only reflects incident light that is perpendicular to the aperture of the reactor tube at the focal point. Thus, all the diffuse light is not utilized [223]. Compound parabolic collectors (CPCs, Fig. 33a) are now the most of the reflectors used for water splitting devices, which allow some diffuse light to reach the reactor tube (Fig. 32c). Furthermore, a new type of reflector geometry has been developed recently for the improvement of the uniformity of illumination on the tube surface (Fig. 33b) [224].

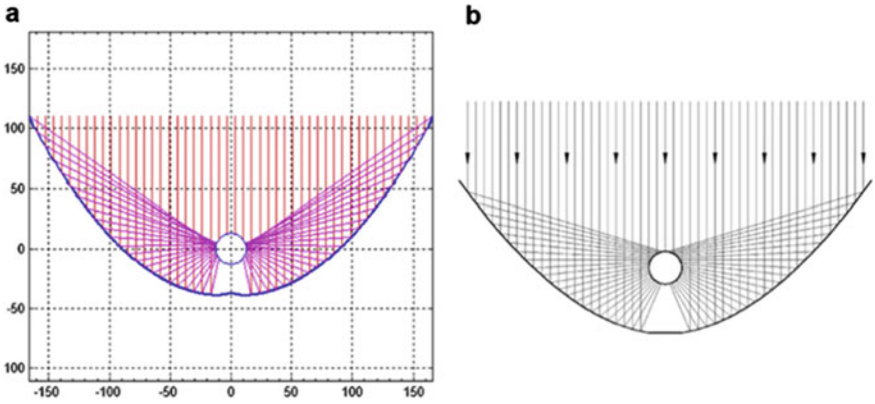

**Fig. 33** Schematic diagram of **a** typical parabolic collector and **b** surface illumination uniform collector

### 4.5 Technology Cost Competitiveness

Unlike in fundamental research where gaining insight into processes that occur is the most important goal, applied technologies depend on profitability. Most of the solar $H_2$ production technologies discussed in this chapter are at the research stage only. Economic assessments of these approaches are made difficult by the unavailability of key data, which necessitates that coarse assumptions be made. As a consequence, direct comparison between different systems provides little insight into the relative viabilities of hydrogen-generating devices. Nevertheless, rough comparisons can provide perspectives for designing future investigations.

Considering that photovoltaics and water electrolysis are well-established industrial processes, modular PEC water splitting has received the greatest techno-economic study thus far. As shown in Table 1, the levelized cost of hydrogen (LCH), estimated by different authors, varies from 4.7 to over 13 USD $kg^{-1}$. An important assumption that leads to differences in the estimates is the capacity factor of the electrolyzer unit, i.e., the ratio of the average actual production rate to the design capacity. This factor directly influences the size and hence capital cost of the electrolyzer. To obtain the lowest LCH, an assumption is made that the electrolyzer operates at constant full capacity, which is equal to that designed for hydrogen production [225]. For a model that includes a minimal size electrolysis plant, the capital cost would be less than 15% of the LCH in the case of a PEM electrolyzer, a value similar to that for a grid-powered electrolyzer [226]. One way of estimating the size of an electrolyzer at the upper end of LCHs is to make its capacity equal to the peak power of the photovoltaic plant, in other words to assume that all photovoltaic power is utilized by the electrolyzer [192, 227]. This consideration significantly increases the contribution of the electrolyzer cost to LCH which can be up to 40%. In this design, the electrolyzer capacity is severely underused.

It has been proposed that grid electricity be used as supplemental to photovoltaic power to keep the electrolyzer operating at full capacity [192]. Because at the current time contributions to the grid are dominated by nonrenewable energy sources, a design of this type would have a high carbon footprint, along with estimated LCHs being higher than that of grid-powered electrolysis (6.6 versus 5.9 USD $kg^{-1}$).

Remarkably low LCHs of 2.1 and 4.2 USD $kg^{-1}$ have been estimated for single semiconductor and Z-scheme PCWS systems, respectively. Both values are within the U. S. Department of Energy target and, thus, they are potentially competitive with hydrogen generation by methane steam reforming having an estimated cost of approximately 1.4 USD $kg^{-1}$ [156, 192]. However, this is an optimistic outlook rather than an estimation based on the current state-of-the-art technologies.

**Table 1** Various solar hydrogen production technologies and their economic assessment

| Type | Scale | STH or $H_2$ productivity | LCH(USD $kg^{-1}$) |
|---|---|---|---|
| Reforming | – | – | 1.4 |
| Photocatalytic, single semiconductor | $10td^{-1}$ | 10% | 2.1 |
| Oxygenic biophotolysis | $10td^{-1}$ | 9.2% | 3.9 |
| Photocatalytic, Z-scheme | $10td^{-1}$ | 5% | 4.2 |
| Photovoltaic PEM electrolysis | $1td^{-1}$ | 10.8% | 4.7 |
| Integrated PEC, 10× solar concentration, and tracking | $10td^{-1}$ | 15% | 5.3 |
| Anoxic biophotolysis | $10td^{-1}$ | 5.2% | 5.5 |
| Integrated photovoltaic-concentrated solar thermal SOSE | $8MW_{PV}$ | – | 5.7 |
| Grid-assisted photovoltaic PEM electrolysis | $10td^{-1}$ | 9.8% | 6.6 |
| Integrated photovoltaic-concentrated solar thermal SOSE | $0.4td^{-1}$ | 9.9% | 6.6 |
| Solar thermal hybrid $H_2SO_4$ | $50MW_{th}$ $10.2td^{-1}$ | – | 6.9 |
| Anoxic biophotolysis by immobilized green algae | $10td^{-1}$ | 2.25% | 7.9 |
| Photovoltaic SOSE | $0.4td^{-1}$ | 6.3% | 8.4 |
| Solar thermal $NiFe_2O_4$ | $50MW_{th}$ $11.4td^{-1}$ | – | 8.6 |
| Integrated PEC, 10× solar concentration, and tracking | $10td^{-1}$ | 20% | 10.0 |
| Photovoltaic electrolysis | – | 11.5% | 10.0 |
| Photovoltaic electrolysis, 10× solar concentration | – | – | 10.1 |
| Integrated PEC, fixed panel | $10td^{-1}$ | 9.8% | 12.3 |
| Photovoltaic SOSE | – | – | 12.8 |
| Photovoltaic PEM electrolysis | $10td^{-1}$ | 9.8% | 13.1 |
| Integrated PEC, fixed panel | $10td^{-1}$ | 10% | 13.6 |
| Photo-fermentation | $10td^{-1}$ | 3.5% (1.5%) | 13.6 (18.3) |
| Solar thermal $CeO_2$ | $90MW_{th}$ | 13.4% | 14.7 |
| Integrated dark/photo-fermentation | $1.3td^{-1}$ | 0.33 $mmolL^{-1}$ $h^{-1}$ | 25.1 |
| Integrated dark/photo-fermentation | $1.4td^{-1}$ | 0.5 $mmolL^{-1}$ $h^{-1}$ | 37.5 |
| Solar thermal $NiFe_2O_4$ | $90MW_{th}$ | 6.4% | 43.8 |

(continued)

**Table 1** (continued)

| Type | Scale | STH or $H_2$ productivity | LCH(USD $kg^{-1}$) |
|---|---|---|---|
| Integrated dark/photo-fermentation | $27.1 t d^{-1}$ | $0.21 mmol L^{-1} h^{-1}$ | 62.6 |

## 5 Perspectives

PCWS has attracted wide interest for the past 50 years and achieved significant improvements reaching solar-to-hydrogen conversion efficiencies $\eta_{STH}$ of nearly 2% during the last 10 years. Thus, efficiency is one of the many considerations guiding the selection of a solar hydrogen production technology. This technology used in seawater splitting has attracted attention in only the recent 5 years. Among the recent studies on PCSS, $TiO_2$ is the most widely used semiconductor material, and the stability of the photocatalyst plays a significant role. However, only part of the reported efforts give an evaluation of the stability of the photocatalyst. Different kinds of inorganic salts (NaCl, $MgCl_2$, etc.), organic matter, and microorganisms exist in seawater. As a result, the activities and durabilities of photocatalysts can be lower when used in seawater rather than pure water. For estimating the effects of ions, it is generally believed that $Na^+$ has a positive effect on photocatalytic water splitting, but the influence of $Cl^-$ remains controversial. Nevertheless, it should be noted that the effects strongly depend on the photocatalysts used.

Although there have been a few reports on the use of electrocatalysis and photoelectrocatalysis for water splitting, photocatalysis has advantages over these approaches that include (1) the design of the photocatalytic device is cheap and easy maintenance, and (2) the reaction does not require additional electrolytes, reducing costs of product separation. Thus, the development of highly efficient PCSS systems for $H_2$ production is highly desirable.

Compared with PCWS, the development of the PCSS has three significant advantages. Firstly, it not only makes full use of abundant seawater resources, opening up scenes and solving the problem of lack of freshwater, but it also greatly reduces the cost and avoids the desalination process, which is more in line with actual application requirements. Secondly, the inorganic salts and other impurities may improve the efficiency of PCWS in some systems. Finally, other high-value-added by-products such as $ClO^-$ can be produced.

Several questions should be posed at the outset of studies of photocatalytic seawater splitting. One concerns possible approaches that can be taken to decrease structural defects, lower surface reaction barriers, and control particle morphology in order to utilize as many photoexcited carriers as possible in narrow band gap photocatalysts. Next, how can backward reactions be suppressed while separating the $H_2$ and $O_2$ products in overall water splitting systems? Also, how can water splitting devices be scaled up for practical applications without significant decreases in performance? Minimization of the negative effects of electron mediators used in PCSS needs to be considered. Finally, the question of how visible light-responses photocatalysts can be stabilized and verified during the water splitting process needs to be addressed.

## 6 Conclusion

In this chapter, we highlighted recent progress made in studies of PCWS, with the goal of inspiring future efforts in this important field. The development and utilization of sustainable and clean solar energy is the goal of investigations aimed at solving the intertwined energy and environmental dilemma.

Firstly, a brief introduction was given to describe the conceptual basis of PCSS and PCWS, including evaluation parameters such as IQY, AQY, STH, and TON, and the effects of salt, sacrificial agents, cocatalysts, and light sources.

Secondly, we provided a brief introduction to the extensively studied materials for PCSS, ranging from their structures, defects, and optical and electronic properties. Major challenges still exist in many areas, including optimization of the photocatalytic materials and the overall systems. Developing long-wavelength-responsive photocatalysts are beneficial to achieve high STH efficiencies. Inhibiting back reactions of hydrogen and oxygen by applying coating layers to cocatalysts and photocatalysts can further improve efficiencies. Developing more visible light-responsive photocatalysts for use in seawater splitting is the most important task for enabling large-scale $H_2$ production by using photocatalysis technology.

Finally, it is important to design new water splitting devices for the development of practical systems. Particulate Photocatalysts are proven to be easily scaled up at low cost, but they have critical disadvantages. These include challenges associated with constructing inexpensive large-size reactors, maintaining suspensions over large areas using pumping and stirring, and reclaiming used photocatalysts from the system. Essentially, a combination of highly efficient photocatalysts, inexpensive scalable devices, and innovative technologies for the construction and operation of large-scale photocatalytic plants is required to realize a future sustainable energy source based on hydrogen.

## References

1. Linsebigler AL, Lu G, Yates JT (1995) Photocatalysis on $TiO_2$ surfaces: principles, mechanisms, and selected results. Chem Rev 95:735–758
2. Cao S, Wang CJ, Fu WF, Chen Y (2017) Metal phosphides as co-catalysts for photocatalytic and photoelectrocatalytic water splitting. Chemsuschem 10:4306–4323
3. Cao S, Chen Y, Wang CJ, Lv XJ, Fu WF (2015) Spectacular photocatalytic hydrogen evolution using metal-phosphide/CdS hybrid catalysts under sunlight irradiation. Chem Commun (Camb) 51:8708–8711

4. Fabian DM, Hu S, Singh N, Houle FA, Hisatomi T, Domen K, Osterloh FE, Ardo S (2015) Particle suspension reactors and materials for solar-driven water splitting. Energy Environ Sci 8:2825–2850
5. Serpone N (1997) Relative photonic efficiencies and quantum yields in heterogeneous photocatalysis. J. Photochem Photobiol A 104:1–12
6. Kuhn HJ, Braslavsky SE, Schmidt R (2004) Chemical actinometry (IUPAC Technical Report). Pure Appl Chem 76:2105–2146
7. Buriak JM, Jones CW, Kamat PV, Schanze KS, Schatz GC, Scholes GD, Weiss PS (2016) Virtual issue on best practices for reporting the properties of materials and devices. Chem Mater 28:3525–3526
8. Kisch H (2010) On the problem of comparing rates or apparent quantum yields in heterogeneous photocatalysis. Angew Chem 122:9782–9783
9. Wang Z, Li C, Domen K (2019) Recent developments in heterogeneous photocatalysts for solar-driven overall water splitting. Chem Soc Rev 48:2109–2125
10. Bolton JR (1996) Solar photoproduction of hydrogen: a review. Sol Energy 57:37–50
11. Hwang DW, Kim HG, Kim J, Cha KY, Kim YG, Lee JS (2000) Photocatalytic water splitting over highly donor-doped (110) layered perovskites. J Catal 193:40–48
12. Cao S, Piao L (2020) Considerations for a more accurate evaluation method for photocatalytic water splitting. Angew Chem Int Ed Engl 59:18312–18320
13. Qureshi M, Takanabe K (2017) Insights on measuring and reporting heterogeneous photocatalysis: efficiency definitions and setup examples. Chem Mater 29:158–167
14. Chen S, Takata T, Domen K (2017) Particulate photocatalysts for overall water splitting. Nat Rev Mater 2:1–17
15. Wang Z, Hisatomi T, Li R, Sayama K, Liu G, Domen K, Li C, Wang L (2021) Efficiency accreditation and testing protocols for particulate photocatalysts toward solar fuel production. Joule 5:344–359
16. Liu G, Sheng Y, Ager JW, Kraft M, Xu R (2019) Research advances towards large-scale solar hydrogen production from water. EnergyChem 1
17. Takanabe K (2017) Photocatalytic water splitting: quantitative approaches toward photocatalyst by design. ACS Catal 7:8006–8022
18. Bolton JR, Strickler SJ, Connolly JS (1985) Limiting and realizable efficiencies of solar photolysis of water. Nature 316:495–500
19. Seitz LC, Chen Z, Forman AJ, Pinaud BA, Benck JD, Jaramillo TF (2014) Modeling practical performance limits of photoelectrochemical water splitting based on the current state of materials research. Chemsuschem 7:1372–1385
20. Ma Y, Wang X, Jia Y, Chen X, Han H, Li C (2014) Titanium dioxide-based nanomaterials for photocatalytic fuel generations. Chem Rev 114:9987–10043
21. Ham Y, Hisatomi T, Goto Y, Moriya Y, Sakata Y, Yamakata A, Kubota J, Domen K (2016) Flux-mediated doping of $SrTiO_3$ photocatalysts for efficient overall water splitting. J Mater Chem A 4:3027–3033
22. Kato H, Asakura K, Kudo A (2003) Highly efficient water splitting into $H_2$ and $O_2$ over lanthanum-doped $NaTaO_3$ photocatalysts with high crystallinity and surface nanostructure. J Am Chem Soc 125:3082–3089
23. Maeda K, Domen K (2010) Solid solution of GaN and ZnO as a stable photocatalyst for overall water splitting under visible light. Chem Mater 22:612–623
24. Ong W-J, Tan L-L, Ng YH, Yong S-T, Chai S-P (2016) Graphitic carbon nitride (g-$C_3N_4$)-based photocatalysts for artificial photosynthesis and environmental remediation: are we a step closer to achieving sustainability? Chem Rev 116:7159–7329
25. Sayad Y, Kaminski A, Blanc D, Nouiri A, Lemiti M (2009) Determination of diffusion length in photovoltaic crystalline silicon by modelisation of light beam induced current. Superlattices Microstruct 45:393–401
26. Salvador P (1984) Hole diffusion length in n-$TiO_2$ single crystals and sintered electrodes: photoelectrochemical determination and comparative analysis. J Appl Phys 55:2977–2985

27. Millero FJ, Feistel R, Wright DG, McDougall TJ (2008) The composition of standard seawater and the definition of the reference-composition salinity scale. Deep Sea Res Part I: Ocean Res Pap 55:50–72
28. Li Y, He F, Peng S, Gao D, Lu G, Li S (2011) Effects of electrolyte NaCl on photocatalytic hydrogen evolution in the presence of electron donors over Pt/TiO2. J Mol Catal A: Chem 341:71–76
29. Li Y, He F, Peng S, Lu G, Li S (2011) Photocatalytic $H_2$ evolution from NaCl saltwater over $ZnS_{1-x-0.5y}O_x(OH)_y$–ZnO under visible light irradiation. Int J Hydrogen Energy 36:10565–10573
30. Song T, Zhang P, Wang T, Ali A, Zeng H (2018) Constructing a novel strategy for controllable synthesis of corrosion resistant $Ti^{3+}$ self-doped titanium–silicon materials with efficient hydrogen evolution activity from simulated seawater. Nanoscale 10:2275–2284
31. Zhu C, Liu Ca, Fu Y, Gao J, Huang H, Liu Y, Kang Z (2019) Construction of CDs/CdS photocatalysts for stable and efficient hydrogen production in water and seawater. Appl Catal B: Environ 242:178–185
32. Gao H, Yan S, Wang J, Zou Z (2014) Ion coordination significantly enhances the photocatalytic activity of graphitic-phase carbon nitride. Dalton Trans 43:8178–8183
33. Li Y, Lu G, Li S (2001) Photocatalytic hydrogen generation and decomposition of oxalic acid over platinized $TiO_2$. Appl Catal A Gen 214:179–185
34. Gao M, Connor PKN, Ho GW (2016) Plasmonic photothermic directed broadband sunlight harnessing for seawater catalysis and desalination. Energy Environ Sci 9:3151–3160
35. Simamora AJ, Chang F-C, Wang HP, Yang TC, Wei YL, Lin WK (2013) $H_2$ Fuels from photocatalytic splitting of seawater affected by nano-$TiO_2$ promoted with CuO and NiO. Int J Photoenergy 2013:419182
36. Ji SM, Jun H, Jang JS, Son HC, Borse PH, Lee JS (2007) Photocatalytic hydrogen production from natural seawater. J Photochem Photobiol A 189:141–144
37. Guan X, Chowdhury FA, Pant N, Guo L, Vayssieres L, Mi Z (2018) Efficient unassisted overall photocatalytic seawater splitting on GaN-based nanowire arrays. J Phys Chem C 122:13797–13802
38. Yang C, Qin J, Rajendran S, Zhang X, Liu R (2018) $WS_2$ and C-$TiO_2$ nanorods acting as effective charge separators on g-$C_3N_4$ to boost visible-light activated hydrogen production from seawater. Chemsuschem 11:4077–4085
39. Kawai T, Sakata T (1979) Hydrogen evolution from water using solid carbon and light energy. Nature 282:283–284
40. Zhang J, Hu W, Cao S, Piao L (2020) Recent progress for hydrogen production by photocatalytic natural or simulated seawater splitting. Nano Res 13:2313–2322
41. Shen S, Guo L (2006) Structural, textural and photocatalytic properties of quantum-sized $In_2S_3$-sensitized Ti-MCM-41 prepared by ion-exchange and sulfidation methods. J Solid State Chem 179:2629–2635
42. Shen S, Guo L (2008) Growth of quantum-confined CdS nanoparticles inside Ti-MCM-41 as a visible light photocatalyst. Mater Res Bull 43:437–446
43. Koriche N, Bouguelia A, Aider A, Trari M (2005) Photocatalytic hydrogen evolution over delafossite. Int J Hydrogen Energy 30:693–699
44. Saadi S, Bouguelia A, Derbal A, Trari M (2007) Hydrogen photoproduction over new catalyst $CuLaO_2$. J Photochem Photobiol A 187:97–104
45. Boudjemaa A, Bouarab R, Saadi S, Bouguelia A, Trari M (2009) Photoelectrochemical $H_2$-generation over spinel $FeCr_2O_4$ in $X_2$-solutions ($X_{2-}$=$S_{2-}$ and $SO_{32\text{-}}$). Appl Energy 86:1080–1086
46. Hirai T, Nomura Y, Komasawa I (2003) Immobilization of $RuS_2$ nanoparticles prepared in reverse micellar system onto thiol-modified polystyrene particles and their photocatalytic properties. J Nanopart Res 5:61–67
47. Younsi M, Saadi S, Bouguelia A, Aider A, Trari M (2007) Synthesis and characterization of oxygen-rich delafossite $CuYO_{2+x}$-Application to $H_2$-photo production. Sol Energy Mater Sol Cells 91:1102–1109

48. Bessekhouad Y, Trari M (2002) Photocatalytic hydrogen production from suspension of spinel powders $AMn_2O_4$(A=Cu and Zn). Int J Hydrogen Energy 27:357–362
49. Bao N, Shen L, Takata T, Domen K (2008) Self-Templated synthesis of nanoporous CdS nanostructures for highly efficient photocatalytic hydrogen production under visible light. Chem Mater 20:110–117
50. Yan H, Yang J, Ma G, Wu G, Zong X, Lei Z, Shi J, Li C (2009) Visible-light-driven hydrogen production with extremely high quantum efficiency on Pt–PdS/CdS photocatalyst. J Catal 266:165–168
51. Shen S, Guo L, Chen X, Ren F, Mao SS (2010) Effect of $Ag_2S$ on solar-driven photocatalytic hydrogen evolution of nanostructured CdS. Int J Hydrogen Energy 35:7110–7115
52. Koriche N, Bouguelia A, Trari M, Photocatalytic hydrogen production over new oxide $CuLaO_{2.62}$. Int. J. Hydrogen Energy 31:1196–1203
53. Zhang X, Jing D, Guo L (2010) Effects of anions on the photocatalytic $H_2$ production performance of hydrothermally synthesized Ni-doped $Cd_{0.1}Zn_{0.9}S$ photocatalysts. Int. J. Hydrogen Energy 35:7051–7057
54. Zhang K, Jing D, Chen Q, Guo L (2010) Influence of Sr-doping on the photocatalytic activities of CdS–ZnS solid solution photocatalysts. Int J Hydrogen Energy 35:2048–2057
55. Lu G, Li S (1992) Hydrogen production by H2S photodecomposition on $ZnFe_2O_4$ catalyst. Int J Hydrogen Energy 17:767–770
56. Gurunathan K, Baeg J-O, Lee SM, Subramanian E, Moon S-J, Kong K-J (2008) Visible light active pristine and $Fe^{3+}$ doped $CuGa_2O_4$ spinel photocatalysts for solar hydrogen production. Int J Hydrogen Energy 33:2646–2652
57. Gurunathan K, Baeg J-O, Lee SM, Subramanian E, Moon S-J, Kong K-J (2008) Visible light assisted highly efficient hydrogen production from $H_2S$ decomposition by $CuGaO_2$ and $CuGa_{1-x}In_xO_2$ delafossite oxides bearing nanostructured co-catalysts. Catal Commun 9:395–402
58. Subramanian E, Baeg J-O, Lee SM, Moon S-J, Kong K-J (2008) Dissociation of $H_2S$ under visible light irradiation ($\lambda \geq 420$nm) with $FeGaO_3$ photocatalysts for the production of hydrogen. Int J Hydrogen Energy 33:6586–6594
59. Barbeni M, Pelizzetti E, Borgarello E, Serpone N, Grätzel M, Balducci L, Visca M (1985) Hydrogen from hydrogen sulfide cleavage. Improved efficiencies via modification of semiconductor particulates. Int. J. Hydrogen Energy 10:249–253
60. De GC, Roy AM, Bhattacharya SS (1995) Photocatalytic production of hydrogen and concomitant cleavage of industrial waste hydrogen sulphide. Int J Hydrogen Energy 20:127–131
61. Naman SA, Aliwi SM, Al-Emara K (1986) Hydrogen production from the splitting of $H_2S$ by visible light irradiation of vanadium sulfides dispersion loaded with $RuO_2$. Int J Hydrogen Energy 11:33–38
62. Linkous CA, Muradov NZ, Ramser SN (1995) Consideration of reactor design for solar hydrogen production from hydrogen sulfide using semiconductor particulates. Int J Hydrogen Energy 20:701–709
63. Ohmori T, Mametsuka H, Suzuki E (2000) Photocatalytic hydrogen evolution on InP suspension with inorganic sacrificial reducing agent. Int J Hydrogen Energy 25:953–955
64. He C-H, Yang OB (2003) Hydrogen Evolution by Photocatalytic Decomposition of Water under UV Irradiation over $K[Bi_3PbTi_5O_{16]}$ Perovskite: Effect of Cerium Species. Ind Eng Chem Res 42:419–425
65. Lee SG, Lee S, Lee H-I (2001) Photocatalytic production of hydrogen from aqueous solution containing CN− as a hole scavenger. Appl Catal A-Gen 207:173–181
66. Bamwenda GR, Uesigi T, Abe Y, Sayama K, Arakawa H (2001) The photocatalytic oxidation of water to $O_2$ over pure $CeO_2$, $WO_3$, and $TiO_2$ using $Fe^{3+}$ and $Ce^{4+}$ as electron acceptors. Appl Catal A Gen 205:117–128
67. Ohno T, Tanigawa F, Fujihara K, Izumi S, Matsumura M (1999) Photocatalytic oxidation of water by visible light using ruthenium-doped titanium dioxide powder. J Photochem Photobiol A 127:107–110

68. Galińska A, Walendziewski J (2005) Photocatalytic water splitting over Pt−$TiO_2$ in the presence of sacrificial reagents. Energy Fuels 19:1143–1147
69. Zieliñska B, Borowiak-Palen E, Kalenczuk RJ (2008) Photocatalytic hydrogen generation over alkaline-earth titanates in the presence of electron donors. Int J Hydrogen Energy 33:1797–1802
70. Chiarello GL, Forni L, Selli E (2009) Photocatalytic hydrogen production by liquid- and gas-phase reforming of CH3OH over flame-made $TiO_2$ and Au/$TiO_2$. Catal Today 144:69–74
71. Chen T, Wu G, Feng Z, Hu G, Su W, Ying P, Li C (2008) In situ FT-IR study of photocatalytic decomposition of formic acid to hydrogen on Pt/$TiO_2$ catalyst. Chin J Catal 29:105–107
72. Patsoura A, Kondarides DI, Verykios XE (2007) Photocatalytic degradation of organic pollutants with simultaneous production of hydrogen. Catal Today 124:94–102
73. Hashimoto K, Kawai T, Sakata T (1984) Photocatalytic reactions of hydrocarbons and fossil fuels with water. Hydrogen production and oxidation. The Journal of Physical Chemistry 88:4083–4088
74. Chen S, Takata T, Domen K (2017) Particulate photocatalysts for overall water splitting. Nat Rev Mater 2:17050
75. Sayama K, Arakawa H (1996) Effect of carbonate addition on the photocatalytic decomposition of liquid water over a $ZrO_2$ catalyst. J Photochem Photobiol A 94:67–76
76. Jing DW, Zhang YJ, Guo LJ (2005) Study on the synthesis of Ni doped mesoporous $TiO_2$ and its photocatalytic activity for hydrogen evolution in aqueous methanol solution. Chem Phys Lett 415:74–78
77. Ebina Y, Sasaki T, Harada M, Watanabe M (2002) Restacked perovskite nanosheets and their Pt-loaded materials as photocatalysts. Chem Mater 14:4390–4395
78. Kudo A, Mikami I (1998) New $In_2O_3(ZnO)(m)$ photocatalysts with laminal structure for visible light-induced $H_2$ or $O_2$ evolution from aqueous solutions containing sacrificial reagents. Chem. Lett. 1027–1028
79. Ikuma Y, Bessho H (2007) Effect of Pt concentration on the production of hydrogen by a $TiO_2$ photocatalyst. Int J Hydrogen Energy 32:2689–2692
80. Ogisu K, Ishikawa A, Teramura K, Toda K, Hara M, Domen K (2007) Lanthanum-indium oxysulfide as a visible light driven photocatalyst for water splitting. Chem Lett 36:854–855
81. Ogisu K, Ishikawa A, Shimodaira Y, Takata T, Kobayashi H, Domen K (2008) Electronic band structures and photochemical properties of La-Ga-based oxysulfides. J Phys Chem C 112:11978–11984
82. Jang JS, Joshi UA, Lee JS (2007) Solvothermal synthesis of CdS nanowires for photocatalytic hydrogen and electricity production. J Phys Chem C 111:13280–13287
83. Bessekhouad Y, Mohammedi M, Trari M (2002) Hydrogen photoproduction from hydrogen sulfide on Bi2S3 catalyst. Sol Energy Mater Sol Cells 73:339–350
84. Bao NZ, Shen LM, Takata T, Lu DL, Domen K (2006) Highly ordered Pt-loaded CdS nanowire arrays for photocatalytic hydrogen production under visible light. Chem Lett 35:318–319
85. Hara M, Hitoki G, Takata T, Kondo JN, Kobayashi H, Domen K (2003) TaON and $Ta_3N_5$ as new visible light driven photocatalysts. Catal Today 78:555–560
86. Hitoki G, Takata T, Kondo JN, Hara M, Kobayashi H, Domen K (2002) An oxynitride, TaON, as an efficient water oxidation photocatalyst under visible light irradiation (lambda <= 500 nm). Chem. Commun. 1698–1699
87. Kasahara A, Nukumizu K, Takata T, Kondo JN, Hara M, Kobayashi H, Domen K (2003) $LaTiO_2N$ as a visible-light (<= 600 nm)-driven photocatalyst (2). J Phys Chem B 107:791–797
88. Xiao W, Yuan H, Zhang W, Shangguan W (2007) TiN film with (111) preferred orientation as a visible-light-driven photocatalyst for hydrogen evolution from water decomposition. Mater Chem Phys 105:6–9
89. Chiarello GL, Selli E, Forni L (2008) Photocatalytic hydrogen production over flame spray pyrolysis-synthesised $TiO_2$ and Au/$TiO_2$. Appl Catal B-Environ 84:332–339
90. Sreethawong T, Yoshikawa S (2005) Comparative investigation on photocatalytic hydrogen evolution over Cu-, Pd-, and Au-loaded mesoporous $TiO_2$ photocatalysts. Catal Commun 6:661–668

91. Bae E, Choi W (2003) Highly enhanced photoreductive degradation of perchlorinated compounds on dye-sensitized metal/$TiO_2$ under visible light. Environ Sci Technol 37:147–152
92. Arabatzis IM, Stergiopoulos T, Andreeva D, Kitova S, Neophytides SG, Falaras P (2003) Characterization and photocatalytic activity of Au/$TiO_2$ thin films for azo-dye degradation. J Catal 220:127–135
93. Tai YW, Chen JS, Yang CC, Wan BZ (2004) Preparation of nano-gold on $K_2La_2Ti_3O_{10}$ for producing hydrogen from photo-catalytic water splitting. Catal Today 97:95–101
94. Tsuji I, Kato H, Kudo A (2005) Visible-light-induced $H_2$ evolution from an aqueous solution containing sulfide and sulfite over a ZnS-$CuInS_2$-$AgInS_2$ solid-solution photocatalyst. Angew Chem Int Ed 44:3565–3568
95. Hara M, Nunoshige J, Takata T, Kondo JN, Domen K (2003) Unusual enhancement of H-2 evolution by Ru on TaON photocatalyst under visible light irradiation. Chem. Commun. 3000–3001
96. Navarro RM, del Valle F, Fierro JLG (2008) Photocatalytic hydrogen evolution from CdS-ZnO-CdO systems under visible light irradiation: effect of thermal treatment and presence of Pt and Ru cocatalysts. Int J Hydrogen Energy 33:4265–4273
97. Sano T, Kutsuna S, Negishi N, Takeuchi K (2002) Effect of Pd-photodeposition over $TiO_2$ on product selectivity in photocatalytic degradation of vinyl chloride monomer. J Mol Catal A-Chem 189:263–270
98. Wang X, He Z, Zhong S, Xiao X (2007) Photocatalytic synthesis of hydrocarbon oxygenates from $C_2H_6$ and $CO_2$ over Pd-$MoO_3$/$SiO_2$ catalyst. J Nat Gas Chem 16:173–178
99. Jin S, Shiraishi F (2004) Photocatalytic activities enhanced for decompositions of organic compounds over metal-photodepositing titanium dioxide. Chem Eng J 97:203–211
100. Ke D, Peng T, Ma L, Cai P, Jiang P (2008) Photocatalytic water splitting for $O_2$ production under visible-light irradiation on BiVO4 nanoparticles in different sacrificial reagent solutions. Appl Catal A-Gen 350:111–117
101. Georgekutty R, Seery MK, Pillai SC (2008) A highly efficient Ag-ZnO photocatalyst: synthesis, properties, and mechanism. J Phys Chem C 112:13563–13570
102. Lu W, Gao S, Wang J (2008) One-pot synthesis of Ag/ZnO self-assembled 3D hollow microspheres with enhanced photocatalytic performance. J Phys Chem C 112:16792–16800
103. Anandan S, Sathishkumar P, Pugazhenthiran N, Madhavan J, Maruthamuthu P (2008) Effect of loaded silver nanoparticles on $TiO_2$ for photocatalytic degradation of Acid Red 88. Sol Energy Mater Sol Cells 92:929–937
104. Hou X-G, Huang M-D, Wu X-L, Liu A-D (2009) Preparation and studies of photocatalytic silver-loaded $TiO_2$ films by hybrid sol-gel method. Chem Eng J 146:42–48
105. Pal B, Ikeda S, Kominami H, Kera Y, Ohtani B (2003) Photocatalytic redox-combined synthesis of L-pipecolinic acid from L-lysine by suspended titania particles: effect of noble metal loading on the selectivity and optical purity of the product. J Catal 217:152–159
106. Sasaki Y, Iwase A, Kato H, Kudo A (2008) The effect of co-catalyst for Z-scheme photocatalysis systems with an $Fe^{3+}$/$Fe^{2+}$ electron mediator on overall water splitting under visible light irradiation. J Catal 259:133–137
107. Pal B, Torimoto T, Okazaki K-I, Ohtani B (2007) Photocatalytic syntheses of azoxybenzene by visible light irradiation of silica-coated cadmium sulfide nanocomposites. Chem Commun 483–485
108. Iwase A, Kato H, Kudo A (2006) Nanosized Au particles as an efficient cocatalyst for photocatalytic overall water splitting. Catal Lett 108:7–10
109. Ebina Y, Sakai N, Sasaki T (2005) Photocatalyst of lamellar aggregates of RuOx-loaded perovskite nanosheets for overall water splitting. J Phys Chem B 109:17212–17216
110. Kadowaki H, Saito N, Nishiyama H, Kobayashi H, Shimodaira Y, Inoue Y (2007) Overall splitting of water by $RuO_2$-loaded $PbWO_4$ photocatalyst with d(10)s(2)-d(0) configuration. J Phys Chem C 111:439–444
111. Arai N, Saito N, Nishiyama H, Shimodaira Y, Kohayashi H, Inoue Y, Sato K (2008) Photocatalytic activity for overall water splitting of $RuO_2$-loaded $Y_xIn_{2-x}O_3$ ($x$=0.9–1.5). J. Phys. Chem. C 112:5000–5005

112. Sato J, Saito N, Yamada Y, Maeda K, Takata T, Kondo JN, Hara M, Kobayashi H, Domen K, Inoue Y (2005) $RuO_2$-loaded beta-Ge3N4 as a non-oxide photocatalyst for overall water splitting. J Am Chem Soc 127:4150–4151
113. Lee Y, Terashima H, Shimodaira Y, Teramura K, Hara M, Kobayashi H, Domen K, Yashima M (2007) Zinc germanium oxynitride as a photocatalyst for overall water splitting under visible light. J Phys Chem C 111:1042–1048
114. Arai N, Saito N, Nishiyama H, Domen K, Kobayashi H, Sato K, Inoue Y (2007) Effects of divalent metal ion ($Mg^{2+}$, $Zn^{2+}$ and $Be^{2+}$) doping on photocatalytic activity of ruthenium oxide-loaded gallium nitride for water splitting. Catal Today 129:407–413
115. Miseki Y, Kato H, Kudo A (2005) Water splitting into $H_2$ and $O_2$ over Cs2Nb4O11 photocatalyst. Chem Lett 34:54–55
116. Kato H, Kudo A (2001) Water splitting into H2 and O-2 on alkali tantalate photocatalysts ATaO(3) (A = Li, Na, and K). J Phys Chem B 105:4285–4292
117. Sreethawong T, Suzuki Y, Yoshikawa S (2005) Photocatalytic evolution of hydrogen over mesoporous $TiO_2$ supported NiO photocatalyst prepared by single-step sol-gel process with surfactant template. Int J Hydrogen Energy 30:1053–1062
118. Lin H-Y, Chen Y-F, Chen Y-W (2007) Water splitting reaction on NiO/$InVO_4$ under visible light irradiation. Int J Hydrogen Energy 32:86–92
119. Maeda K, Domen K (2007) New non-oxide photocatalysts designed for overall water splitting under visible light. J Phys Chem C 111:7851–7861
120. Kawai T, Sakata T (1980) Conversion of carbohydrate into hydrogen fuel by a photocatalytic process. Nature 286:474–476
121. Maeda K, Teramura K, Lu D, Takata T, Saito N, Inoue Y, Domen K (2006) Characterization of Rh-Cr mixed-oxide nanoparticles dispersed on $(Ga_{1-x}Zn_x)(N_{1-x}O_x)$ as a cocatalyst for visible-light-driven overall water splitting. J Phys Chem B 110:13753–13758
122. Maeda K, Teramura K, Saito N, Inoue Y, Domen K (2006) Improvement of photocatalytic activity of $(Ga_{1-x}Zn_x)(N_{1-x}O_x)$ solid solution for overall water splitting by co-loading Cr and another transition metal. J Catal 243:303–308
123. Maeda K, Teramura K, Domen K (2007) Development of cocatalysts for photocatalytic overall water splitting on $(Ga_{1-x}Zn_x)(N_{1-x}O_x)$ solid solution. Catal Surv Asia 11:145–157
124. Maeda K, Lu D, Teramura K, Domen K (2008) Direct deposition of nanoparticulate rhodium-chromium mixed-oxides on a semiconductor powder by band-gap irradiation. J Mater Chem 18:3539–3542
125. Hisatomi T, Miyazaki K, Takanabe K, Maeda K, Kubota J, Sakata Y, Domen K (2010) Isotopic and kinetic assessment of photocatalytic water splitting on Zn-added $Ga_2O_3$ photocatalyst loaded with $Rh_{2\text{-}y}CryO_3$ cocatalyst. Chem Phys Lett 486:144–146
126. Maeda K, Teramura K, Lu D, Saito N, Inoue Y, Domen K (2006) Noble-metal/$Cr_2O_3$ core/shell nanoparticles as a cocatalyst for photocatalytic overall water splitting. Angew Chem Int Ed 45:7806–7809
127. Maeda K, Teramura K, Lu D, Saito N, Inoue Y, Domen K (2007) Roles of Rh/$Cr_2O_3$ (core/shell) nanoparticles photodeposited on visible-light-responsive $(Ga_{1-x}Zn_x)(N_{1-x}O_x)$ solid solutions in photocatalytic overall water splitting. J Phys Chem C 111:7554–7560
128. Maeda K, Lu D, Teramura K, Domen K (2010) Simultaneous photodeposition of rhodium-chromium nanoparticles on a semiconductor powder: structural characterization and application to photocatalytic overall water splitting. Energy Environ Sci 3:471–478
129. Maeda K, Sakamoto N, Ikeda T, Ohtsuka H, Xiong A, Lu D, Kanehara M, Teranishi T, Domen K (2010) Preparation of core-shell-structured nanoparticles (with a noble-metal or metal oxide core and a chromia shell) and their application in water splitting by means of visible light. Chem Eur J 16:7750–7759
130. Maeda K, Xiong A, Yoshinaga T, Ikeda T, Sakamoto N, Hisatomi T, Takashima M, Lu D, Kanehara M, Setoyama T, Teranishi T, Domen K (2010) Photocatalytic overall water splitting promoted by two different cocatalysts for hydrogen and oxygen evolution under visible light. Angew Chem Int Ed 49:4096–4099

131. Tian M, Shangguan W, Yuan J, Wang S, Ouyang Z (2007) Promotion effect of nanosized Pt, $RuO_2$ and NiOx loading on visible light-driven photocatalysts K4Ce2M10O30 (M = Ta, Nb) for hydrogen evolution from water decomposition. Sci Technol Adv Mater 8:82–88
132. Thaminimulla CTK, Takata T, Hara M, Kondo JN, Domen K (2000) Effect of chromium addition for photocatalytic overall water splitting on Ni-$K_2La_2Ti_3O_{10}$. J Catal 196:362–365
133. Zong X, Wu G, Yan H, Ma G, Shi J, Wen F, Wang L, Li C (2010) Photocatalytic $H_2$ evolution on $MoS_2$/CdS catalysts under visible light irradiation. J Phys Chem C 114:1963–1968
134. Zong X, Yan H, Wu G, Ma G, Wen F, Wang L, Li C (2008) Enhancement of photocatalytic $H_2$ evolution on CdS by loading $MoS_2$ as cocatalyst under visible light irradiation. J Am Chem Soc 130:7176–7177
135. Frame FA, Osterloh FE (2010) CdSe-$MoS_2$: a quantum size-confined photocatalyst for hydrogen evolution from water under visible light. J Phys Chem C 114:10628–10633
136. Tabata M, Maeda K, Ishihara T, Minegishi T, Takata T, Domen K (2010) Photocatalytic hydrogen evolution from water using copper gallium sulfide under visible-light irradiation. J Phys Chem C 114:11215–11220
137. Goto Y, Hisatomi T, Wang Q, Higashi T, Ishikiriyama K, Maeda T, Sakata Y, Okunaka S, Tokudome H, Katayama M, Akiyama S, Nishiyama H, Inoue Y, Takewaki T, Setoyama T, Minegishi T, Takata T, Yamada T, Domen K (2018) A particulate photocatalyst water-splitting panel for large-scale solar hydrogen generation. Joule 2:509–520
138. Zhang Q, Li Z, Wang S, Li R, Zhang X, Liang Z, Han H, Liao S, Li C (2016) Effect of redox cocatalysts location on photocatalytic overall water splitting over cubic $NaTaO_3$ semiconductor crystals exposed with equivalent facets. ACS Catal 6:2182–2191
139. Kudo A, Miseki Y (2009) Heterogeneous photocatalyst materials for water splitting. Chem Soc Rev 38:253–278
140. Chen X, Liu L, Yu Peter Y, Mao Samuel S (2011) Increasing solar absorption for photocatalysis with black hydrogenated titanium dioxide nanocrystals. Science 331:746–750
141. Tao X, Zhao Y, Mu L, Wang S, Li R, Li C (2018) Bismuth tantalum oxyhalogen: a promising candidate photocatalyst for solar water splitting. Adv Energy Mater 8:1701392
142. Cai J, Wu M, Wang Y, Zhang H, Meng M, Tian Y, Li X, Zhang J, Zheng L, Gong J (2017) Synergetic enhancement of light harvesting and charge separation over surface-disorder-engineered $TiO_2$ photonic crystals. Chem 2:877–892
143. Rather RA, Singh S, Pal B (2017) Visible and direct sunlight induced $H_2$ production from water by plasmonic Ag-$TiO_2$ nanorods hybrid interface. Sol Energy Mater Sol Cells 160:463–469
144. Si Y, Cao S, Wu Z, Ji Y, Mi Y, Wu X, Liu X, Piao L (2018) What is the predominant electron transfer process for Au NRs/$TiO_2$ nanodumbbell heterostructure under sunlight irradiation? Appl Catal B Environ 220:471–476
145. Si Y, Cao S, Wu Z, Ji Y, Mi Y, Wu X, Liu X, Piao L (2017) The effect of directed photogenerated carrier separation on photocatalytic hydrogen production. Nano Energy 41:488–493
146. Xiao S-T, Wu S-M, Dong Y, Liu J-W, Wang L-Y, Wu L, Zhang Y-X, Tian G, Janiak C, Shalom M, Wang Y-T, Li Y-Z, Jia R-K, Bahnemann DW, Yang X-Y (2020) Rich surface hydroxyl design for nanostructured $TiO_2$ and its hole-trapping effect. Chem Eng J 400:125909
147. Zhang YX, Wu SM, Tian G, Zhao XF, Wang LY, Yin YX, Wu L, Li QN, Zhang YX, Wu JS (2021) Titanium vacancies in $TiO_2$ nanofibers enable highly efficient photodriven seawater splitting. Chem–A Eur J 27:14202–14208
148. Vilatela JJ, Eder D (2012) Nanocarbon composites and hybrids in sustainability: a review. Chemsuschem 5:456–478
149. Christoforidis KC, Fornasiero P (2017) Photocatalytic hydrogen production: a rift into the future energy supply. ChemCatChem 9:1523–1544
150. Lu Y, Liu Y-X, He L, Wang L-Y, Liu X-L, Liu J-W, Li Y-Z, Tian G, Zhao H, Yang X-H, Liu J, Janiak C, Lenaerts S, Yang X-Y, Su B-L (2020) Interfacial co-existence of oxygen and titanium vacancies in nanostructured TiO2 for enhancement of carrier transport. Nanoscale 12:8364–8370
151. Wang S, Pan L, Song J-J, Mi W, Zou J-J, Wang L, Zhang X (2015) Titanium-defected undoped anatase $TiO_2$ with p-type conductivity, room-temperature ferromagnetism, and remarkable photocatalytic performance. J Am Chem Soc 137:2975–2983

152. Lu Y, Liu X-L, He L, Zhang Y-X, Hu Z-Y, Tian G, Cheng X, Wu S-M, Li Y-Z, Yang X-H, Wang L-Y, Liu J-W, Janiak C, Chang G-G, Li W-H, Van Tendeloo G, Yang X-Y, Su B-L (2020) Spatial heterojunction in nanostructured $TiO_2$ and its cascade effect for efficient photocatalysis. Nano Lett 20:3122–3129
153. Wu S-M, Liu X-L, Lian X-L, Tian G, Janiak C, Zhang Y-X, Lu Y, Yu H-Z, Hu J, Wei H, Zhao H, Chang G-G, Tendeloo G, Wang L-Y, Yang X-Y, Su B-L (2018) Homojunction of oxygen and titanium vacancies and its interfacial *n–p* effect. Adv Mater 30:1802173
154. Guo L, Yang Z, Marcus K, Li Z, Luo B, Zhou L, Wang X, Du Y, Yang Y (2018) $MoS_2/TiO_2$ heterostructures as nonmetal plasmonic photocatalysts for highly efficient hydrogen evolution. Energy Environ Sci 11:106–114
155. Dang HV, Wang YH, Wu JCS (2021) Z-scheme photocatalyst Pt/GaP-TiO2-SiO2:Rh for the separated $H_2$ evolution from photocatalytic seawater splitting. Appl Catal B: Environ 296:120339
156. Pinaud BA, Benck JD, Seitz LC, Forman AJ, Chen Z, Deutsch TG, James BD, Baum KN, Baum GN, Ardo S, Wang H, Miller E, Jaramillo TF (2013) Technical and economic feasibility of centralized facilities for solar hydrogen production via photocatalysis and photoelectrochemistry. Energy Environ Sci 6:1983–2002
157. Hisatomi T, Kubota J, Domen K (2014) Recent advances in semiconductors for photocatalytic and photoelectrochemical water splitting. Chem Soc Rev 43:7520–7535
158. Wang X, Maeda K, Thomas A, Takanabe K, Xin G, Carlsson JM, Domen K, Antonietti M (2009) A metal-free polymeric photocatalyst for hydrogen production from water under visible light. Nat Mater 8:76–80
159. Zheng Y, Lin L, Wang B, Wang X (2015) Graphitic carbon nitride polymers toward sustainable photoredox catalysis. Angew Chem Int Ed 54:12868–12884
160. Lin L, Wang C, Ren W, Ou H, Zhang Y, Wang X (2017) Photocatalytic overall water splitting by conjugated semiconductors with crystalline poly(triazine imide) frameworks. Chem Sci 8:5506–5511
161. Wang L, Wan Y, Ding Y, Wu S, Zhang Y, Zhang X, Zhang G, Xiong Y, Wu X, Yang J, Xu H (2017) Conjugated microporous polymer nanosheets for overall water splitting using visible light. Adv Mater 29:1702428
162. Lin L, Yu Z, Wang X (2019) Crystalline carbon nitride semiconductors for photocatalytic water splitting. Angew Chem Int Ed 58:6164–6175
163. Liu J, Liu Y, Liu N, Han Y, Zhang X, Huang H, Lifshitz Y, Lee S-T, Zhong J, Kang Z (2015) Metal-free efficient photocatalyst for stable visible water splitting via a two-electron pathway. Science 347:970–974
164. Liu Y, Xiang Z (2019) Fully conjugated covalent organic polymer with carbon-encapsulated $Ni_2P$ for highly sustained photocatalytic $H_2$ production from seawater. ACS Appl Mater Inter 11:41313–41320
165. Yang X, Hu Z, Yin Q, Shu C, Jiang XF, Zhang J, Wang X, Jiang JX, Huang F, Cao Y (2019) Water-soluble conjugated molecule for solar-driven hydrogen evolution from salt water. Adv Funct Mater 29:1808156
166. Li L, Zhou Z, Li L, Zhuang Z, Bi J, Chen J, Yu Y, Yu J (2019) Thioether-functionalized 2D covalent organic framework featuring specific affinity to Au for photocatalytic hydrogen production from seawater. ACS Sustain Chem Eng 7:18574–18581
167. Ranjeesh KC, George L, Maibam A, Krishnamurty S, Babu SS (2021) A durable Metallo-porphyrin 2D-polymer for photocatalytic hydrogen and oxygen evolution from river and sea waters. ChemCatChem 13:1717–1721
168. Guselnikova O, Trelin A, Miliutina E, Elashnikov R, Sajdl P, Postnikov P, Kolska Z, Svorcik V, Lyutakov O (2020) Plasmon-induced water splitting—through flexible hybrid 2D architecture up to hydrogen from seawater under NIR light. ACS Appl Mater Inter 12:28110–28119
169. Tao Jing YD (2017) Development of solid solution photocatalytic materials. Acta Phys Chim Sin 33:295–304
170. Hart JN, Allan NL, Claeyssens F (2011) Ternary silicon germanium nitrides: a class of tunable band gap materials. Phys Rev B 84:245209

171. Ouyang S, Ye J (2011) β-AgAl1-xGaxO$_2$ solid-solution photocatalysts: continuous modulation of electronic structure toward high-performance visible-light photoactivity. J Am Chem Soc 133:7757–7763
172. Tsuji I, Kato H, Kudo A (2006) Photocatalytic hydrogen evolution on $ZnS-CuInS_2-AgInS_2$ solid solution photocatalysts with wide visible light absorption bands. Chem Mater 18:1969–1975
173. Maeda K, Takata T, Hara M, Saito N, Inoue Y, Kobayashi H, Domen K (2005) GaN:ZnO solid solution as a photocatalyst for visible-light-driven overall water splitting. J Am Chem Soc 127:8286–8287
174. Schulz H, Thiemann KH (1977) Crystal structure refinement of AlN and GaN. Solid State Commun 23:815–819
175. García-Martínez O, Rojas RM, Vila E, de Vidales JLM (1993) Microstructural characterization of nanocrystals of ZnO and CuO obtained from basic salts. Solid State Ionics 63–65:442–449
176. Ohno T, Bai L, Hisatomi T, Maeda K, Domen K (2012) Photocatalytic water splitting using modified GaN:ZnO solid solution under visible light: long-time operation and regeneration of activity. J Am Chem Soc 134:8254–8259
177. Maeda K, Masuda H, Domen K (2009) Effect of electrolyte addition on activity of $(Ga_{1-x}Zn_x)(N_{1-x}O_x)$ photocatalyst for overall water splitting under visible light. Catal Today 147:173–178
178. Qiu B, Zhu Q, Xing M, Zhang J (2017) A robust and efficient catalyst of CdxZn1−xSe motivated by CoP for photocatalytic hydrogen evolution under sunlight irradiation. Chem Commun 53:897–900
179. Li Y, Lin S, Peng S, Lu G, Li S (2013) Modification of $ZnS_{1-x-0.5y}O_x(OH)_y$–ZnO photocatalyst with NiS for enhanced visible-light-driven hydrogen generation from seawater. Int J Hydrogen Energy 38:15976–15984
180. Chew Y-H, Ng B-J, Tang J-Y, Tan L-L, Chai, SP (2021) A synergistic combination of P-doped $Zn_{0.5}Cd_{0.5}S$ and CoP for dual-stage electron trapping and its application in seawater splitting. Solar RRL 5:2100016
181. Zeng G, Cao Y, Wu Y, Yuan H, Zhang B, Wang Y, Zeng H, Huang S (2021) $Cd_{0.5}Zn_{0.5}S/Ti_3C_2$ MXene as a Schottky catalyst for highly efficient photocatalytic hydrogen evolution in seawater. Appl Mater Today 22:100926
182. Lopes PAL, Maia DLdS, Silva LA (2020) Chalcogenide nanoparticles like $Cd_xZn_{(1-x)}SySe_{(1-y)}$ applied to photocatalytic hydrogen production from natural seawater under visible light irradiation. Mater Today Commun 25:101503
183. Wu Y, Ceder G (2013) First principles study on $Ta_3N_5$:$Ti_3O_3N_2$ solid solution as a water-splitting photocatalyst. J Phys Chem C 117:24710–24715
184. Zhou G, Guo Z, Shan Y, Wu S, Zhang J, Yan K, Liu L, Chu PK, Wu X (2019) High-efficiency hydrogen evolution from seawater using hetero-structured T/Td phase $ReS_2$ nanosheets with cationic vacancies. Nano Energy 55:42–48
185. Cui G, Wang W, Ma M, Xie J, Shi X, Deng N, Xin J, Tang B (2015) IR-driven photocatalytic water splitting with $WO_2$–$Na_xWO_3$ hybrid conductor material. Nano Lett 15:7199–7203
186. Yang TC, Chang FC, Wang HP, Wei YL, Jou CJ (2014) Photocatalytic splitting of seawater effected by (Ni–ZnO)@C nanoreactors. Mar Pollut Bull 85:696–699
187. Chang C-J, Huang K-L, Chen J-K, Chu K-W, Hsu M-H (2015) Improved photocatalytic hydrogen production of ZnO/ZnS based photocatalysts by Ce doping. J Taiwan Inst Chem Eng 55:82–89
188. Kim JH, Hansora D, Sharma P, Jang J-W, Lee JS (2019) Toward practical solar hydrogen production - an artificial photosynthetic leaf-to-farm challenge. Chem Soc Rev 48:1908–1971
189. https://www.energy.gov/eere/fuelcells/doe-technical-targets-hydrogen-production-photoelectrochemical-water-splitting.
190. Pinaud BA, Benck JD, Seitz LC, Forman AJ, Chen Z, Deutsch TG, James BD, Baum KN, Baum GN, Ardo S (2013) Technical and economic feasibility of centralized facilities for solar hydrogen production via photocatalysis and photoelectrochemistry. Energy Environ Sci 6:1983–2002

191. Setoyama T, Takewaki T, Domen K, Tatsumi T (2017) The challenges of solar hydrogen in chemical industry: how to provide, and how to apply? Faraday Discuss 198:509–527
192. Shaner MR, Atwater HA, Lewis NS, McFarland EW (2016) A comparative technoeconomic analysis of renewable hydrogen production using solar energy. Energy Environ Sci 9:2354–2371
193. Nishiyama H, Yamada T, Nakabayashi M, Maehara Y, Yamaguchi M, Kuromiya Y, Nagatsuma Y, Tokudome H, Akiyama S, Watanabe T, Narushima R, Okunaka S, Shibata N, Takata T, Hisatomi T, Domen K (2021) Photocatalytic solar hydrogen production from water on a 100–$m^2$ scale. Nature 598:304–307
194. Liu M, Wang L, Lu G, Yao X, Guo L (2011) Twins in Cd1−xZnxS solid solution: Highly efficient photocatalyst for hydrogen generation from water. Energy Environ Sci 4:1372–1378
195. Hwang J-Y, Shi S, Xu Z, Peterson KW (2006) synthesis of monodispersed iron oxide particles by a large-scale microwave reactor. Chem Eng Commun 193:1586–1591
196. Pan L, Liu X, Sun Z, Sun CQ (2013) Nanophotocatalysts via microwave-assisted solution-phase synthesis for efficient photocatalysis. J. Mater. Chem. A 1:8299–8326
197. Thostenson ET, Chou TW (1999) Microwave processing: fundamentals and applications. Compos A Appl Sci Manuf 30:1055–1071
198. Xiao J, Liu P, Wang CX, Yang GW (2017) External field-assisted laser ablation in liquid: An efficient strategy for nanocrystal synthesis and nanostructure assembly. Prog Mater Sci 87:140–220
199. Jedsukontorn T, Ueno T, Saito N, Hunsom M (2017) Facile preparation of defective black $TiO_2$ through the solution plasma process: Effect of parametric changes for plasma discharge on its structural and optical properties. J Alloys Compd 726:567–577
200. Zhang Z-K, Bai M-L, Guo D-Z, Hou S-M, Zhang G-M (2011) Plasma-electrolysis synthesis of TiO2 nano/microspheres with optical absorption extended into the infra-red region. Chem Commun 47:8439–8441
201. Kimura T (2011) In: Advances in ceramics-synthesis and characterization, processing and specific applications, pp. 75–100
202. Sun J, Chen G, Pei J, Jin R, Wang Q, Guang X (2012) A simple approach to strontium sodium tantalite mesocrystals with ultra-high photocatalytic properties for water splitting. J Mater Chem 22:5609–5614
203. Darr JA, Zhang J, Makwana NM, Weng X (2017) Continuous hydrothermal synthesis of inorganic nanoparticles: applications and future directions. Chem Rev 117:11125–11238
204. Makwana NM, Tighe CJ, Gruar RI, McMillan PF, Darr JA (2016) Pilot plant scale continuous hydrothermal synthesis of nano-titania; effect of size on photocatalytic activity. Mater Sci Semicond Process 42:131–137
205. Weng X, Zeng Q, Zhang Y, Dong F, Wu Z (2016) Facile approach for the syntheses of ultrafine $TiO_2$ nanocrystallites with defects and C heterojunction for photocatalytic water splitting. ACS Sustain Chem Eng 4:4314–4320
206. Wu S, Wang W, Tu W, Yin S, Sheng Y, Manuputty MY, Kraft M, Xu R (2018) Premixed stagnation flame synthesized $TiO_2$ nanoparticles with mixed phases for efficient photocatalytic hydrogen generation. ACS Sustain Chem Eng 6:14470–14479
207. Manuputty MY, Dreyer JAH, Sheng Y, Bringley EJ, Botero MariaL, Akroyd J, Kraft M (2019) Polymorphism of nanocrystalline $TiO_2$ prepared in a stagnation flame: formation of the $TiO_2$-II phase. Chem Sci 10:1342–1350
208. Teoh WY (2013) A perspective on the flame spray synthesis of photocatalyst nanoparticles. Materials 6
209. Xing Z, Zong X, Pan J, Wang L (2013) On the engineering part of solar hydrogen production from water splitting: photoreactor design. Chem Eng Sci 104:125–146
210. Jing D, Liu H, Zhang X, Zhao L, Guo L (2009) Photocatalytic hydrogen production under direct solar light in a CPC based solar reactor: reactor design and preliminary results. Energy Convers Manage 50:2919–2926
211. Xiong A, Ma G, Maeda K, Takata T, Hisatomi T, Setoyama T, Kubota J, Domen K (2014) Fabrication of photocatalyst panels and the factors determining their activity for water splitting. Catal Sci Technol 4:325–328

212. Schröder M, Kailasam K, Borgmeyer J, Neumann M, Thomas A, Schomäcker R, Schwarze M (2015) Hydrogen evolution reaction in a large-scale reactor using a carbon nitride photocatalyst under natural sunlight irradiation. Energy Technol 3:1014–1017
213. Wang Q, Hisatomi T, Suzuki Y, Pan Z, Seo J, Katayama M, Minegishi T, Nishiyama H, Takata T, Seki K (2017) Particulate photocatalyst sheets based on carbon conductor layer for efficient Z-scheme pure-water splitting at ambient pressure. J Am Chem Soc 139:1675–1683
214. Tilley SD, Lany S, Van de Krol R (2018) Advances in photoelectrochemical water splitting: theory. Royal Society of Chemistry, Experiment and Systems Analysis
215. Sun S, Hisatomi T, Wang Q, Chen S, Ma G, Liu J, Nandy S, Minegishi T, Katayama M, Domen K (2018) Efficient redox-mediator-free Z-scheme water splitting employing oxysulfide photocatalysts under visible light. ACS Catal 8:1690–1696
216. Alsayegh S, Johnson JR, Ohs B, Lohaus J, Wessling M (2017) Systematic optimization of H2 recovery from water splitting process using membranes and $N_2$ diluent. Int J Hydrogen Energy 42:6000–6011
217. Alsayegh S, Johnson JR, Wei X, Ohs B, Lohaus J, Wessling M (2017) CO2 aided H2 recovery from water splitting processes. Int J Hydrogen Energy 42:21793–21805
218. Huang C, Yao W, T-Raissi A, Muradov N (2011) Development of efficient photoreactors for solar hydrogen production. Solar Energy 85:19–27
219. Reilly K, Fang B, Taghipour F, Wilkinson DP (2017) Enhanced photocatalytic hydrogen production in a UV-irradiated fluidized bed reactor. J Catal 353:63–73
220. Reilly K, Wilkinson DP, Taghipour F (2018) Photocatalytic water splitting in a fluidized bed system: Computational modeling and experimental studies. Appl Energy 222:423–436
221. Vagia EC, Muradov N, Kalyva A, T-Raissi A, Qin N, Srinivasa AR, Kakosimos KE (2017) Solar hybrid photo-thermochemical sulfur-ammonia water-splitting cycle: Photocatalytic hydrogen production stage. Int J Hydrogen Energy 42:20608–20624
222. Braham RJ, Harris AT (2009) Review of major design and scale-up considerations for solar photocatalytic reactors. Ind Eng Chem Res 48:8890–8905
223. Fuqiang W, Ziming C, Jianyu T, Yuan Y, Yong S, Linhua L (2017) Progress in concentrated solar power technology with parabolic trough collector system: A comprehensive review. Renew Sustain Energy Rev 79:1314–1328
224. Yang Y, Wei Q, Hou J, Liu H, Zhao L (2016) Solar concentrator with uniform irradiance for particulate photocatalytic hydrogen production system. Int J Hydrogen Energy 41:16040–16047
225. Touili S, Alami Merrouni A, Azouzoute A, El Hassouani Y, Amrani A-I (2018) A technical and economical assessment of hydrogen production potential from solar energy in Morocco. Int J Hydrogen Energy 43:22777–22796
226. Chen H, Bo R, Tran-Phu T, Liu G, Tricoli A (2018) One-step rapid and scalable flame synthesis of efficient $WO_3$ photoanodes for water splitting. ChemPlusChem 83:569–576
227. Yadav D, Banerjee R (2018) Economic assessment of hydrogen production from solar driven high-temperature steam electrolysis process. J Clean Prod 183:1131–1155